A SEARCH FOR THE PROCESS $K^+ \to \pi^+ + \pi^0 + \gamma$

Thesis by

Robert James Macek

In Partial Fulfillment of the Requirements
For the Degree of
Doctor of Philosophy

California Institute of Technology

Pasadena, California

1965

(Submitted 5 April 1965)

ACKNOWLEDGMENTS

This experiment was supervised by Professor Alvin V. Tollestrup, the Principal Investigator, whose interest, suggestions, criticisms and many hours of effort are gratefully acknowledged. His encouragement and advice throughout the last four years of the author's graduate career are sincerely appreciated.

Professor Tollestrup, Dr. Ricardo Gomez, and Dr. Hans Kobrak designed and operated this experiment. The author is deeply indebted to them for their many months of work under trying circumstances. Dr. George Zweig and Mr. Laurie Hatch spent many hours on the preparation and running of this experiment. Mr. Wesley Shanks aided in the preparation stage.

The author is grateful for the support of Professor R. F. Bacher who was director of the laboratory throughout the duration of this experiment.

The many hours of work performed by the scanners were vitally necessary for the analysis of this experiment.

Discussions of physics with Carl Clinesmith, Donald Groom and Charles Peck have been of great value and are happily acknowledged as both pleasant and instructive.

The hospitality of the Lawrence Radiation Laboratory in making the Bevatron facilities available for this experiment is appreciated.

The financial support of the Atomic Energy Commission, the National Science Foundation, and The California Institute of Technology is gratefully acknowledged.

ABSTRACT

A search for the process $K^+ \rightarrow \pi^+ + \pi^o + \gamma$ has been made using counter and spark chamber techniques. The experiment was designed to detect all of the products of the process and measure sufficient quantities to overdetermine the kinematical parameters. Positive pions from K^+ decays at rest were detected in a scintillation counter hodoscope sensitive to pions with energies between 55 and 105 Mev. Positive identification of the π^+ was achieved by observing the $\pi - \mu$ decay on photographs of the hodoscope counter pulses displayed on a fast oscilloscope. The primary photon and the two π^o decay photons were observed by the showers produced in spark chambers constructed of several radiation lengths of steel plate. Additional spark chambers determined the π and K trajectories which, combined with a measurement of photon angles, overdetermine the $K_{\pi 2\gamma}$ kinematics by two parameters.

A total of 4.3×10^6 stopping K's were counted by the apparatus whose overall efficiency for detecting $K_{\pi 2\gamma}$ events is 2.5×10^{-3}. One or possibly two events survived all the $K_{\pi 2\gamma}$ selection criteria. Because approximately one or two background events would be expected to survive the same selection criteria; the results must be presented as an upper limit of about 2×10^{-4} on the $K_{\pi 2\gamma}$ branching ratio for the portion of the π^+ spectrum from 55 to 85 Mev. This upper limit is in agreement with the prediction based on the internal bremsstrahlung mechanism and with other experiments which obtain the branching ratio by another approach.

APPENDICES

I. INTRODUCTION

In the theory of non-leptonic weak decays the $|\Delta I| = 1/2$ rule has enjoyed success and seems to be generally valid (1). As an example of its success, consider the lambda decays:

(1) $\Lambda \rightarrow \pi^{o} + n$;

(2) $\Lambda \rightarrow \pi^{-} + p$.

Invoking the $|\Delta I| = 1/2$ rule predicts

$$\frac{\omega(\Lambda \rightarrow \pi^{-} + p)}{\omega(\Lambda \rightarrow \text{all})} = \frac{2}{3}$$

for the charged mode branching ratio and predicts that the decay asymmetry parameters for both modes should be equal. Experimentally, good agreement is obtained for both numbers; the data are 0.66 ± 0.04 for the branching ratio (2) and

$$\alpha(\Lambda \rightarrow \pi^{o} + n)/\alpha(\Lambda \rightarrow \pi^{-} + p) = 1.10 \pm 0.27$$

for the ratio of asymmetry parameters (3).

One possible failing of the $|\Delta I| = 1/2$ rule is perhaps seen in the results for the following ratio of decay rates,

$$\omega(K^{+} \rightarrow 2\pi)/\omega(K_1^{o} \rightarrow 2\pi) = R.$$

The $|\Delta I| = 1/2$ rule forbids the $K^{+} \rightarrow 2\pi$ process except for electromagnetic effects. One would expect intermediate states with a virtual photon to raise R from zero to the order of $\alpha^2 = 1/(137)^2$. However experimentally, $R \simeq 1/700$ which is a factor of 20 too large.

Cabibbo (4) has constructed an SU(3) theory of non-leptonic decays, which in the limit of SU(3) validity, forbids $K_1^o \to 2\pi$. Since SU(3) symmetry is by no means exact, one still expects to see and does in fact observe $K_1^o \to 2\pi$. If the symmetry breaking interaction does not affect the $|\Delta I| = 1/2$ rule, then it is reasonable to expect R to be increased from α^2 by a factor of 10 or 20(4, 5), thus bringing it in line with experiments. This means that $K_1^o \to 2\pi$ is affected by the SU(3) selection rule while the $K^+ \to 2\pi$ process ($K_{\pi 2}$), which is assumed to be of electromagnetic origin, is not.

However, the simple picture of electromagnetic effects breaking $|\Delta I| = 1/2$ may still be incorrect. Consider the radiative process $K^+ \to 2\pi + \gamma$ which has a real instead of a virtual photon. Here there needs to be only one electromagnetic vertex and therefore one expects the rate of $K^+ \to 2\pi + \gamma$ ($K_{\pi_2\gamma}$) to be only of order α times the $K_1^o \to 2\pi$ rate or even more if Cabbibbo is right. Thus, this theory would say that the $K_{\pi_2\gamma}$ rate ought to exceed the rate of $K_{\pi 2}$, but the experimental evidence to date does not favor a $K_{\pi_2\gamma}$ rate even comparable to $K_{\pi 2}$. It would be interesting to know why this simple picture for electromagnetic effects on the $|\Delta I| = 1/2$ rule is so wrong for $K_{\pi_2\gamma}$.

The radiative decay amplitude has two distinct parts:

(a) the internal bremsstrahlung part where ingoing or outgoing charged particles emit photons; and

(b) a direct emission process where the photon is emitted from virtual intermediate states.

The internal bremsstrahlung contribution is certain to be present and its amplitude is easily computed as a correction to the $K_{\pi 2}$ amplitude (6). Internal bremsstrahlung alone gives a branching ratio of 1.6×10^{-4} for the part of the π^+ spectrum between 55 and 80 MeV but it is the direct term that is of greater interest for it is here that the $|\Delta I| = 1/2$ rule comes into play.

Attempts to compute the direct amplitudes are more speculative and generally contain poorly determined parameters. For example, a theory by Cabibbo and Gatto (7) contains a poorly determined ratio of coupling constants and an unknown sign for the interference between the direct term and the internal bremsstrahlung term. The hope here is that the shape of the experimental spectrum will identify the dominant terms. Some of the curves from this theory are shown in Figure 1, namely: (a) pure inner bremsstrahlung, (b) destructive interference between inner bremsstrahlung and the direct term, and (c) the constructive interference of the two terms. The direct term, which is not shown goes to zero at both T = 0 and T = 108 MeV and has a broad maximum at around 70 MeV. In the region of 55 to 75 MeV the rate for (b) is comparable with the rate for (a) while the rate for (c) is a factor of five larger. The experimental data will be discussed shortly.

Other theoretical models either use specific intermediate states (8, 9), or compute effects of final state pion-pion interactions (10, 11) or are purely phenomenological (12, 13). All models predict rates for $K_{\pi_2 \gamma}$ which are within a factor of ten of the purely inner

FIGURE 1

DATA AND THEORY FOR π^+ SPECTRUM FROM $K_{\pi_2\gamma}$

Figure 1 is a copy of a plot from Reference 20. The ordinate, $d\omega/dT$, is the transition rate per unit energy plotted as a function of the π^+ kinetic energy, T. The energy unit in $d\omega/dT$ is the pion mass. The scale of the ordinate is to be multiplied by 10^{+5}; for example curve (c) crosses at $d\omega/dT = 2.0 \times 10^5$.

Curve (a) is the theoretical spectrum for pure inner bremsstrahlung while curve (b) is the spectrum for destructive interference between inner bremsstrahlung and Gabibbo's direct term and, (c) the constructive interference of the two terms. The data of Cline and Fry is plotted with statistical error flags. P_a and P_b are the χ^2 probabilities that curves (a) and (b) respectively fit the data in the kinetic energy region 55 to 85 MeV.

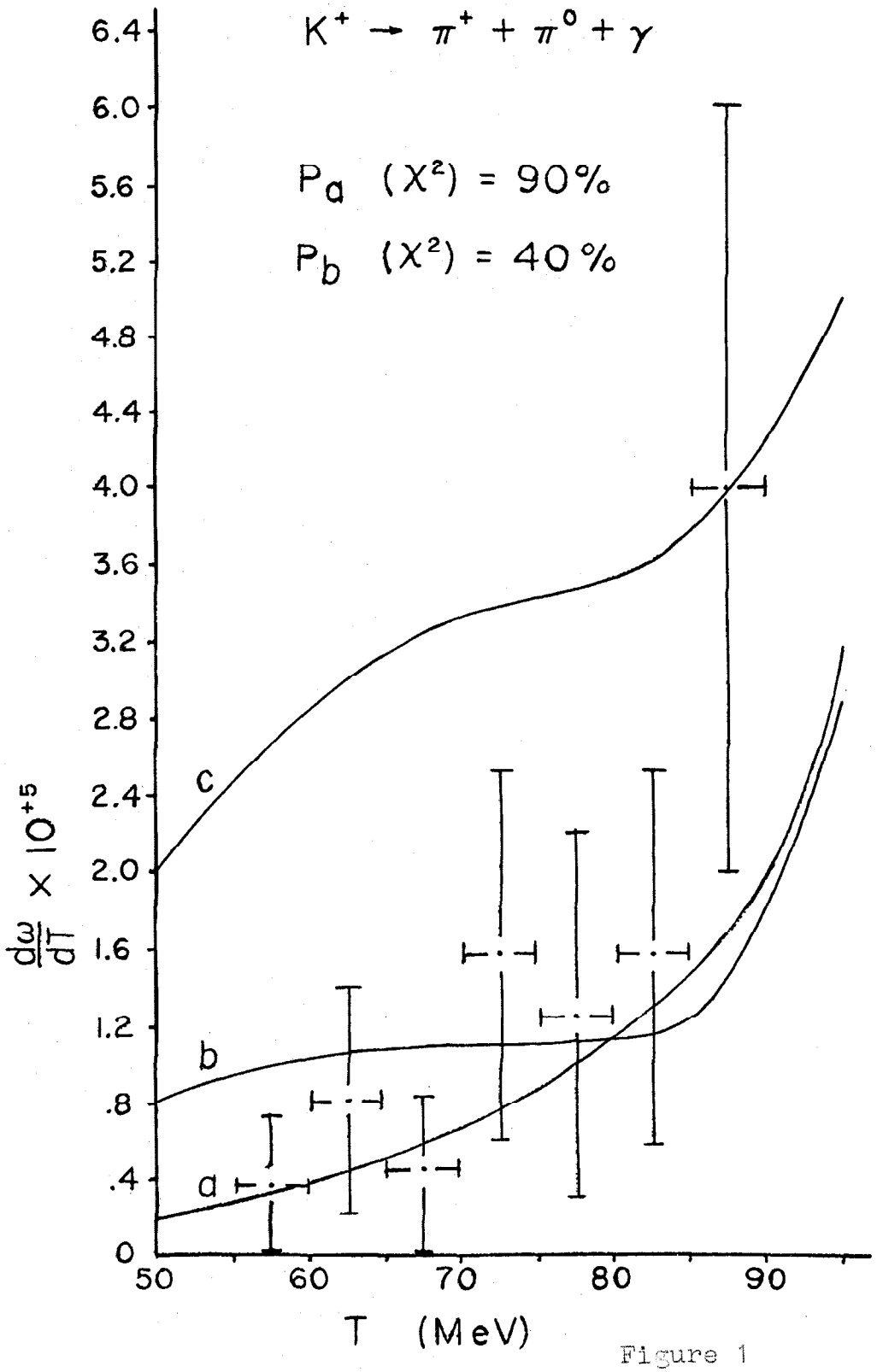
$K^+ \rightarrow \pi^+ + \pi^0 + \gamma$
P_a (X^2) = 90%
P_b (X^2) = 40%
$\frac{d\omega}{dT} \times 10^{+5}$
T (MeV)
a
b
c
6.4
6.0
5.6
5.2
4.8
4.4
4.0
3.6
3.2
2.8
2.4
2.0
1.6
1.2
.8
.4
0
50
60
70
80
90

Figure 1

bremsstrahlung rate for reasonable values of the unknown parameters. They will not be considered further because there is no compelling reason to expect dominence of the rate by any one of the specific mechanisms and because the existing data are not sufficiently precise for a meaningful comparison with competing theories.

To completely specify the $K_{\pi_2\gamma}$ process would require knowing the rate, differential in two independent kinematic variables, say the π^+ energy and the $\pi^+ - \gamma$ angle, as well as knowing the γ polarization as a function of two independent variables. Experiments to measure these quantities in detail would provide a maximum of information about $K_{\pi_2\gamma}$. Such experiments, however, are difficult to perform, particularly the measurement of the γ polarization. Less detailed information such as the total rate, or the spectrum for a single variable such as the π^+ energy, might be sufficient to isolate the effects of the direct term from the inner bremsstrahlung term.

One way to detect possible $K_{\pi_2\gamma}$ decays is to search for intermediate range π^+ secondaries. Of the known K^+ decays shown in Table I, only two, $K_{\pi 2}$ and τ', have just one charged pion secondary. A glance at the energy spectra from these two decays shows that the range from 0 to 53 MeV is occupied by τ' secondaries, which is then followed by a gap to 108 MeV where the monoenergetic π^+ from $K_{\pi 2}$ occurs. If the $K_{\pi_2\gamma}$ mode exists, then it can have a π^+ secondary that falls in this gap. The only other known modes which

TABLE I

K^+ DECAY DATA

Decay Mode	Branching Ratio (14) (%)	Kinetic Energy Range of Charged Secondaries for Decay at Rest (MeV)
$K^+_{\mu 2} \rightarrow \mu^+ + \nu_\mu$	64.2 ± 1.3	Monoenergetic 152.6
$K^+_{\pi 2} \rightarrow \pi^+ + \pi^o$	18.6 ± 0.9	Monoenergetic 108.6
$K^+_{\mu 3} \rightarrow \mu^+ + \pi^o + \nu_\mu$	4.8 ± 0.6	0.0 - 134.1
$K^+_{e3} \rightarrow e^+ + \pi^o + \nu_e$	5.0 ± 0.5	0.0 - 228.0
$\tau^+ \rightarrow 2\pi^+ + \pi^-$	5.7 ± 0.3	0.0 - 48.2
$\tau'^+ \rightarrow \pi^+ + 2\pi^o$	1.7 ± 0.2	0.0 - 53.3
$K^+_{e4} \rightarrow e^+ + \pi^+ + \pi^- + \nu_e$	$(2.3 \pm 0.7) \times 10^{-3}$ Ref. 15	e 0.0 - 160.0 π 0.0 - 107.3
$K^+_{\mu 4} \rightarrow \mu^+ + \pi^+ + \pi^- + \nu_\mu$	$\sim 1.4 \times 10^{-3}$ Ref. 28	μ 0.0 - 75.1 π 0.0 - 43.7
$K^+_{\pi_2 \gamma} \rightarrow \pi^+ + \pi^o + \gamma$	$\sim 10^{-2}$ ( )	0.0 - 108.6

can reach this gap with π^+ secondaries are the K_{e4} and $K_{\mu 4}$ modes which are very rare and have three charge secondaries.

Until recently the experimental evidence for the radiative decay, $K_{\pi_2\gamma}$, has rested with three anomalous events observed in 19,000 K^+ decays in emulsions. G. Harris, et. al.(16) find one π^+ secondary with an energy of 60 MeV in 5000 K^+ decays; Prowse, et. al.(17) find a π^+ secondary with 62 MeV in a sample of 353 K^+ decays; and D. Monti, et. al.(18) find a π^+ secondary of 70 MeV in a sample of 9000 decays, only 30 of which they claim are properly examined for $K_{\pi_2\gamma}$. Others (19) have examined 5496 events observing no anomalies of the above kind. In all cases the secondaries are followed to the end of their range and the π-μ decay is seen. These three anomalous events described above are interesting because they have π^+ energies in the gap between τ' and $K_{\pi 2}$, where no previously observed K^+ decays can reach.

Recently Cline and Fry (2) have observed eighteen short range π^+ secondaries showing the characteristic π-μ-e decay chain in a sample of 165,000 stopping K^+ decays in a freon bubble chamber. Like the three emulsion anomolies the π's here had energies between the τ' maximum and the monoenergetic $K_{\pi 2}$ energy. Cline and Fry did not observe all the photons because the conversion probabilities for the γ's were too low to allow all three γ's to be seen, although a few events did have one or two converted photons. Therefore, their events are in the same class as the emulsion events, namely events identified by the range of the π^+ secondary from a stopping K^+ decay where π-μ-e decay chain or π-μ decay gives positive identification of the π^+.

A very plausible explanation of the anomalous events seen so far is to say that they are examples of $K^+ \rightarrow \pi^+ + \pi^o + \gamma$. Other possibilities include:

(1) $K^+ \rightarrow \pi^+ + 2\gamma$;

(2) $K^+ \rightarrow \pi^+ + \nu + \bar{\nu}$.

Process (1) was excluded by Harris, et.al. (16) on the basis of an order of magnitude estimate by Dalitz, while (2) can be excluded because it would mean the existence of neutral currents for weak processes, which have not been required to date.

It is possible that the events so far seen are π^+ from $K_{\pi 2}$ that have scattered inelastically, thereby producing a short range π^+. Such scatters can often be detected by observing an abrupt change in direction of the π^+, a proton knock-on, or a change in the ionization $(\frac{dE}{dx})$ of the π^+. The emulsion workers use all three indications while Cline and Fry use the first two only. If the inelastic scatter occurs after the π^+ has gone some distance, then it has a good chance of being detected, but an inelastic scattering close to the K^+ vertex unaccompanied by a visible proton knock-on cannot be detected because a change in direction or ionization would not be detected. Cline and Fry estimate that two of their eighteen events are due to this contamination, while Harris, et.al., estimate a relative probability of 10^{-9} for this possibility.

As was mentioned earlier the inner bremsstrahlung mechanism alone predicts a branching ratio (compared to all K^+ decays) of 1.6×10^{-4} for the part of the spectrum between 55 and 80 MeV. The

three emulsion events are consistent with this rate if the efficiency for detecting intermediate range π's is of the order of unity. The 18 events of Cline and Fry yield a branching ratio of $(2.2 \pm 0.7) \times 10^{-4}$ which is also consistent with inner bremsstrahlung; furthermore, their π^+ spectrum, which is plotted with statistical error flags in Figure 1, agrees, within statistics, with that predicted for inner bremsstrahlung (curve a).

There is some question about the branching ratio determined from the emulsion events. D. Monti, et. al., (18) consider that only 30 of their 9000 events were examined properly for $K_{\pi_2\gamma}$. This is because the emulsion scans were set up to look for τ' or to study the $K_{\mu 3}$ spectrum out to about 60 MeV and so employed ionization cutoffs which guarantee complete detection of these events, but which are not particularly efficient for detecting π's much beyond 75 MeV. They re-examine the world data and conclude that only 4000 of the emulsion events have been properly analyzed in a way suitable to detect K decays. They quote a ratio of 8×10^{-4} for the π^+ energy range 55 to 80 MeV, which they say is probably underestimated by a factor of 2 because of inefficiencies in the detection procedure, especially near 80 MeV.

The data of Cline and Fry on the π^+ spectrum shown in Figure 1 are consistent not only with a pure inner bremsstrahlung rate alone but also with the destructive interference (curve b) of Cabibbo's direct term with inner bremsstrahlung. More data on the π^+ spectrum alone, if it continues to look like the data of Figure 1,

will probably not allow one to disentangle the direct amplitude from internal bremsstrahlung. However, more information can be obtained if one observes in more detail the rate as a function of the two variables needed to completely specify the kinematics of $K_{\pi_2\gamma}$ in the rest system of the K. By observing the distribution of one other variable in addition to the π^+ energy, for example, the $\pi^+ - \gamma$ angular correlations or the photon energy; or by observing the joint distribution as a function of two variables instead of the spectrum of a single variable, it may be possible to isolate the direct term.

In view of the present experimental and theoretical uncertainties concerning the direct amplitude it would be an interesting experiment:

(a) to observe directly the products of the $K^+_{\pi_2\gamma}$ mode and verify the kinematics and

(b) to obtain enough events to characterize the distribution of two independent variables which specify the decay.

At the time that the present experiment was being designed, the data of Cline and Fry did not exist. The rate was more uncertain then; even so, the goal of the experiment was to get more than just the rate. This thesis describes an attempt to carry out such a program; but unfortunately, the difficulties encountered in getting the experiment operational before an unavoidable deadline at an accelerator 400 miles away considerably compromised these objectives.

II. EXPERIMENTAL DESIGN AND PROCEDURE

The experiment was designed to detect $K_{\pi_2\gamma}$ decays by identifying all the decay products and to measure sufficient parameters to more than determine the kinematics. In this section the main features of how this was supposed to be done will be briefly discussed. More details of some aspects, specifically on the K^+ beam design and the triggering scheme, are available in Appendix I.

A. Design Considerations

There are three facts about the process $K^+ \rightarrow \pi^+ + \pi^o + \gamma$ around which this experiment was designed:

(1) The process is rare with a branching ratio somewhere in the order of 10^{-4} to 10^{-3}. It is rare when compared to any other K^+ decay mode except K_{e4} and $K_{\mu 4}$.

(2) The π^+ energy range of 53.3 to 108.6 MeV is inaccessible to π^+ from any of the other known K^+ decay modes except the very rare K^+_{e4} and $K^+_{\mu 4}$ modes. The observed K^+_{e4} and $K^+_{\mu 4}$ modes, however, produce three charged secondaries.

(3) The other products besides the π^+ are three photons, one from the primary decay and two from the decay of the π^o.

Because of (1) the main problem of any practical experiment to study $K_{\pi_2\gamma}$ is twofold:

(a) to obtain in some feasible manner with known efficiency for retaining $K_{\pi_2\gamma}$ events, a sample of K^+ decays considerably enriched in $K_{\pi_2\gamma}$ events and

(b) to establish a procedure for positively identifying $K_{\pi_2\gamma}$ in the midst of contaminations from other decay modes.

The experimental technique which seeks to utilize consideration (2) above to identify $K_{\pi_2\gamma}$ solely by the presence of a single intermediate range π^+ and neutrals has two disadvantages. First, the energy of the π^+ does not completely specify the kinematical quantities for the unobserved π^o and γ. Secondly, the range technique to measure π^+ energy may confuse π^+'s from $K_{\pi 2}$, which inelastically scatter, with those intermediate energy π^+'s from $K_{\pi_2\gamma}$. However, by detecting the three photons accompanying the radiative decay, all ambiguities can in principle be resolved.

A $K_{\pi_2\gamma}$ decay at rest is shown schematically below; where π^+, π^o, and γ are the products from the primary decay and γ_1 and γ_2 are the photons from the π^o decay. Identifying the π^+, K^+ and the three photons and measuring the three γ directions, the π^+ energy and direction is sufficient to overdetermine the kinematics for $K_{\pi_2\gamma}$. For a $K_{\pi_2\gamma}$ decay at rest one has the following five kinematic equations:

$$P_{\pi^+}\vec{\ell}_{\pi^+} = k\vec{\ell} + k_1\vec{\ell}_1 + k_2\vec{\ell}_2$$

$$E_{\pi^+} + k + k_1 + k_2 = M_K$$

$$M^2_{\pi^o} = 2 k_1 k_2 (1 - \vec{\ell}_1 \cdot \vec{\ell}_2)$$

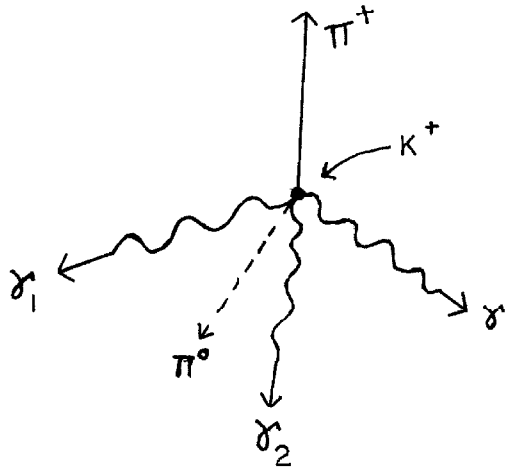

where $\vec{\ell}_{\pi^+}$, $\vec{\ell}$, $\vec{\ell}_1$, $\vec{\ell}_2$ are unit vectors in the direction of the π^+ and the three photons and where P_{π^+}, E_{π^+}, k, k_1, k_2, M_K, M_{π^o} are the π^+ momentum and energy, the three photon energies and the K^+ and π^o masses respectively. There are three unknown parameters, i.e., the three photon energies; therefore, the $K_{\pi_2\gamma}$ kinematics are overdetermined by two parameters and desirable consistency checks can be made. The situation is somewhat complicated by not knowing which of the three photons came from the primary decay. In this experiment the overdetermination was utilized by making maximum likelihood fits to the kinematic parameters for each of the three different combinations of photons and then picking the combination with the smallest χ^2 as the one with the proper photon assignment. The χ^2 "goodness of fit" criterion can be used to check the consistency of the measurements with $K_{\pi_2\gamma}$ hypothesis.

B. Experimental Design

With the above facts and considerations in mind an experiment was designed which could detect large numbers of K^+ decays at rest in the laboratory, select a sample enriched in $K_{\pi_2\gamma}$ decays and record enough information which, when analyzed in detail, should yield positive identification of the $K_{\pi_2\gamma}$ events. The apparatus separates naturally into three sections:

(1) The K^+ telescope which detects K^+'s coming to rest near the center of the apparatus,

(2) The π^+ range hodoscope which detects and determines the range of intermediate range π^+'s from K^+ decays. Discrimination against decay modes other than $K_{\pi_2\gamma}$ is provided for by designing the hodoscope to have a range acceptance window between the range of a 53 MeV and 108 MeV π^+.

(3) The spark chamber assembly which consists of five γ detecting spark chambers and two other spark chambers which measure the π^+ and K^+ trajectories.

The three sections will be discussed in more detail shortly. Figures 2 and 3 show diagrams of the apparatus in place. Figure 2 is a front view of the experimental layout showing the FC-75 stopper where the K's were brought to rest, the various spark chambers with a typical event configuration depicted, and the scintillation counters of the π^+ range hodoscope. Figure 3 is a side view of the apparatus in place. In addition to what is shown in Figure 2, this

FIGURES 2 AND 3

EXPERIMENTAL LAYOUT

Figures 2 and 3 are drawings of the experimental layout, i.e., the π^+ hodoscope, the spark chambers, and a portion of the K^+ telescope. Not all of the γ chamber plates are shown, nor are the phototubes on the counters shown. A possible $K_{\pi_2\gamma}$ event as it might appear in the experiment is shown in the drawings of Figures 2 and 3.

In Figure 2 the K^+ beam is perpendicular to the plane of the paper while in Figure 3 it is in the plane of the paper. Figure 3 shows the most detail of the K^+ telescope: the positions of the 0-75 and H_2O Cerenkov counters, the Al absorber, the K chamber, the "dE/dx" counter (labeled S_K), and the FC-75 stopper appear in the center of Figure 3.

The π^+ hodoscope counters are the ones labeled 1A through 6A and 1B through 6B. The Aluminum prescessor in the position between 3B and 5B is equivalent in stopping power to 1 and 3/4 inches of scintillator plastic. Beyond the π^+ hodoscope lie the counters and Aluminum precessors used for the high energy point in the $K_{\mu 3}$ experiment. The Copper absorber between channel 6 and 8 is used to prevent π^+'s from $K_{\pi 2}$ from reaching the counters of the $K_{\mu 3}$ experiment. The lucite wedge below the π^+ hodoscope and above the π chamber compensate for variations in range due to variation in the π^+ direction.

Figure 2 shows the labeling of the γ chambers that is used throughout the thesis. The shielding is not shown in any of the drawings.

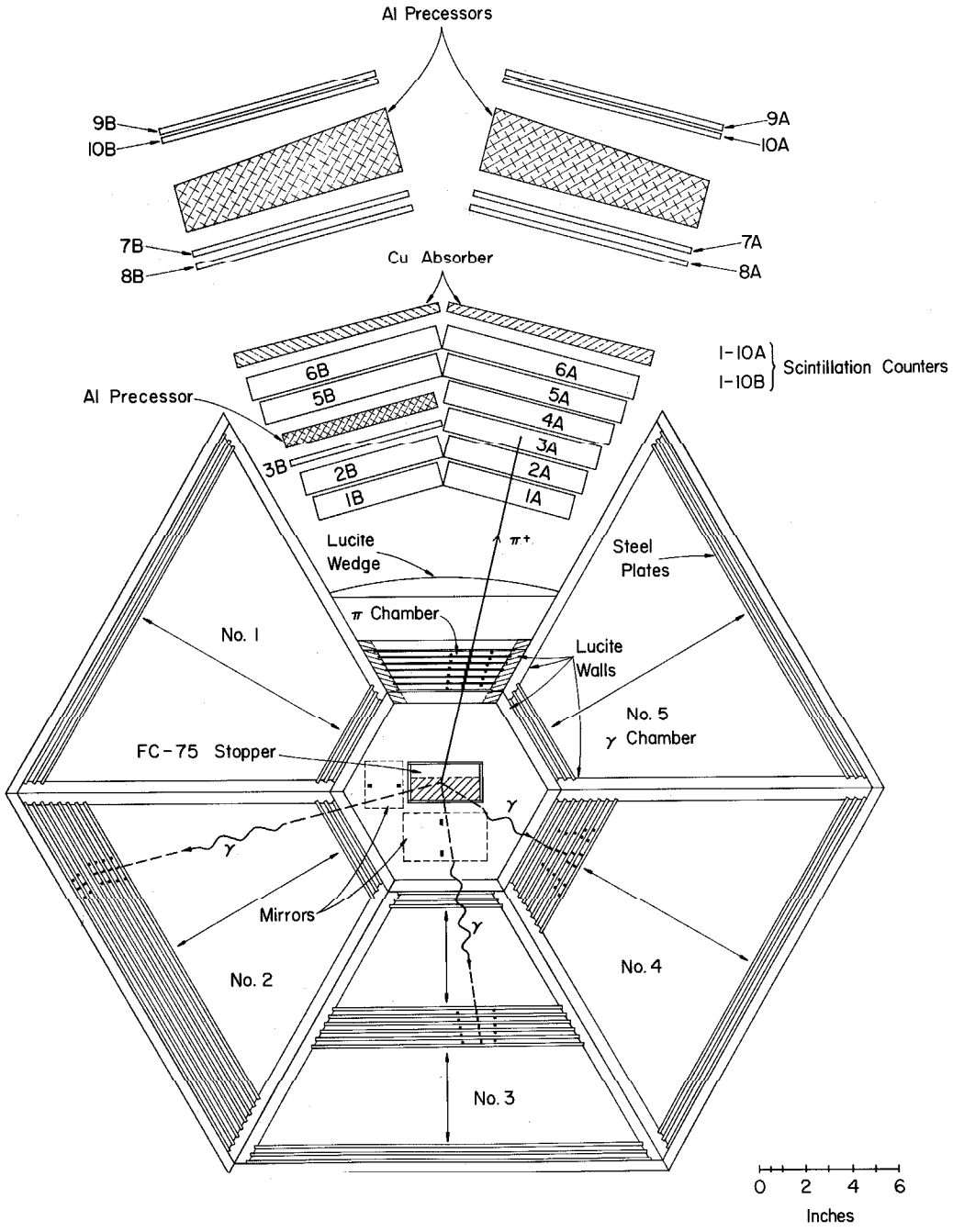

Experimental Layout - Front View

Figure 2

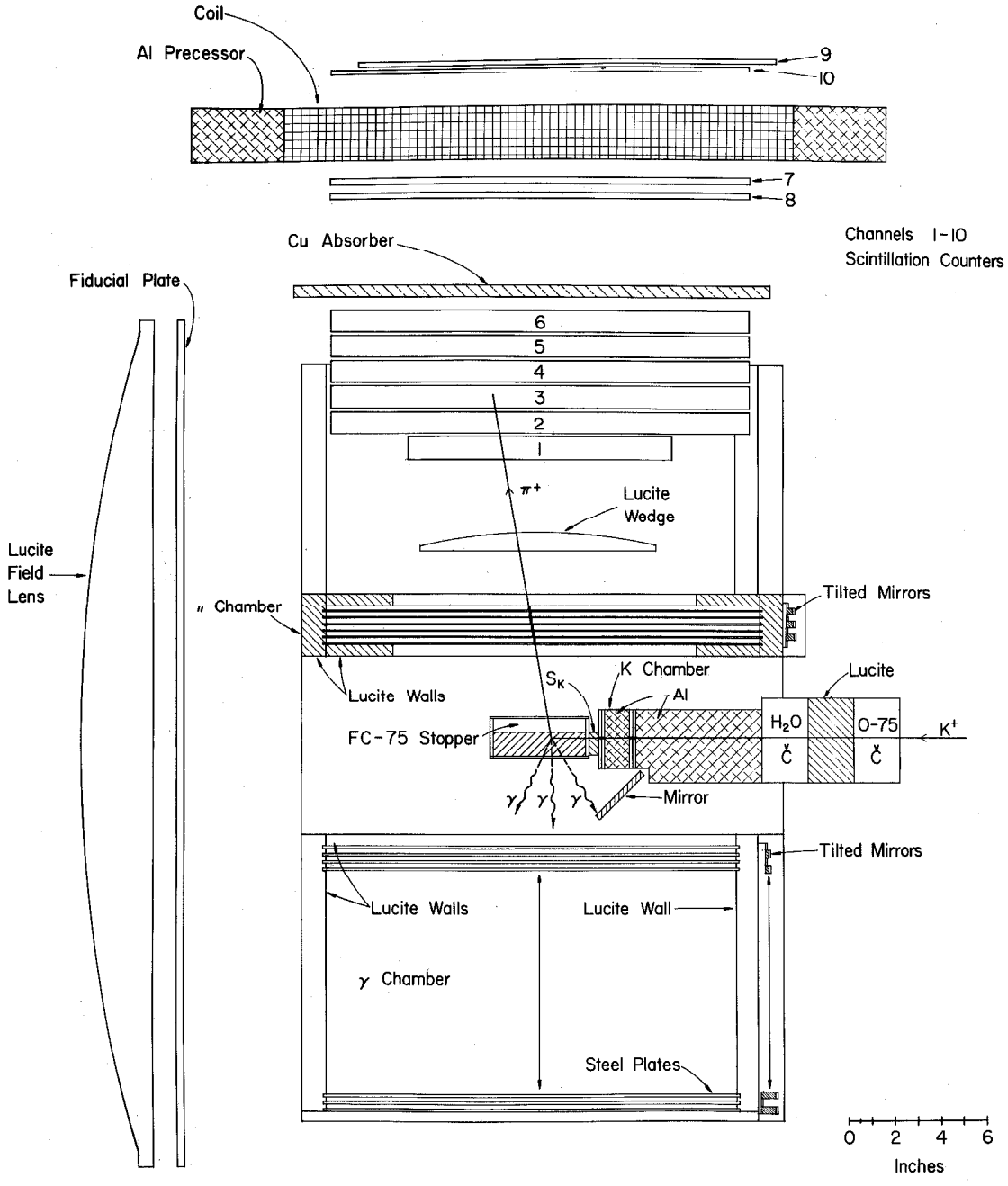

Experimental Layout – Side View

Figure 3

FIGURE 4

PHOTOGRAPHS OF EXPERIMENTAL APPARATUS

Figure 4 is a collection of four photographs which give an idea of the physical arrangement of the apparatus and auxilliary equipment. Figures 4a and 4b show the spark chambers, field lens and counter assemblies in place and surrounded by magnetic and electrostatic shielding. The apparatus without the field lens is shown in Figure 4c and Figure 4d shows the room housing the racks of electronics.

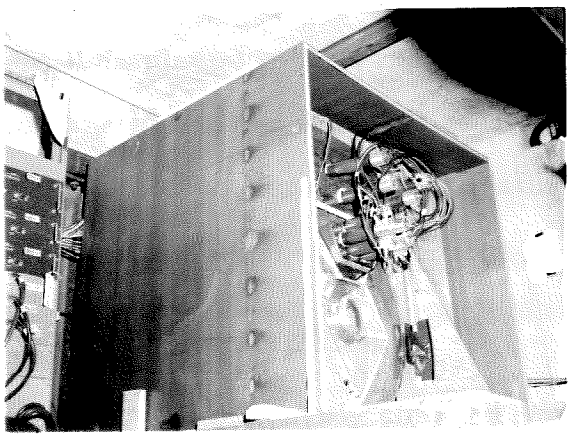

a

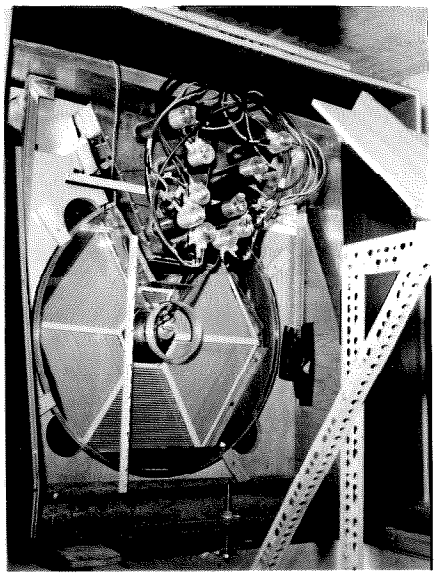

b

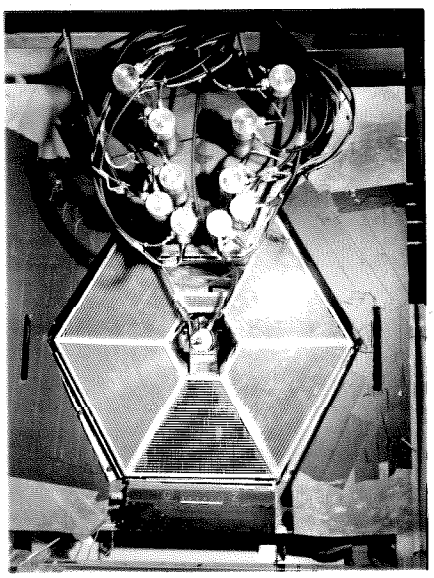

c

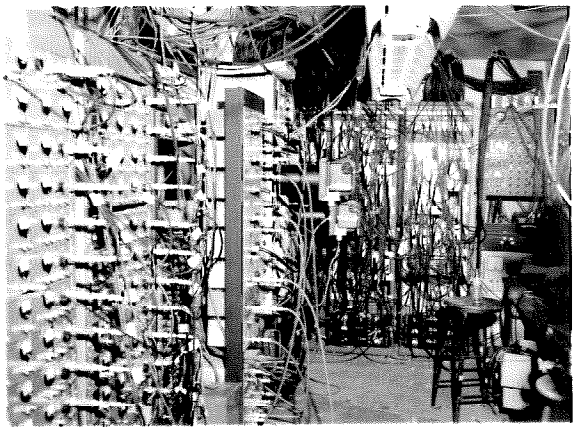

d

Figure 4

view shows most of the counters of the K telescope as well as the field lens placed in front of the spark chambers. Figure 4a and 4b show the spark chambers, field lens, and counter assemblies in place, while 4c shows the apparatus from the front without the field lens and 4d shows the room housing the racks of electronics.

1. The K^+ Beam

A positively charged, momentum analyzed, secondary beam from an internal platinum target of the Lawrence Radiation Laboratory's Bevatron was focused on a stopper of FC-75, a flurocarbon liquid composed mainly of isomers of perfluro cyclic ether, $C_8F_{16}O$. The first counter, which is not shown in Figure 3, is the Fitch counter, a type of Cerenkov counter described in more detail in Appendix I. The Fitch counter gives a pulse for K's but not for π's or protons. The K's are slowed down in passing through the 0-75 and H_2O Cerenkov counter, the aluminum absorber, the scintillation counter, S_K, and come to rest in the FC-75 stopper. The K's are below the Cerenkov threshold in both the H_2O and 0-75 counters as well as the FC-75 stopping counter while any π's in the beam are above the threshold and will produce pulses in all three counters and will not stop in the stopper. At the S_K counter π's are still minimum ionizing but the K's are three or more times minimum. Any protons in the beam will stop well before the stopping counter. By utilizing this series of velocity sensitive Cerenkov and scintillation counters placed as they were in the beam, a very reliable K^+ signature was obtained.

The FC-75 material in the stopping counter and the 0-75 counter has a low refractive index of 1.27 and therefore a velocity threshold of $\beta = 0.79$ for Cerenkov radiation. The FC-75 counter served also as a threshold Cerenkov counter which gave pulses when a fast particle like a μ from $K_{\mu 2}$ with $\beta = 0.91$ or a π from $K_{\pi 2}$ with $\beta = 0.83$ emerged from a K^+ decay in the stopper.

The K^+ beam was designed and prepared by Professor Alvin Tollestrup and Dr. George Zweig. For more details see Appendix I.

2. The π^+ Hodoscope

The pion hodoscope consisted of two scintillation counter telescopes composed of six one-inch-thick plastic scintillation counters each. The hodoscope counters are the ones labeled 1A through 6A and 1B through 6B in Figures 2 and 3. The nomenclature Channel 1, Channel 2, etc. is used when speaking of either the 1A or 1B counters, etc. Pions in the energy range of interest would stop in one of the six channels and decay promptly into a 4 MeV μ and a neutrino. The π lifetime is large enough so that for a reasonable fraction of the time ($\sim 1/2$) the stopping π pulse and the μ pulse are sufficiently separated in time to be distinguished. The fast circuitry designed by Professor Tollestrup and Dr. Ricardo Gomez was used to detect these conditions electronically.

Three measurements contribute to the total π^+ range. First, the range in the stopping counter is determined from a measurement of the pulse height in the stopping counter. Secondly,

the range in the rest of the hodoscope is computed from the direction of the π^+, which is determined from measurements in a spark chamber, and from knowledge of how many counters the π^+ traversed. The third contribution is the range in the stopping counter and the spherical wedge between the π chamber and the hodoscope. Computing this contribution requires knowing the π^+ direction and the origin of the decay.

In the actual operation of this experiment there were additional counters beyond the π counters. These counters were used to detect μ's from $K_{\mu 3}$ and measure the up-down asymmetry of the μ decay as a way of studying the μ polarization. The triggering rates for both experiments were low enough so that they could be run simultaneously. Very little more will be said about the $K_{\mu 3}$ experiment except as it affects the $K_{\pi_2 \gamma}$ experiment.

In order to observe the π-μ decay, to get the range in the stopping counter, and to verify that the triggering requirements were met, the pulses from the π^+ hodoscope as well as some from the K^+ telescope were displayed on a fast oscilloscope and photographed. This display will be referred to as the "fast display". An additional slower oscilloscope display with information from both the $K_{\pi_2 \gamma}$ and the $K_{\mu 3}$ experiments was also photographed and will be referred to as the "slow display". This display was necessary for the $K_{\mu 3}$ polarization experiment, but it also afforded a means of identifying which event belonged with which experiment.

3. Spark Chambers

The photon detecting spark chambers, which were designed primarily by Dr. Hans Kobrak, contained approximately four conversion lengths of steel plates (36 plates 1/8 inch thick) in each chamber. The trapezoidal shape allowed for an approximately cylindrical geometry around the stopper with the advantage that the trajectories are more nearly perpendicular to the plates than is the case with a rectangular arrangement. To get a measure of a spark's depth (z coordinate) in a chamber, two tilted mirrors were placed in back of each gap. The displacement of the reflection from the main spark as viewed in the plane of the photographic film is related to the depth in a simple way.

The π chamber employed to measure the π^+ trajectory was similar in design to the γ chambers except that it was smaller and had thin aluminum plates. The K chamber was a small, four gap chamber with 90° stero views and was placed next to the "dE/dx" (S_K in Figures 2 and 3) counter in front of the stopper. A lucite field lens was placed in front of the spark chamber assembly and a camera placed at its focus.

Figure 5 illustrates the spark chamber measurements used for kinematic fitting. The π and K chamber tracks extrapolate back to give the decay vertex, which when combined with measurements of the points of conversion of the photon determine the photon angles. The π^+ pulse height in the stopping counter determines the range of the π^+ in that counter while the rest of the π^+ range comes

FIGURE 5

SPARK CHAMBER EVENT CONFIGURATION AND MEASUREMENTS

This diagram shows the features of a $K_{\pi_2\gamma}$ event configuration which are essential for measurement in this experiment. The K^+ enters the stopper at $\vec{P}_K$, comes to rest at $\vec{R}_o$ and decays. the π^+ emerges from the stopper at $\vec{R}_4$ and passes through the middle of the π chamber at the point $\vec{R}_5$ on its way to the hodoscope. The primary photon converts at $\vec{R}_1$ and the two π^o photons at $\vec{R}_2$ and $\vec{R}_3$ respectively.

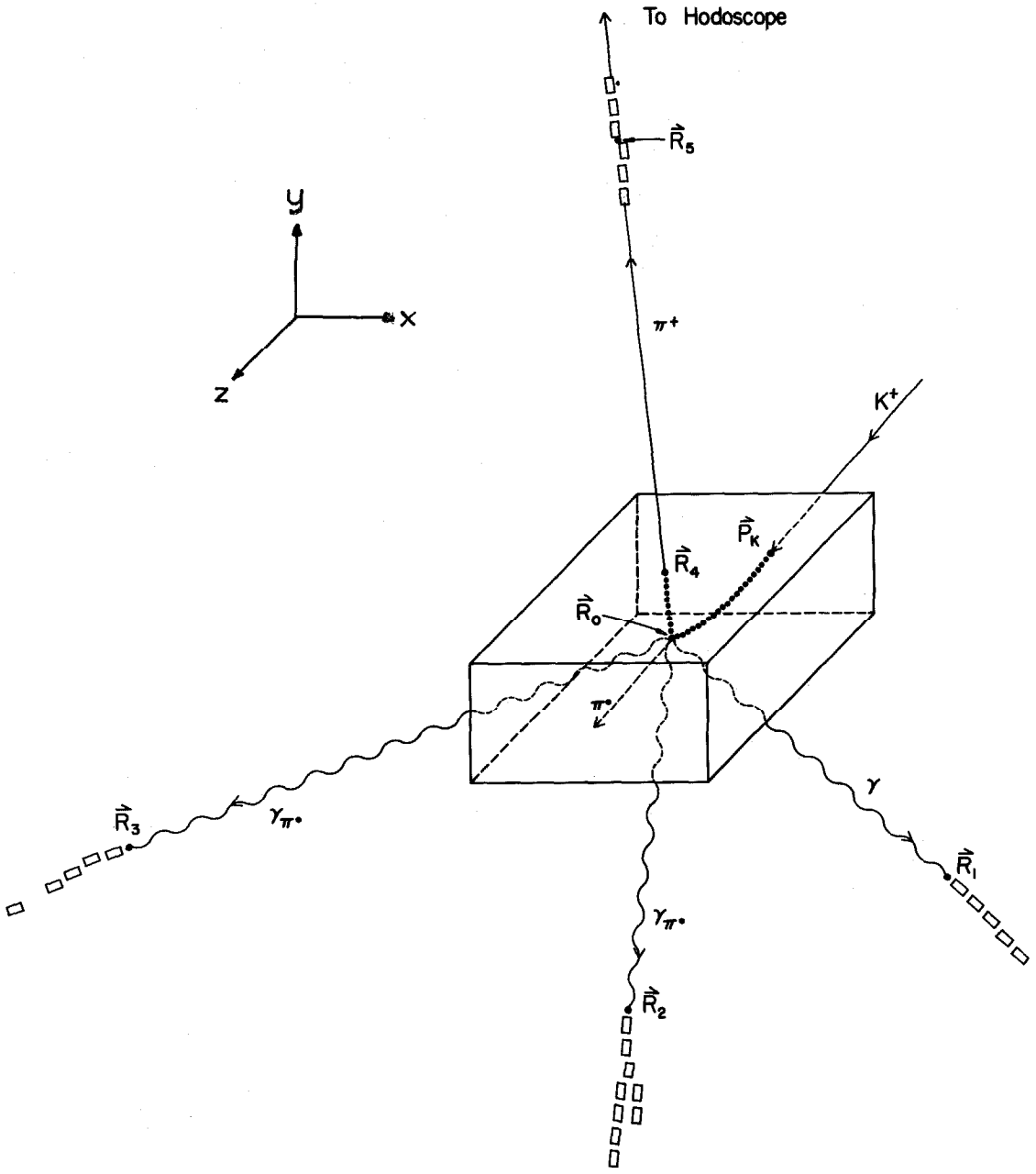
To Hodoscope
$\vec{R}_5$
y
x
z
π^+
K^+
$\vec{P}_K$
$\vec{R}_4$
$\vec{R}_o$
π^o
γ
$\vec{R}_3$
γ_{π^o}
$\vec{R}_1$
γ_{π^o}
$\vec{R}_2$

Figure 5

from geometry; that is to say, the decay vertex and π^+ direction specify the range in the stopper and the range in the counters up to the stopping counter. With the π^+ identity known, the range then determines the energy so that the π^+ kinematics are completely specified. The γ angles, the π^+ energy and direction, and the masses of all particles involved are sufficient to overdetermine the $K_{\pi_2\gamma}$ kinematics by two parameters.

4. The $K_{\pi_2\gamma}$ Triggers

A $K_{\pi_2\gamma}$ trigger was generated when the electronics detected a stopping K^+ signature followed shortly (a few K lifetimes) by a stopping π^+ signature in the hodoscope. The stopping π^+ signature required that the particle stop in one of the six counters of the hodoscope and produce a second pulse in the stopping counter that overlapped in time a 100 ns gate which was delayed by approximately 12 to 15 nanoseconds. The later requirement constituted an electronic mans of requiring the π-μ decay. The $K_{\pi_2\gamma}$ trigger caused the spark chambers to fire, triggered the oscilloscopes, and advanced the cameras. Appendix I describes in more detail the $K_{\pi_2\gamma}$ triggering requirements and logic.

For positive identification of $K_{\pi_2\gamma}$ the π-μ decay of the stopping π^+ must be seen in the photographs of pulses from the counter where the π^+ stopped. In addition, the measurements on the shower tracks seen in the spark chamber and on the π^+ range and direction must fit the $K_{\pi_2\gamma}$ kinematics.

5. Anticipated Rate

The beam at the Bevatron was dumped eleven times per minute and an average of 275 K's were detected in the K telescope for each spill. The hodoscope solid angle was about 5% of a sphere while the γ chambers had an efficiency of approximately 15 to 20%, depending of course on the spectrum, for seeing the three photons from the $K_{\pi_2\gamma}$ decays. With a π-μ efficiency of 50% and a branching ratio of 3×10^{-4} for the part of the π^+ spectrum sampled one would expect one and one half $K_{\pi_2\gamma}$ events to be seen per million stopped K's or about three events per half day, or 60 events in 20 half days, assuming negligible down time. If the branching ratio is higher, of course more events would be seen.

C. Data Collected

For each event triggering the experimental apparatus, a separate photographic record on 35 mm film was made of each of the following items:

1. the slow display oscilloscope,
2. the fast display oscilloscope,
3. the spark chambers.

Sample photographs plus detailed descriptions of the pulse patterns for both the slow and fast displays are available in Appendix II. Some photographs of the spark chambers for certain events are shown in Section III F 4.

The slow display oscilloscope displayed pulses from all the counters in the π^+ hodoscope as well as those in the $K_{\mu 3}$ experiment. Thus, pulses from counters 1A through 10A and 1B through 10B were recorded. Time relationships relative to the event trigger were preserved. A $K_{\pi_2\gamma}$ trigger is characterized by a pulse pattern starting at t = 0 containing only pulses from channels 1 up to the channel in which the π^+ stopped which will not be beyond channel 6. A $K_{\mu 3}$ trigger will show pulses from the μ decay electron in channels 7 and 8 or 9 and 10 at t = 0 plus a pattern of pulses from channels 1 through 8 at an earlier time.

The fast display oscilloscope displayed the Fitch counter and the dE/dx (S_K) counter pulses from the K^+ telescope and pulses from counters 1A through 6A plus 1B through 6B of the π^+ hodoscope. One additional pulse, the FC-75 counter pulse, was also shown on the fast display. Time relationships relative to the K^+ signal were preserved for all pulses. The sweep speed was 30 ns/cm. The purpose of the fast display was to record accurate pulse height and time information for $K_{\pi_2\gamma}$ triggers. Pulses associated with the $K_{\mu 3}$ triggers generally came too late in time relative to the K^+ signal to appear on the fast display.

The spark chamber photographs were taken with the camera at the focus of the field lens in front of the experimental assembly. The five γ chambers, the π chamber and the K chamber were recorded on these photographs.

The number of K^+ decays detected by this experiment in the actual operation was nearly a factor of 10 fewer than were planned for. The primary reason for this was that most of the allotted time was spent setting up and checking out equipment instead of taking "good" data. At one point the spark chambers stopped working and needed extensive repair. As a result the data consists of two parts, that taken before and that taken after the spark chambers broke down. Because the first portion observed fewer K-decays, requires separate calibrations, and contains an unknown number of frames where the spark chamber efficiency was poor, it was not analyzed. The second portion offered the best hope for yielding a result; if it proved to be barren, then the first portion would not change that result.

In all 58 runs were made and 6.6×10^6 K^+ signatures counted and 18,066 events were photographed. Of these, 26 runs, 7,529 events and 2.3×10^6 K^+ signatures occurred in the first portion of the experiment before the breakdown and 32 runs, 10,437 events, and 4.3×10^6 K^+ signatures in the second portion.

III. DATA ANALYSIS

A. General Considerations

In the portion of the experiment which was analyzed 4.3×10^6 K^+ signatures were counted and 10,437 events satisfying the $K_{\pi_2\gamma}$ or $K_{\mu 3}$ logic were photographed. Of these 10,437 events, the slow display showed that 5,584 satisfied the requirements for $K_{\pi_2\gamma}$ triggers. (See Appendix II for details of the slow display considerations and a sample photograph.) These 5,584 $K_{\pi_2\gamma}$ triggers constitute the data for the rest of the analysis.

Because the $K_{\pi_2\gamma}$ events are rare compared to $K_{\pi 2}$ and τ' decays, the criterion for good events must be very efficient for rejecting false events and reasonably efficient for accepting good events. The possibility of backgrounds of one form or another swamping the desired events is a real worry in this type of experiment. The triggering rate was low, approximately one trigger per 10^3 K stops or per 6×10^4 π's through the stopper, but was still large compared to the rate expected from $K_{\pi_2\gamma}$ which is only about two per 10^5 K stops. Therefore two important considerations must be established:

(a) The system triggered only on K^+ decays or at least the final selection of $K_{\pi_2\gamma}$ candidates were triggered on K decays only. It is more convincing if all triggers are K decays.

(b) The π^+ identification is certain.

Most of the evidence for (a) and (b) above came from an analysis of the fast display data. The fast display for the 5,584 $K_{\pi_2\gamma}$ triggers was scanned for π-μ decays and at the same time all pulse heights were measured as well as three delays, namely, the Fitch - dE/dx counter delay, the Fitch - 1A or the Fitch - 1B counter delay, and the delay between the stopping π counter pulse and its μ candidate, if any, called the μ delay. The Fitch - dE/dx delay essentially measures the K^+ time of flight between the Fitch and dE/dx counters while the Fitch - 1A or 1B delays essentially measure the time elapsed from the moment the K^+ stopped until it decayed. the μ delay gives the time elasped from the moment the π^+ stopped in the π^+ hodoscope until it decayed. All fast display information for each event was punched into IBM cards for convenience in sorting and classifying events as well as for use with analysis programs requiring certain fast display measurements. Appendix II contains details of the scanning criteria and data processing for the fast display and Appendix III treats in detail the fast display pulse height and sweep calibrations.

The fast display analysis must yield the indentity of the intermediate ranges π's from the K^+ decays. These events will then be the $K_{\pi_2\gamma}$ candidates for further consideration. One would hope that these are all $K_{\pi_2\gamma}$ events, however, as will be shown later, the probability for π^+'s from $K_{\pi 2}$ inelastically scattering in the FC-75 stopper and coming to rest in the hodoscope is large enough to account for most of the observed events.

The spark chamber data must then be relied on for the final selection of $K_{\pi_2\gamma}$ events. In the absence of accidential γ's in the spark chambers, observing three γ's in an event with an intermediate range π^+ would be convincing evidence for $K_{\pi_2\gamma}$. Kinematic fits to the spark chamber measurements and the π^+ energy measurement would provide conclusive evidence for $K_{\pi_2\gamma}$ as well as the best value for the kinematic parameters. Unfortunately, the γ accidential rate proved to be very high, so that kinematic fits are required in order to reject events with accidentals..

In addition to requirements (a) and (b) above it is also necessary:

(c) to show that photons can be reliably identified in the γ chambers and

(d) to show that the spark chamber measurements and the π^+ range measurement are precise enough to allow kinematic fits to reject most non $K_{\pi_2\gamma}$ events.

For a good result, the expected number of non $K_{\pi_2\gamma}$ events which fit must be small compared to the actual number of events fitting the $K_{\pi_2\gamma}$ kinematics.

B. K^+ Identification

Three pieces of evidence from the fast display support the contention that the experimental apparatus triggered only on K^+ decays, namely:

(1) The Fitch - dE/dx counter delay is constant, thus verifying the coincidence of the Fitch and dE/dx pulses with a fixed time of flight.

(2) The dE/dx counter pulse height spectrum agrees with the one expected from stopping K's. Appendix IV shows spectra and gives details.

(3) The strongest evidence appears in the exponential distributions of the delays between the Fitch counter pulse and the pulses from counter 1A or 1B. These distributions show the K^+ lifetime.

The distributions for (3) are shown in Figure 6 and are the results for all 5,584 events considered as a whole. The χ^2 probability for the counter 1A distribution having the K^+ lifetime (12.27 ns) based on the region from 100 to 135 ns is 65% while for counter 1B it is 75% based on the region from 120 to 155 ns. The cut-off seen at the upper end of the distribution is due to 35 ns gate in the triggering logic. The finite rise and fall times on these distributions are caused mainly by differences in magnifications of the projectors used in scanning as well as changes in magnification from one focus-setting to another. The finite bin width of the histogram also makes a contribution to the rise and fall times.

Similar results are obtained for the various sub-classes of events including those events with good π-μ decays. Appendix IV contains plots of these distributions for interesting sub-classes as well as a more detailed discussion of them.

FIGURE 6

K^+ DECAY DELAY SPECTRA

The Fitch counter to counter 1A and the Fitch counter to counter 1B delays are the time elapsed from the moment the K^+ stopped until it decayed plus a fixed delay introduced for convenience in using the display. All 5584 $K_{\pi_2\gamma}$ triggers were used for the histograms plotted on semi-log paper in Figure 6. The dashed line labeled "K^+ lifetime" is the exponential distribution using the known K^+ lifetime (12.27) and normalized to the number of observed events in the region from 100 to 135 ns for counter 1A, and 120 to 155 ns for counter 1B.

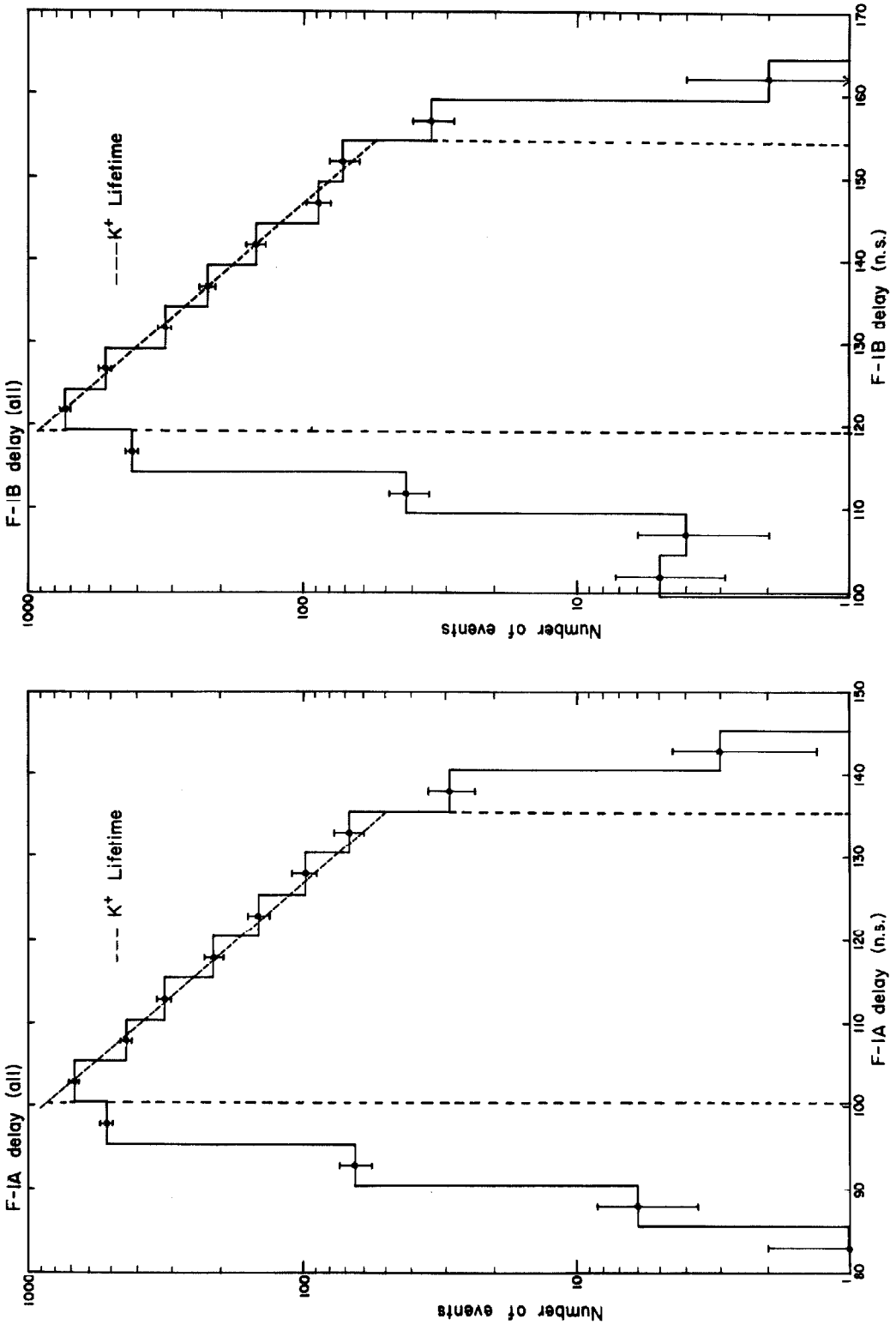
F-1B delay (all)
---K+ Lifetime
Number of events
F-1B delay (n.s.)
F-1A delay (all)
--- K+ Lifetime
Number of events
F-1A delay (n.s.)

Figure 6

C. Pion Identification

The π^+ identification rests mainly with identifying π-μ decays, but additional evidence can be obtained from the π hodoscope counter pulse heights which should behave in a known way for stopping π's. The analysis of τ and τ' events provides a test of the method.

1. Identification of π-μ Decays

Identifying π-μ decays was made difficult by having a small μ pulse height compared to the π pulse height. For the one inch thick hodoscope counters the ratio of the μ pulse height to the π pulse height ranged from 1:1 down to about 1:7 depending on how far the π penetrated into the counter. In terms of scope displacement it is made worse because the system gain is nonlinear in such a way as to make small pulses smaller. Appendix III shows a typical gain curve illustrating typical nonlinearities. The net result is that the average μ pulse height on the fast display is only about two or three times the width of the scope trace. Such small pulses are difficult to separate from reflections, oscillations, and other wiggles on the scope trace.

Because reflections and oscillations are expected to occur for large pulses and at fixed delays, their presence should alter the joint distribution of the μ delay (t) and stopping counter pulse height (h). Since the two variables are independent, this distribution should be the product of an exponential in μ delay and a power law in the stopping counter pulse height. A dot plot of the two

variables in the (t, h) plane is a convenient way to exhibit the distribution of a two dimensional variable because the density of dots is proportional to the distribution function. Figure 7 is a dot plot of the μ delay versus stopping counter pulse height for counter 5B, which was the counter most plagued with reflections. Plots for some other channels are shown in Appendix V. Some channels, such as 5B, show a clustering of points at a fixed delay for large pulse heights; others do not. For each counter an upper limit on the pulse height served to eliminate most of the anomalous regions. The upper limit or bias is established by eye in such a way that below this bias the density of dots behaves as expected for π-μ decays. Table II presents a breakdown of all $K_{\pi 2\gamma}$ triggers by π^+ hodoscope counter and shows the number of events stopping in that counter, the number of π-μ candidates, the number of stopping counter pulses below the pulse height bias described above, and the number of good π-μ candidates, i. e., those not in anomolous regions of dot plots.

It would be desirable to show that the 978 π-μ candidates surviving the above procedure are indeed bonafide π-μ decays. Three pieces of evidence listed below support this conclusion:

(a) The μ delay distributions fit the π lifetime.

(b) Very few π-μ candidates are observed in a scan for π-μ decays in the counters preceding the stopping counter. No π-μ decays should occur in those preceding counters; but contaminations such as oscillations, reflections, and noise pulses should remain.

FIGURE 7

COUNTER 5B DOT PLOT

This figure shows the distributions of two variables measured on the fast display for each π-μ candidate. The ordinate is the μ delay in ns and the abscissa is the stopping π pulse height in counter 5B divided by the pulse height corresponding to minimum. Each dot corresponds to one event. A dashed line labeled "Bias" separates the anomolous region to the right from the region of well behaved events to the left. Due to saturation of the display system, the gain curve for the display reaches a plateau for large pulses; the knee of the gain curve corresponds to the pulse height labeled maximum pulse height in Figure 7. Figure 31 Appendix III shows a sample gain curve.

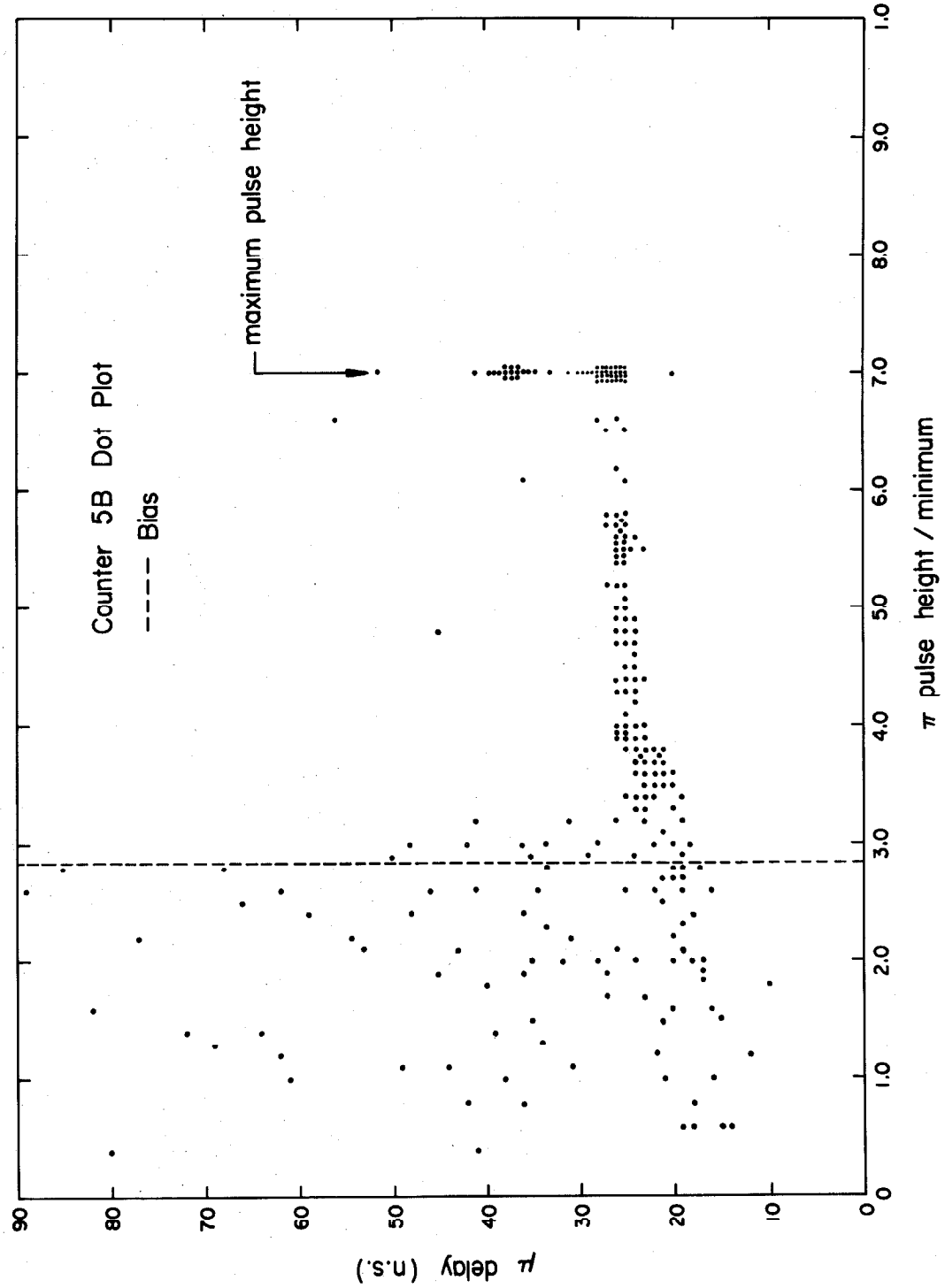
Counter 5B Dot Plot
Bias
maximum pulse height
μ delay (n.s.)
π pulse height / minimum
90
80
70
60
50
40
30
20
10
0
1.0
2.0
3.0
4.0
5.0
6.0
7.0
8.0
9.0
1.0

Figure 7

TABLE II

SUMMARY OF FAST DISPLAY SCAN

For each counter, column A shows the number of events stopping in the counter, column B the number of π-μ candidates observed, column C the number of good π-μ candidates, i.e., those π-μ candidates not in the anomolous regions of the μ delay versus stopping π pulse height dot plots, and column D the number of events whose stopping counter pulse height is below the bias used for separating good π-μ decays. Column E gives the percentage of events, with stopping counter pulse heights below the bias, which have good π-μ decays.

The row labeled amb. refers to those events which had both A and B counter pulses for at least one channel. Such events were separated and not considered in the rest of the analysis.

TABLE II

SUMMARY OF FAST DISPLAY SCAN

	A	B	C	D	E
Counter	Stops	π-μ Cand.	Good π-μ Candidates	Stops below bias	C/D (%)
1A	599	398	207	285	75
2A	184	98	58	111	53
3A	161	65	42	103	46
4A	276	73	57	182	34
5A	523	235	92	243	40
6A	965	243	103	559	18
1B	651	419	177	219	83
2B	124	60	56	120	47
3B	458	134	--	--	--
5B	606	363	83	238	35
6B	991	188	103	611	17
amb.	146	31	--	--	--
Totals	5584	2307	978	2671	--

(c) Good fits to the pulse height information for most events are obtained by assuming that the pulse heights arise from stopping π^+ while very poor fits are obtained for the stopping proton hypothesis.

Ideally it is desirable to test each stopping counter separately, but such a breakdown sufficiently reduces the number of events in some counters to the point of poor statistics. What was done, however, was to group certain counters together. Counters 1A and 1B were grouped together as Group I because these counters would detect π's from τ and τ' decays; these counters also had the highest number of events. Channels 2 through 5, forming Group II, should be relatively free from τ and τ' events as well as from $K_{\pi 2}$ events, although channel 2 can still see some τ and τ' events, particularly τ' events, and the higher channels can detect π's from $K_{\pi 2}$ if the π^+ suffers appreciable inelastic scatterings. Counters 6A and 6B were considered together as Group III because they were susceptible to $K_{\pi 2}$ decays where the π^+ came from deep in the stopper and/or scattered enough in the wedge or hodoscope for the oblique angle to give it enough range to stop in the hodoscope. These counters had the second highest number of events. Channels 2 through 5 did indeed have significantly fewer events and so the remaining effort to find $K_{\pi_2\gamma}$ events that are the least troubled with backgrounds was concentrated here.

Each of the three groups satisfactorily passed the K^+ identification tests described earlier, the details of which are presented in Appendix IV. The μ delay distribution for the 388 events of Group II as well as the distribution for the 174 events of Group II having a good π chamber track are shown in Figures 8 and 9. The good π chamber track requirement will be discussed later. The χ^2 probability for the samples to have the π lifetime of 25.6 ns, based on events in the delay region 15 to 75 ns, is 42% for all 388 events and 59% for the 174 events. Below 15 ns delay the efficiency for seeing the μ drops rapidly as the μ pulses merge with the π pulse and cannot be distinguished. Appendix V shows plots and χ^2's for the other two groups having good π-μ decays.

Table III columns A, B, and C show the results from a scan of counters behind the stopping counter where no π-μ decays should be seen, while column D shows the number of good π-μ decays which would have occurred if the same number of stopping counters had been scanned instead. Only 16 good π-μ decays were observed in the background scan, whereas 70 times as many would have been identified in a scan of the same number of stopping counter pulses. These results indicate that the procedure for separating contamination from the π-μ candidates is quite clean.

2. A π Chamber Consideration

Of the 388 events in channels 2 through 5 with good π-μ decays, 214 were eliminated because the π chamber either had no

FIGURES 8 and 9

MU DELAY HISTOGRAMS

Figures 8 and 9 are μ delay histograms plotted on semi-log paper with the μ delay along the abscissa and the number of events per 5 ns bin as the ordinate. Figure 8 shows the plot for all 388 events of Group II and Figure 9 the plot for the 174 events of Group II having a good π chamber track. The dotted curve is the expected histogram using the exponential distribution with the known π lifetime (25.6 ns) and normalized to the observed number of events in the region of 15 to 75 ns. $P(\chi^2)$ is the χ^2 probability that the data fit the π^+ lifetime.

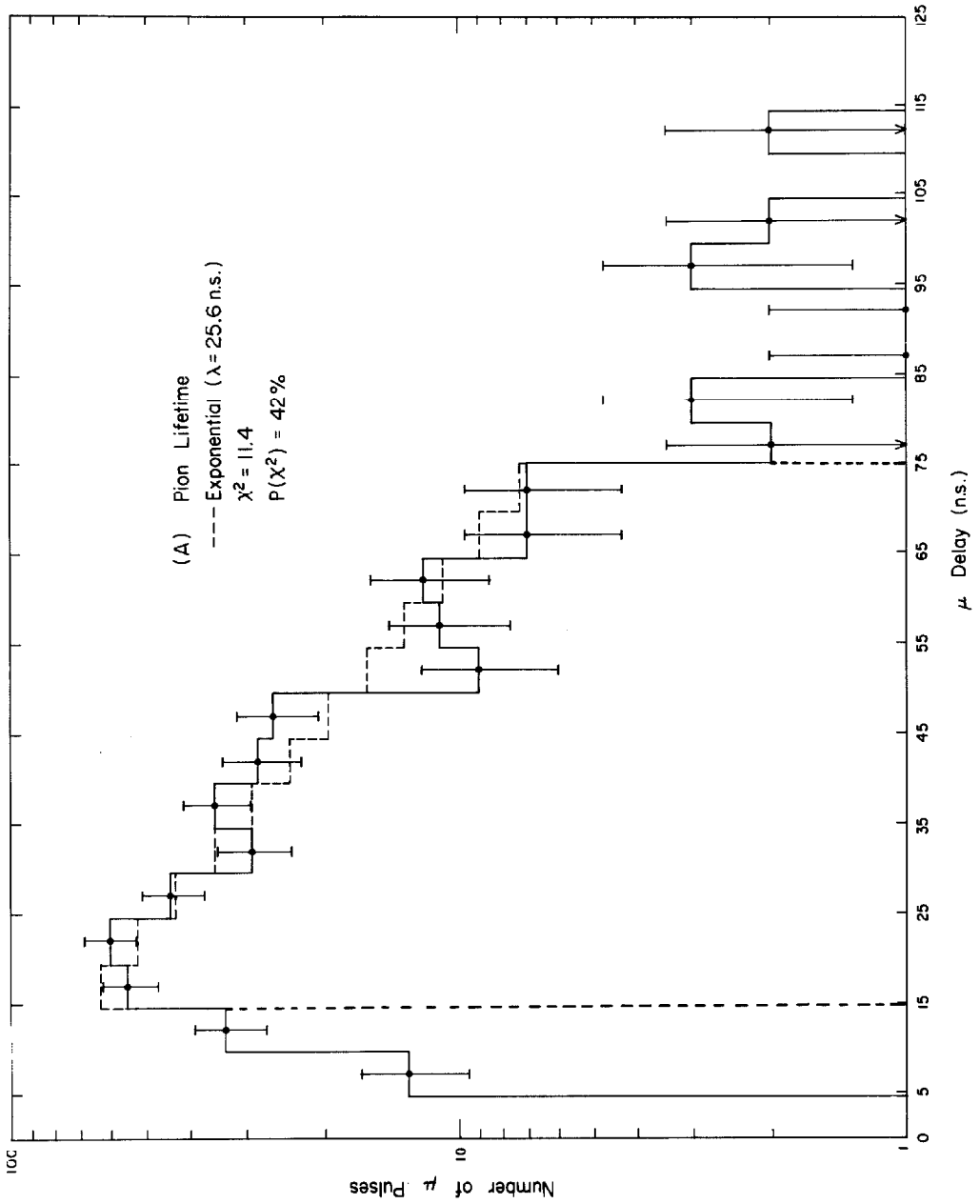
(A) Pion Lifetime
--- Exponential (λ = 25.6 n.s.)
χ² = 11.4
P(χ²) = 42%
Number of μ Pulses
μ Delay (n.s.)
0
5
15
25
35
45
55
65
75
85
95
105
115
125
1
10
100

Figure 3

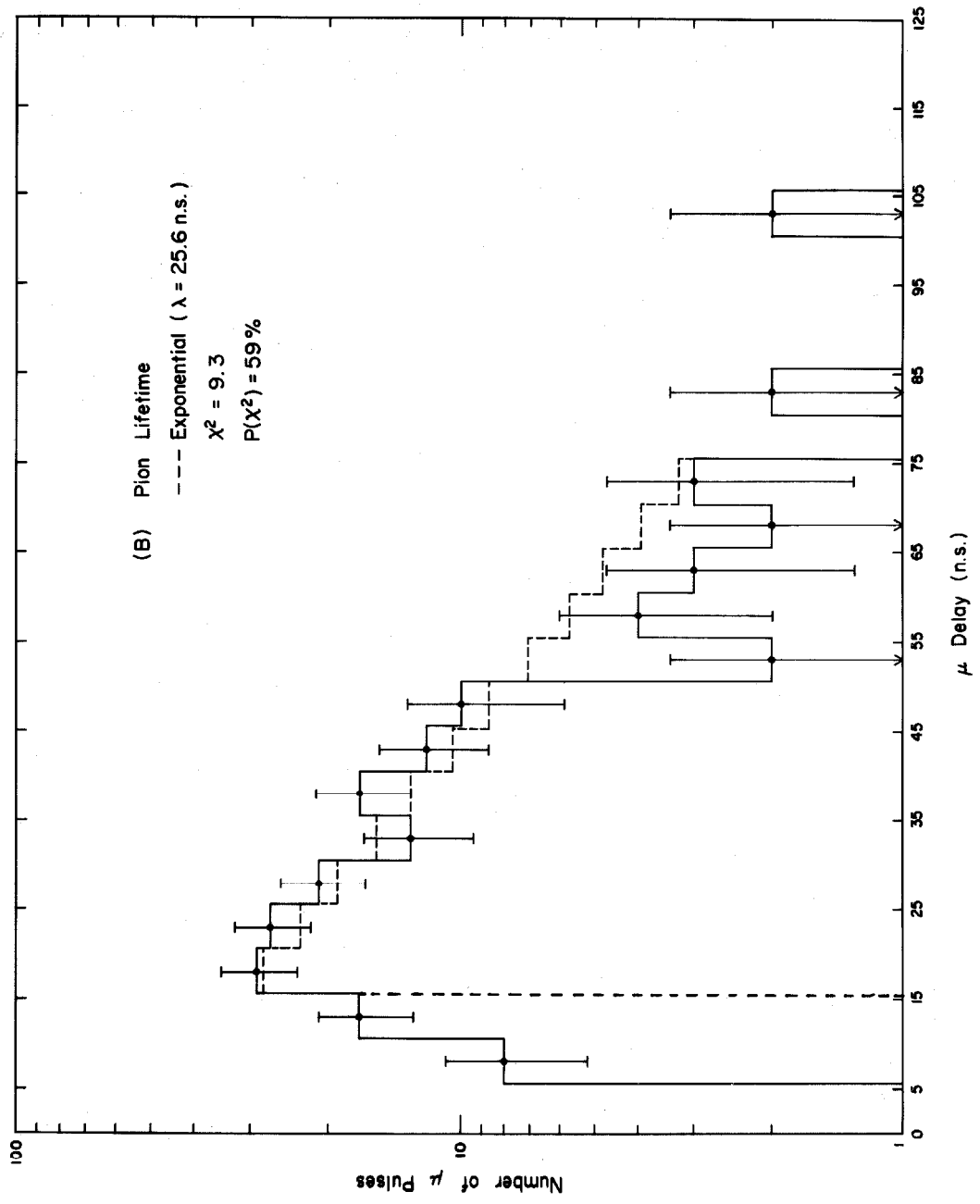
(B) Pion Lifetime
--- Exponential (λ = 25.6 n.s.)
χ² = 9.3
P(χ²) = 59%
Number of μ Pulses
μ Delay (n.s.)
100
10
1
0
5
15
25
35
45
55
65
75
85
95
105
115
125

Figure 9

TABLE III

π-μ BACKGROUND SCAN

	A	B	C	D
Counter	Pulses Scanned	Pulses Below Bias	Good π-μ	"Expected" π-μ
1A	252	224	2	168
2A	238	226	1	120
3A	252	250	5	115
4A	282	260	1	89
5A	396	342	3	137
6A	148	140	1	28
1B	191	173	1	144
2B	287	286	0	130
3B	282	--	-	--
5B	445	386	2	135
6B	130	129	0	22
Totals	2903	2416	16	1088

track, or two tracks, or a track indicating that the π went through part of the sides of the π chamber before emerging in the spark gaps. About 85% of those eliminated had no π chamber tracks. It is possible for particles coming from the stopper to follow straight trajectories to the hodoscope and miss the π chamber's sensitive regions by going through the lucite sides of the chamber or even through edges of the γ chambers. In this way π^+'s from $K_{\pi 2}$ decays can stop in the hodoscope without inelastic scattering; also π's may scatter into the hodoscope from the γ chambers and the π chamber edges and still miss the π chamber. A study of the fraction of events from each counter that have good π chamber tracks provides evidence to support this conjecture. The data for each counter are shown in Table IV. Channel 1, which is susceptible to π's from τ and τ' decays, has a high percentage of good π chamber tracks. As one goes to the higher counters the percentage gets lower until channel 5 has only 33% with good π tracks. Channel 2 and even 3 can see some of the τ and τ' events if the K stops high enough in the stopper. The percentage is slightly higher again for Channel 6, which is sensitive to π's from $K_{\pi 2}$ that come from deep in the stopper and which from straggling, from elastic scattering off hydrogen in the hodoscope or wedge, or from the increased range of an oblique trajectory manage to lose the extra few MeV needed in order to stop in the hodoscope.

TABLE IV

RESULTS OF π CHAMBER REQUIREMENT

	A	B	C
Channel	Good π-μ	π Chamber Good	% Good π Chamber
1	384	316	82 ± 5
2	114	68	60 ± 7
3	42	19	45 ± 11
4	57	29	51 ± 10
5	176	58	33 ± 4
6	206	83	41 ± 4
Total	979	573	--

Column A shows for each channel the number of events having a good π-μ decay, while column B presents the number that in addition have a "good" π chamber track as discussed in the main text. Column C expresses B as a percentage of A. The errors presented in column C are based on the statistical uncertainties for the number of events in column B.

3. Pulse Height Fitting

The pulse height from a scintillation counter is proportional to the light output, $\int(dL/dx)dx$, from the scintillator, which in turn is a function of the mass and residual range of the particle. Assuming that the mass is known, the only free parameter is the range in the stopping counter; therefore, by using a minimum χ^2 technique, a one parameter fit to the pulse height information can be obtained. A sample of the results can be seen in the χ^2 histograms for fits to good π-μ events stopping in counter 5A. Figure 10A shows the histogram for a stopping π hypothesis while Figure 10B shows the histogram for a stopping proton hypothesis. For comparison the expected χ^2 distribution for four degrees of freedom, normalized to the number of events with $\chi^2 < 13$ is shown on the first graph, while on the second graph the χ^2 distribution normalized to 10 events is shown. These plots show that about 15% of the events give poor π fits and only one event gives anywhere close to a decent proton fit. Thus, it can be concluded that the majority of events with good π-μ decays are normal stopping π's. The poor fits can be understood as scattering in the hodoscope or as occasional large Landau fluctuations. Figures 11 and 12 are χ^2 histograms for fits to good π-μ events stopping in counters other than 5A. Tables V and VI summarize the results of pulse height fitting for the various channels.

The main features of Figures 11 and 12 and Table V show that results similar to those seen in 5A hold for the other counters of channels 2 through 5. These results carry over to the

FIGURES 10, 11, 12

HISTOGRAMS FOR PULSE HEIGHT FITTING

The results of pulse height fitting, also called dL/dx fitting, are presented here as histograms of the value of χ^2 obtained for events stopping in the various counters and having a good π-μ decay. The expected chi squared histograms for the appropriate number of degrees of freedom (d. f.) normalized to the number of events having observed χ^2 less than the cutoff for each channel are plotted with dashed lines. Figures 11 and 12 show fits to counters 2A, 2B, 3A, 4A, 5B, 6A, and 6B assuming the events to be normal stopping pions. Figure 10 shows results for counter 5A, both for the stopping π hypothesis (10A) and the stopping proton hypothesis (10B). Here, for the proton fits, the expected distribution is normalized to 10 events instead of the number below the χ^2 cutoff. The χ^2 cutoffs used for each counter are listed in Table V.

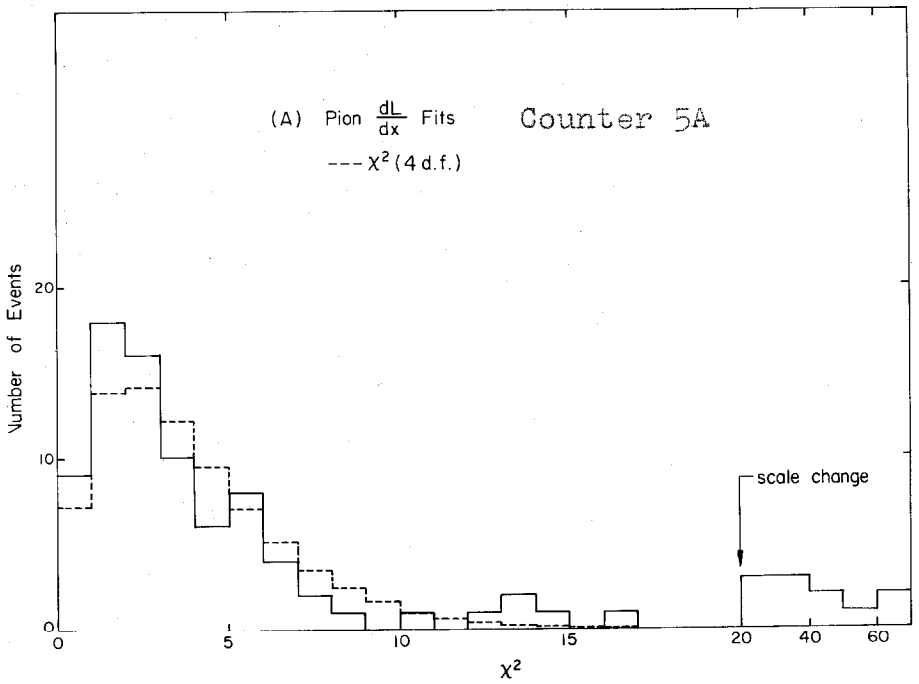
(A) Pion dL/dx Fits
Counter 5A
---χ²(4 d.f.)
Number of Events
20
10
0
0
5
10
15
20
40
60
scale change
χ²

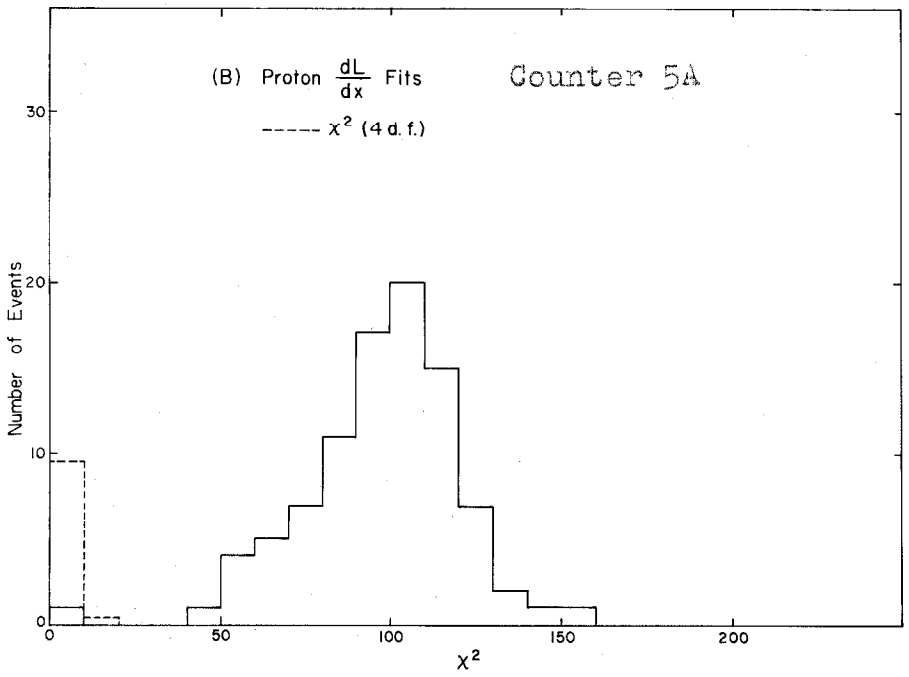
(B) Proton dL/dx Fits
Counter 5A
----- χ² (4 d. f.)
Number of Events
30
20
10
0
0
50
100
150
200
χ²

Figure 10

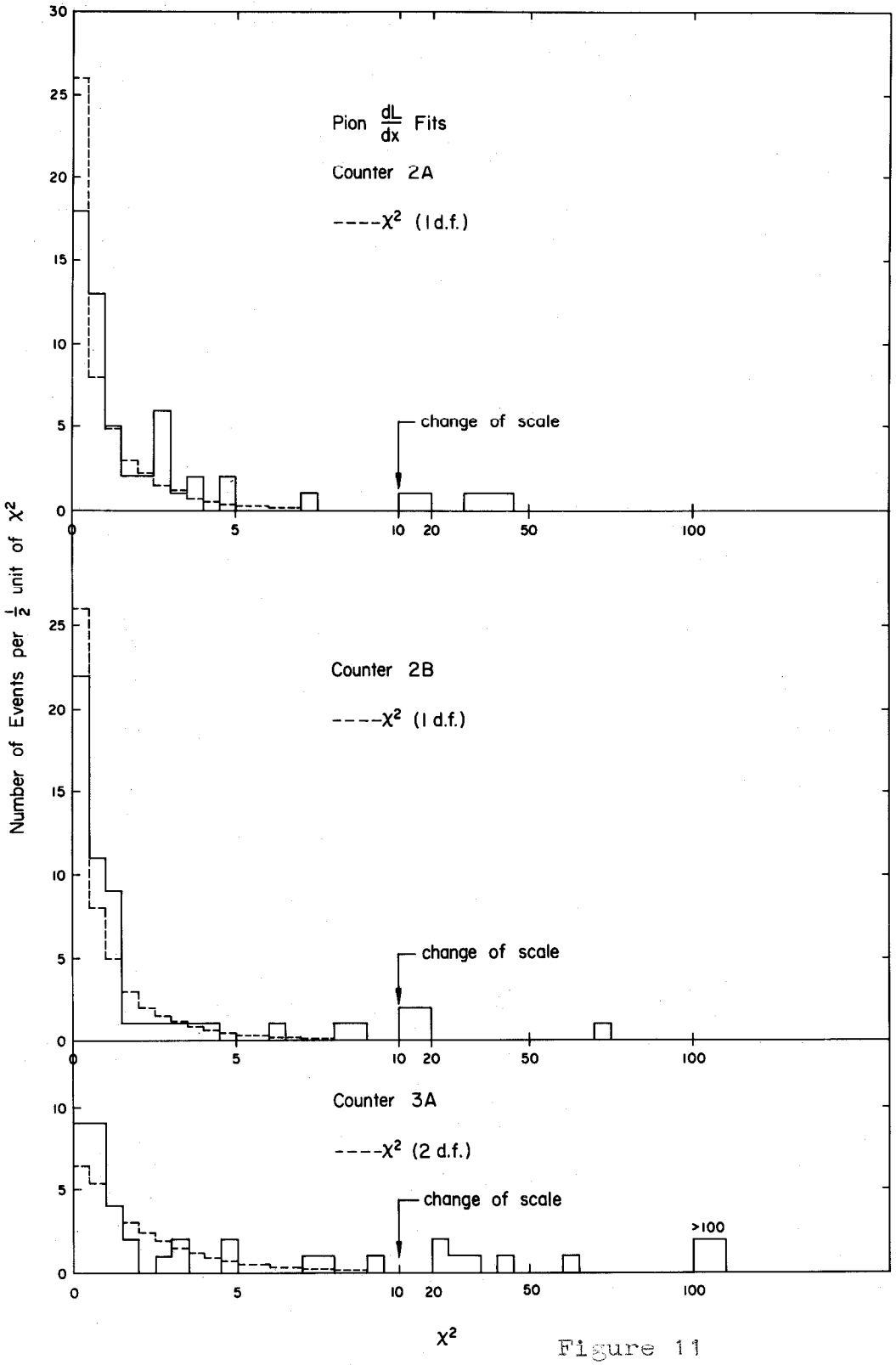
Pion dL/dx Fits
Counter 2A
----X² (1 d.f.)
change of scale
Counter 2B
----X² (1 d.f.)
change of scale
Counter 3A
----X² (2 d.f.)
change of scale
>100
Number of Events per ½ unit of X²
X²
0
5
10
20
50
100

Figure 11

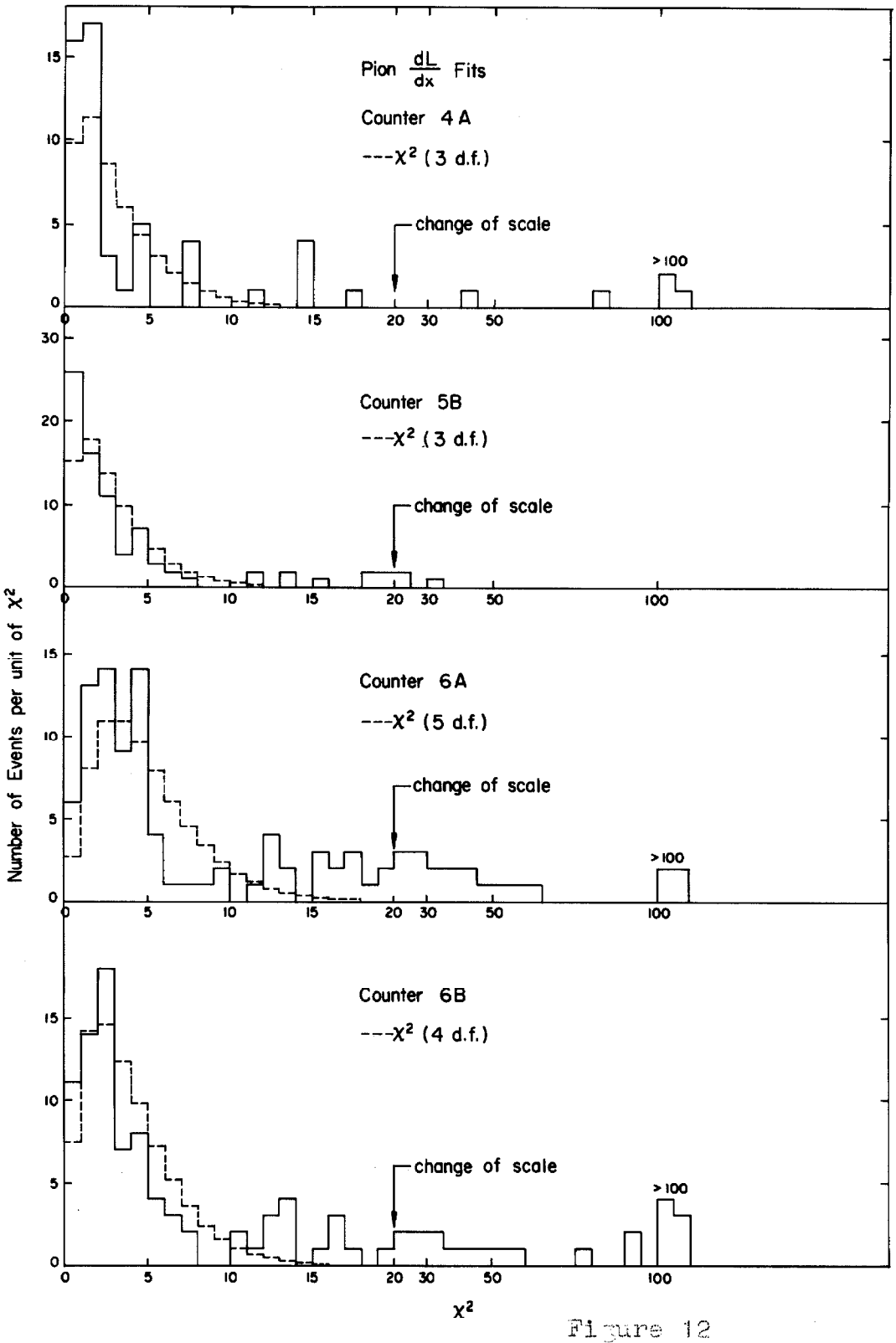
Pion dL/dx Fits
Counter 4A
---χ² (3 d.f.)
change of scale
>100
Counter 5B
---χ² (3 d.f.)
change of scale
Counter 6A
---χ² (5 d.f.)
change of scale
>100
Counter 6B
---χ² (4 d.f.)
change of scale
>100
Number of Events per unit of χ²
χ²

Figure 12

TABLE V

PULSE HEIGHT FITS

Pulse height fitting results for all events having a good π-μ decay are presented in this table. Counter 1A and 1B would give zero constraint fits and so are not included. Column A gives the χ^2 cutoff used to determine a "good fit". The χ^2 cutoff was at the 1% level. If the χ^2 was less than the cutoff, the event was considered a "good fit". Columns B, C, and D concern all the events with a good π-μ decay; column B shows the total number stopping in each counter; column C gives the number that fit the stopping π hypothesis, while column D shows the number that fit the stopping proton hypothesis.

In columns E, F, and G only the events in channels 2 through 5 having a good π chamber as well as a good π-μ decay are considered. These 174 $K_{\pi_2\gamma}$ candidates had a stopping counter distribution as shown in column E. Columns F and G show the number that fit the stopping π or stopping proton hypothesis respectively. The percentage figures shown at the bottom reflect the fraction of each category that fit the stopping π or proton hypothesis respectively.

TABLE V

PULSE HEIGHT FITS

	All Good π-μ Events				Good π Chamber Track		
	A	B	C	D	E	F	G
Counter	χ^2 Cutoff	Total Events	Fit Pion	Fit Proton	Total Events	Fit Pion	Fit Proton
2A	6.5	58	52	0	36	32	0
3A	9.3	42	32	2	19	13	2
4A	11.2	57	47	2	29	24	2
5A	13.3	92	79	1	31	25	1
6A	15.0	103	72	0	--	--	-
2B	6.5	56	49	1	32	27	0
3B	9.3	0	--	-	--	--	-
5B	11.2	83	71	0	27	25	0
6B	13.3	103	76	2	--	--	-
Totals	--	594	478	8	174	146	5
	% of 594		80%	1.4%	% of 174	84%	3%
	% of 388		85%*	1.5%*			

*excluding channel 6

TABLE VI

OTHER PULSE HEIGHT FITTING RESULTS

The same χ^2 cutoffs were used here as in Table V to ascertain which events gave good fits to the hypothesis under consideration. Two categories of events are considered: those with no π-μ candidates and those with π-μ candidates which are not good. Column A and D give the counter distributions for each category respectively. Columns B and E show the number that fit the stopping π hypothesis and columns C and F the number that fit the stopping proton hypothesis for each category. Once again the percentages that fit the two different hypotheses for each category are shown at the bottom of the table.

TABLE VI

OTHER PULSE HEIGHT FITTING RESULTS

	No. π-μ Candidates			π-μ Candidates are not good		
	A	B	C	D	E	F
Counter	Total Events	Fit Pion	Fit Proton	Total Events	Fit Pion	Fit Proton
2A	86	36	27	40	15	15
3A	96	21	36	23	5	18
4A	203	71	40	16	15	2
5A	288	118	41	143	15	11
6A	722	286	14	140	70	0
2B	64	43	15	4	4	0
3B	344	80	0	134	39	0
5B	243	168	19	280	171	63
6B	803	491	21	85	53	2
Total	2849	1314	213	865	386	111
	% of 2849	46.1%	7.5%	% of 865	44.6%	12.8%
	% of 1324	40.6%*	13.5%*	% of 640	41.0%*	17.1%*

*excluding channel 6

particular sub-class of those with good π chamber tracks. For channel 6 there are a significantly greater number of events that do not fit the stopping π hypothesis, but the χ^2's are not enormously large, indicating that the deviation was not extreme. This is not surprising for channel 6, since a π from $K_{\pi 2}$ needs only a fairly mild inelastic occurrence to cause it to stop here.

In Table VI are presented the pulse height fitting results for all events other than those with good π-μ decays. What is noticeable is that a much larger fraction, 50% to 60% as compared with 15% in Table V, are not stopping π's; thereby, indicating that the π-μ scheme provided some discrimination against undesirable events. Another interesting feature is the total number of good π fits in each channel, for channels 2A through 5A and 2B show approximately the same numbers here as they did for the good π-μ decays. The position of the μ delay cutoff indicates that about 50% of the stopping π's should have detectable μ's; the other 50% would show up in the Table VI events if the μ gate (see the triggering scheme in Appendix I) was moved too close to the π pulse, thus letting through stopping π's with prompt decays. The large number of fits seen for chambers 6A and 6B can also be explained. Pions from $K_{\pi 2}$ will stop just beyond channel 6; if they stop within a gram or so of it, and a large number will, they can still give a χ^2 of 10 to 15. The broad χ^2 distribution for channel 6 supports this explanation. The large number of events in channel 5B that fit is perhaps also understood when it is considered that some of the most

important pulse height information is lost because the precessor below counter 5B takes away the equivalent of one and three quarter counters. Much of the sensitivity of the fit is contained in the pulses just behind the stopping counter, for it is here that rapid changes in energy loss are taking place. If an inelastic scatter takes place in the precessor and the π stops in 5B, the event could fit, whereas it might not if counters were in the precessor's place.

The use of pulse height fits as evidence for π^+ identification is less certain than observing π-μ decays. First, a stopping π may not necessarily behave like the average; it may inelastically scatter and give a poor fit, but still stop and give a π-μ decay; or it may elastically scatter and go through at such a large angle that the large pulses which result will not fit. Secondly, a fast proton or kaon going out the side of the hodoscope could fit. Thirdly, μ's are close enough in mass to π's so that stopping μ's will fit the stopping π hypothesis. However, a reasonable fit to the π hypothesis and a bad fit to the stopping proton hypothesis is a necessary condition for a non-interacting, stopping π^+.

A final test of the π^+ identification procedure would be to try it on something that is known to produce π^+. Channel 1 is sensitive to π^+ from τ and τ' decays. It is possible to compute the number that should be identified given the π^+ energy spectrum for τ and τ' and the branching ratios as well as the y coordinate distribution of the K^+, the solid angle of counter 1A and 1B, and the π-μ detection efficiency. The calculation, when normalized to the number of K^+

counted, predicts 330 events, while 316 π-μ decays were actually observed in channel 1. Later, after the γ chamber data has been analyzed, spark chamber evidence will be presented to support the contention that the 316 events are τ and τ'. For channel 6 it is difficult to compute the number of π-μ decays expected to be seen, but the γ chamber results for the fast, monoenergetic π^o from $K_{\pi 2}$ would be qualitatively different from the slow π^o's from the three body τ' decay. These results will also be considered later.

4. The $K_{\pi_2\gamma}$ Candidates

The 174 events with good π-μ decays in channels 2 through 5 and with good π chamber tracks satisfactorily passed previously described tests for triggering on K^+ decays and for good π^+ identification. Good χ^2 probabilities of 68% and 90% for the K^+ and 59% for the π^+ lifetime distribuions were obtained. This sample of intermediate range π's from K^1 decays can give an upper limit on the $K_{\pi_2\gamma}$ branching ratio; however, the contamination from inelastic scattering in the stopper of π^+'s from $K_{\pi 2}$ and undetected inelastic scattering in the wedge and hodoscope can be large. A Monte Carlo calculation of inelastic scattering in the stopper is described in Appendix VII and predicts that most, approximately 120, of the 174 are due to this cause alone. The calculation is not particularly precise as it is based upon limited data, but should be good to within a factor of 2. Additional events can come from back-scattering in the material of the γ chambers, especially in Chamber 3. Inelastic scattering in the wedge and hodoscope would add more.

It is possible to eliminate some inelastic scatterings in the hodoscope because the pulse height information would be affected. Inelastic scattering is often accompanied by emission of charged particles which could cause a large pulse in the counter where scattering occurred and consequently give poor fits to pulse height information. Abrupt changes in energy or large changes in direction, arising from interactions which give rise to oblique angles, also cause abrupt changes in dL/dx and give rise to poor fits. Indeed, about 15% of channels 2 through 5 events do give poor pulse height fits to ordinary stopping π hypotheses, but do not fit stopping proton hypothesis, thus suggesting that they are interactions.

One other piece of fast display information that might be useful in rejecting interactions in the FC-75 pulse. This counter is known, from a study of $K_{\pi 2}$ events in calibration runs, to give visible pulses for 60% of the π's from $K_{\pi 2}$. If a π^+ from $K_{\pi 2}$ goes far enough in the stopper before interacting it may have a reasonable chance for producing an FC-75 pulse that can be seen on the fast display. Inelastic scattering produces mainly longer range π's which stop in channels 4 and beyond. Some of the 174 events do have FC-75 pulses and, significantly, they are mostly in channels 4 and 5 as can be seen in the Table below.

THE 174 $K_{\pi_2\gamma}$ CANDIDATES

Channel	No. with FC-75	Total for Channel
2	1	68
3	0	19
4	6	29
5	20	58
Total	27	174

The problem with using these events as an estimate of the number of interactions is that the efficiency for seeing them is unknown. The FC-75 counter's efficiency depends on how far the π went before interaction, on the angle with respect to the phototube, and on the energy loss in the interaction. The threshold for π's is around 85 MeV and the number of photons produced depends strongly on how far the π is above threshold. So even some good events might fire the FC-75 counter, but with small efficiency; however, one can use the FC-75 results as a lower limit on interactions by assuming the same efficiency as obtained for calibration runs. This procedure yields about 50 interactions, a number which is in agreement with the 120 predicted by the Monte Carlo calculation considering that accuracy of calculation is not good and that the 50 events are a lower limit.

An upper limit on the $K_{\pi_2\gamma}$ branching ratio can be established using the 174 events with intermediate range π's as data

and subtracting the lower limit of 50 events for contamination from $K_{\pi 2}$. The result is 1.8×10^{-3} for an upper limit on the $K_{\pi_2\gamma}$ branching ratio. On the other hand, using the 120 events computed for the $K_{\pi 2}$ contamination yields a result of $\sim (0.8 \pm 0.8) \times 10^{-3}$ for the branching ratio. Any improvement in the quality of this result for this experiment rests with the spark chamber data.

D. Photon Spark Chamber Data Analysis

1. Introduction

One purpose of the γ spark chambers was to detect photons by observing in spark chambers the shower produced when photons convert in matter. The other purpose was to determine the location of the point of conversion of the photons. Observing three γ's associated with an intermediate range π^+ from a K^+ decay is convincing evidence for a $K_{\pi_2\gamma}$ event providing there is no possibility for accidental γ's appearing. In order to specify the kinematic parameters describing the $K_{\pi_2\gamma}$ events and to aid in eliminating contaminations, the capability for making sufficient measurements to overdetermine the kinematics was built into the design of the experiment.

The present section will be devoted to describing the procedure for identifying photon showers, the evidence proving a proper γ identification, a study of backgrounds due to accidental γ's and charged particles, and spark chamber data for the 174 $K_{\pi_2\gamma}$ candidates as well as for the events with π's stopping in

channel 1 or 6. The analysis based on kinematic fits to spark chamber measurement will be described in the following section, Section E.

The first two plates of each γ chamber were constructed of aluminum so that photons would have a small probability of about 0.05 for converting in them. Thus, a photon would be identified as a track starting after the first two gaps while a charged particle track would start in the first gap. The gap efficiency for a spark chamber is the probability that a gap will have a spark in it near the particle trajectory. Experimentally, it is measured as the ratio of missing gaps to total gaps along a particle trajectory. For the γ chambers, the probability that the first gaps are absent is non-negligible for an old, inefficient charged particle track when the inefficiency approaches 30%. These tracks have a further characteristic of γ showers in that they skip gaps further down the track, just as many photon showers do.

During the experiment the sweep field voltage of the γ chambers was adjusted to give a sensitive time of 5 microseconds. At such long sensitive times the gap-efficiency cut-off is not sharp and varies with impurities in the gas mixture. At the end of the experiment the gap efficiency as a function of the delay in the trigger was measured out to 5 μseconds for cosmic rays. The three curves - f, g and h - shown in Figure 13B are for 0, 3.0, and 5.0 volts respectively. For comparison the curves a, b, c, d and e are also shown in Figure 13A for a retangular chamber with 11

FIGURE 13

GAP EFFICIENCY VERSUS DELAY

Figure 13a shows the gap efficiency, η, as a function of the external delay of the spark chamber trigger for several settings of the sweep field voltage for a prototype rectangular chamber having eleven 1/8-inch steel plates with 1/4-inch gaps. Curves a, b, c, d, and e correspond to 0, 20, 40, 60, and 80 volts respectively. In Figure 13b curves are shown for the γ chambers used in this experiment; curves f, g, and h correspond to 0.0, 3.0, and 5.0 volts respectively.

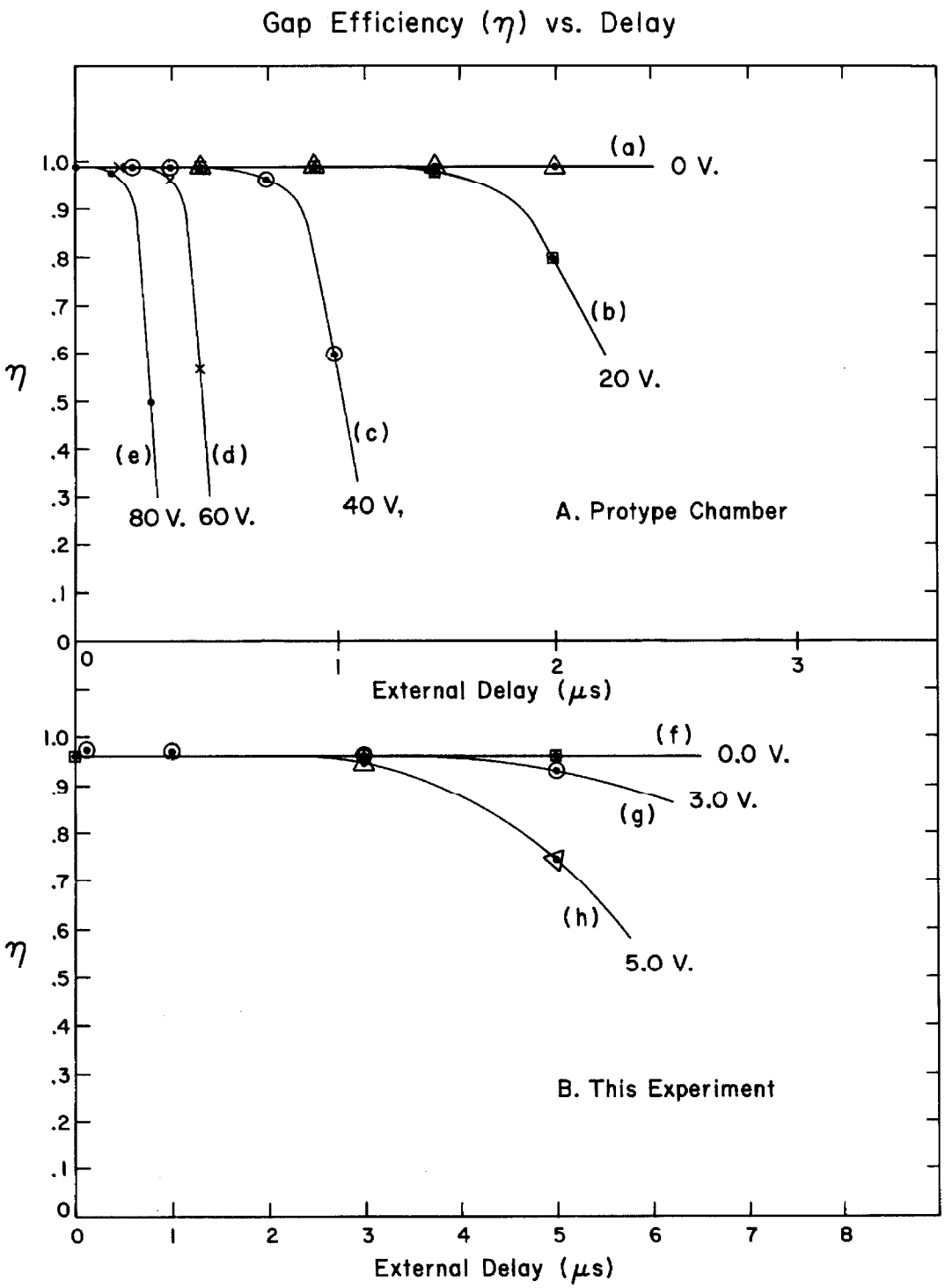
Gap Efficiency (η) vs. Delay
η
1.0
.9
.8
.7
.6
.5
.4
.3
.2
.1
0
(a)
0 V.
(b)
20 V.
(c)
40 V,
(d)
60 V.
(e)
80 V.
A. Protype Chamber
0
1
2
3
External Delay (μs)
(f)
0.0 V.
(g)
3.0 V.
(h)
5.0 V.
B. This Experiment
4
5
6
7
8
External Delay (μs)

Figure 13

steel plates with 1/4-inch gaps and were run for 0, 20, 40, 60, and 80 volts respectively. During the experiment the γ chambers were run at 3.0 volts. The efficiency was still 93% at this point, although increasing the sweep voltage by 70% reduced the efficiency to 75% at 5 μsec. This means that the γ chambers were probably sensitive for about 10 μsec.

The long sensitive time leads to the appearance of γ like tracks not associated with triggered events for two reasons:

(a) The chance for real accidental γ showers not associated with trigger, but from sources like charge exchange scattering of the many π^+ in the K beam, increases with the sensitive time.

(b) The occurrence of old tracks with low gap efficiency increases because the fall time of the efficiency versus delay curve increases with increasing sensitive time. The old charged particle tracks can look like photon showers.

Before the spark chamber information can be convincing, it is necessary to know:

(c) which tracks are photon showers, and

(d) the chance for and spatial distributions of accidental photon showers.

2. Photon Identification

The chief problem in identifying photons is determining how short and inefficient a track can be and still be associated with a photon conversion and not be part of an old, inefficient track or just plain random junk. Requiring at least three consecutive sparks in the track and requiring that it point, in general, towards the stopper gave a good criterion. The test of a good criterion is that the photons so identified by it must exhibit an exponential conversion point distribution with the proper conversion length. The total collection of γ tracks as well as various sub-classes give good χ^2 probabilities for fitting an exponential conversion point distribution when a value of the conversion length obtained from γ absorption experiments was used (29). Figure 14 shows the conversion point distribution for the collection of all photons made up of the 174 $K_{\pi 2\gamma}$ candidates, short range calibration events, and backgrounds to $K_{\mu 2}$ events, all of which will be discussed shortly. The gap number refers to the gap in which the first spark of the shower is observed. The histogram bin width is four gaps. The total collection has a χ^2 probability of 26 % for fitting an exponential distribution over the entire chamber when the expected value of 9.5 plates is used. The expected value has been averaged over polar angles accessible in the spark chambers.

During the course of the experiment, a number of calibration runs were made, which were triggered on $K_{\mu 2}$ and $K_{\pi 2}$ decays. The $K_{\mu 2}$ events would provide information about accidentals,

FIGURE 14

PHOTON CONVERSION POINT DISTRIBUTION

Figure 14 is a histogram of the gap in which photons first appear. The gaps are numbered from 1 to 36 starting with 1 as the gap nearest the stopper. Four gaps are combined for each bin of the histogram. All photons from the 174 $K_{\pi_2\gamma}$ candidates (150 γ's), the Type L (71 γ's) and Type S (198 γ's) calibration events and backgrounds to $K_{\mu 2}$ events (265 γ's) giving a total of 684 γ's were used in this plot. The dashed line is the histogram expected on the basis of an exponential distribution with $\lambda = 9.5$ plates and normalized to 684 γ's. The error flags are statistical errors. $P_7(\chi^2)$ is the χ^2 probability that the observed distribution fit an exponential using $\lambda = 9.5$ plates.

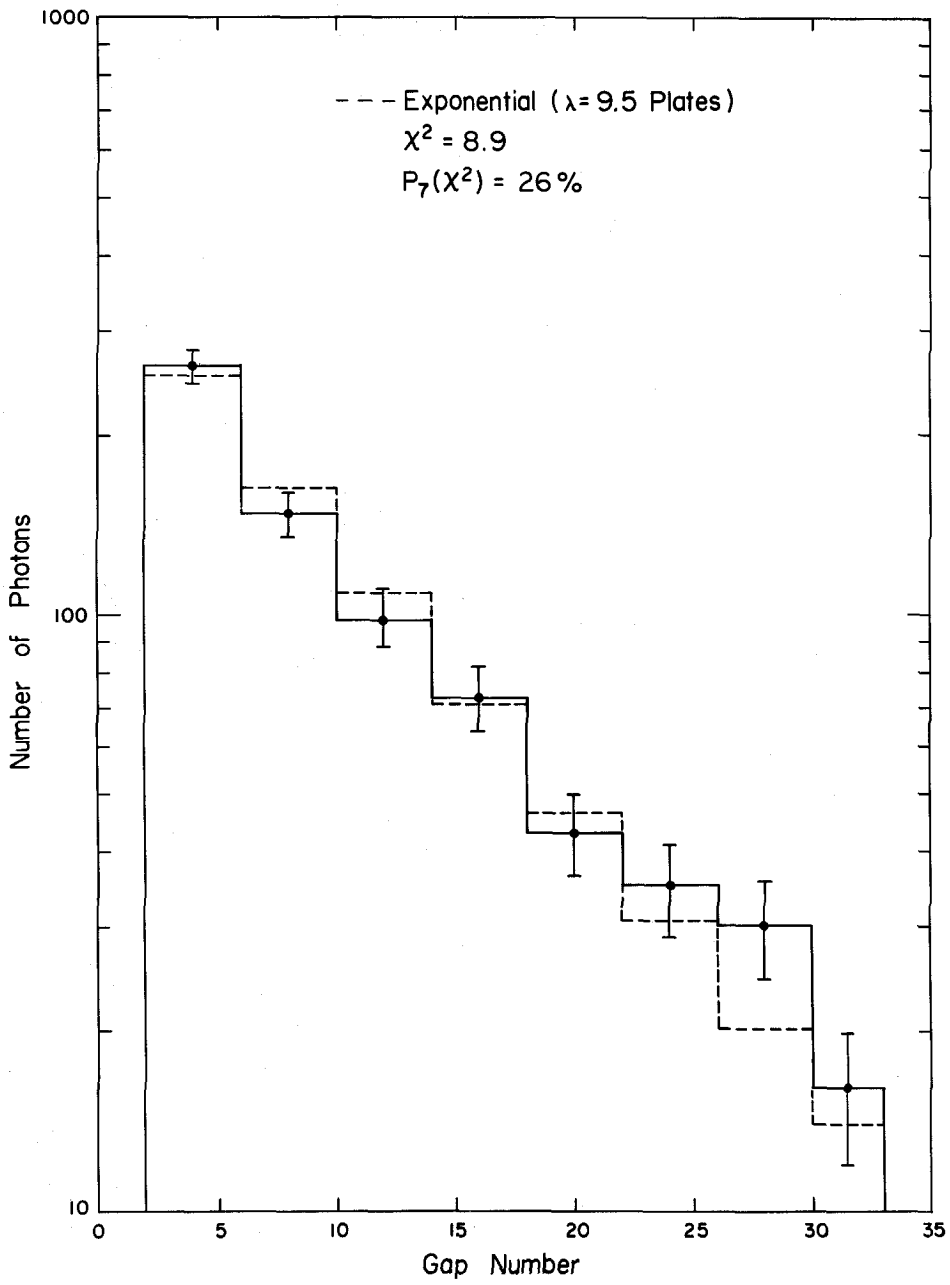
1000
100
10
Number of Photons
0
5
10
15
20
25
30
35
Gap Number
- - - Exponential (λ= 9.5 Plates)
X^2 = 8.9
$P_7(X^2)$ = 26 %

Figure 14

while the $K_{\pi 2}$ events are a predictable source of photons. Two types of events were separated; those with short range particles, called Type S, that went through channel 6 of the hodoscope, but not into channels 7, 8, 9, or 10 of the $K_{\mu 3}$ experiment, and those with long range particles, called Type L, that gave pulses past channel 6. Type S events are a mixture of $K_{\pi 2}$ events and $K_{\mu 2}$ events where the μ went at such an angle as to miss channels 7 through 10, while type L events are nearly pure $K_{\mu 2}$ events.

The conversion point distributions for the 174 $K_{\pi_2 \gamma}$ candidates and for the Type S or short range calibration events are shown in Figure 15. The χ^2 probabilities assuming $\lambda = 9.5$ plates are 98% and 63% respectively. Figure 16 shows the conversion point distribution for the 71 photons from Type L events of the calibration runs combined with 265 photons from another series of runs set to trigger only on Type L events.

The above data shows that the γ criteria identified photons with relatively little contamination from other sources. Further analysis is necessary to establish the efficiency for identifying photons. The best evidence for both proper identification and for a nearly 100% efficiency will be discussed in the section on kinematic fitting where it will be shown that the proper number, i.e., thirty-six, of two γ events from the Type S events fit the $K_{\pi 2}$ kinematics and exhibit the proper opening angle distribution for the π^0 decay. The statistics on thirty-six events limit the search for anomolies in the behavior of $K_{\pi 2}$ events as seen in the spark chambers. More evidence is available utilizing the three times more numerous one

FIGURES 15 AND 16

PHOTON CONVERSION POINT DISTRIBUTIONS

These two figures break down data of Figure 14 into histograms for the various classes of events combined for Figure 14. Figure 15 shows histograms for the 150 γ's from the $K_{\pi_2\gamma}$ candidates and the 198 γ's from the Type S (short range) calibration events. Figure 16 is a histogram of the combination of 71 γ's from Type L calibration events and 265 γ's from the other $K_{\mu 2}$ background runs. The error flags are statistical errors; the dashed curves are the expected histograms for an exponential conversion point distribution normalized to the number of events considered and using $\lambda = 9.5$ plates. $P(\chi^2)$ is again the χ^2 probability for the data to fit an exponential distribution with $\lambda = 9.5$ plates.

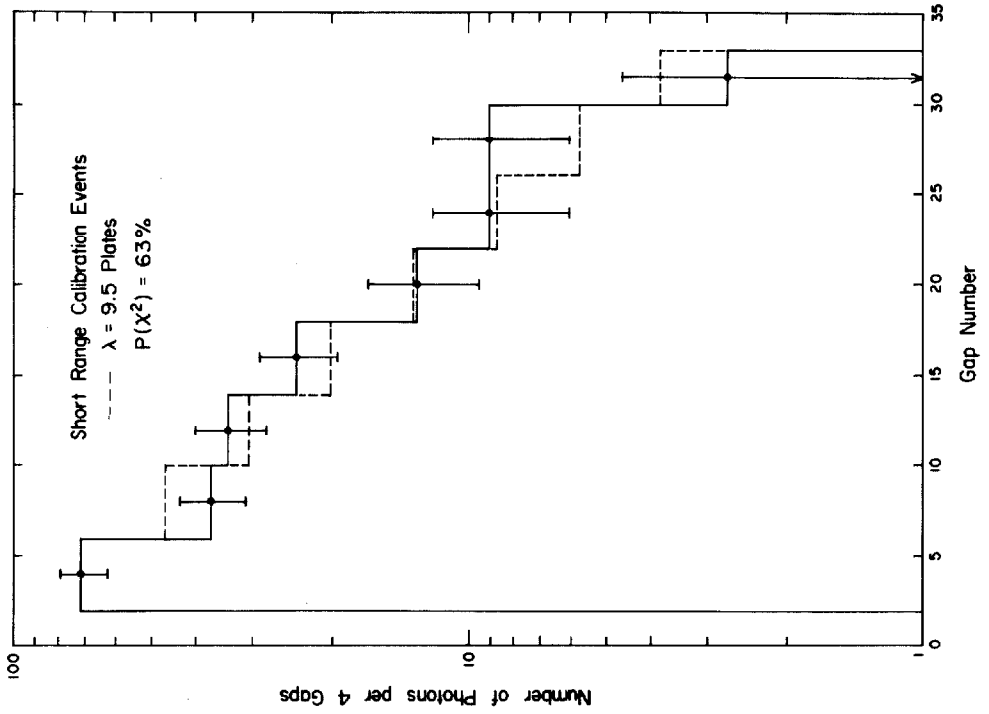
Short Range Calibration Events
--- λ = 9.5 Plates
P(X²) = 63%
Number of Photons per 4 Gaps
Gap Number

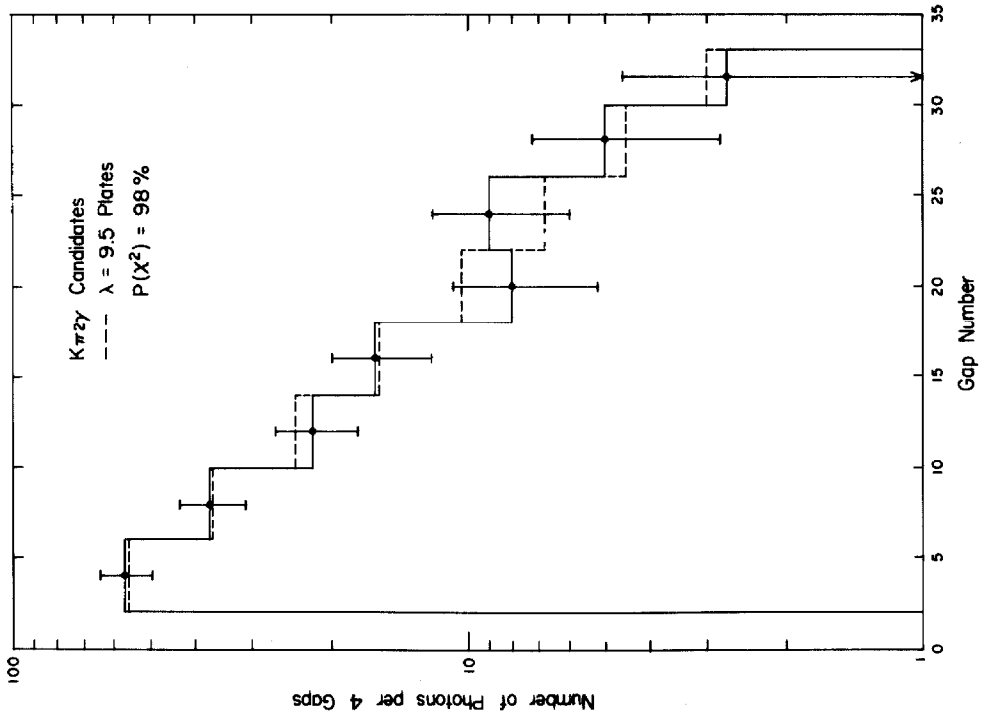
Kπ2γ Candidates
--- λ = 9.5 Plates
P(X²) = 98 %
Number of Photons per 4 Gaps
Gap Number

Figure 15

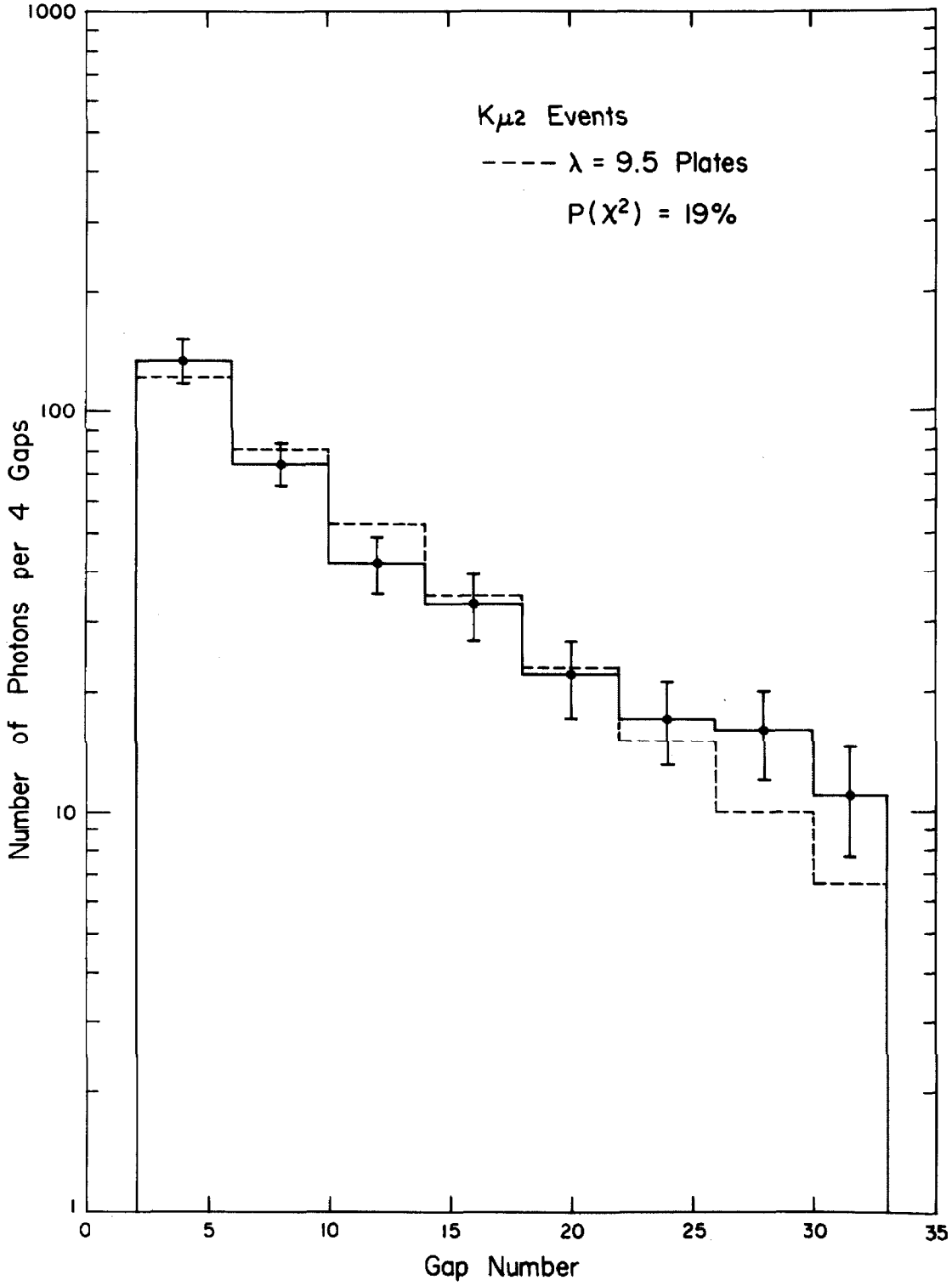
Kμ2 Events
---- λ = 9.5 Plates
P(χ²) = 19%
Number of Photons per 4 Gaps
Gap Number
1000
100
10
1
0
5
10
15
20
25
30
35

Figure 16

photon $K_{\pi 2}$ events. Instead of kinematic fits, the evidence will be limited to γ angular distributions and the relative number of zero, one and two γ events.

It is also desirable to understand the behavior of the accidental photons in the calibration runs. If accidentals from the stopper are due to beam π's interacting in the stopper one expects a nearly uniform azimuthal angular distribution for these γ's. Thus for $K_{\pi 2}$ events, which can have only accidental γ's, one expects equal number of γ's in each chamber. The data for type L calibration events are plotted below and show approximately, considering the poor statistics, this expected behavior:

TYPE L γ AZIMUTHAL ANGULAR DISTRIBUTION

(71 γ's)

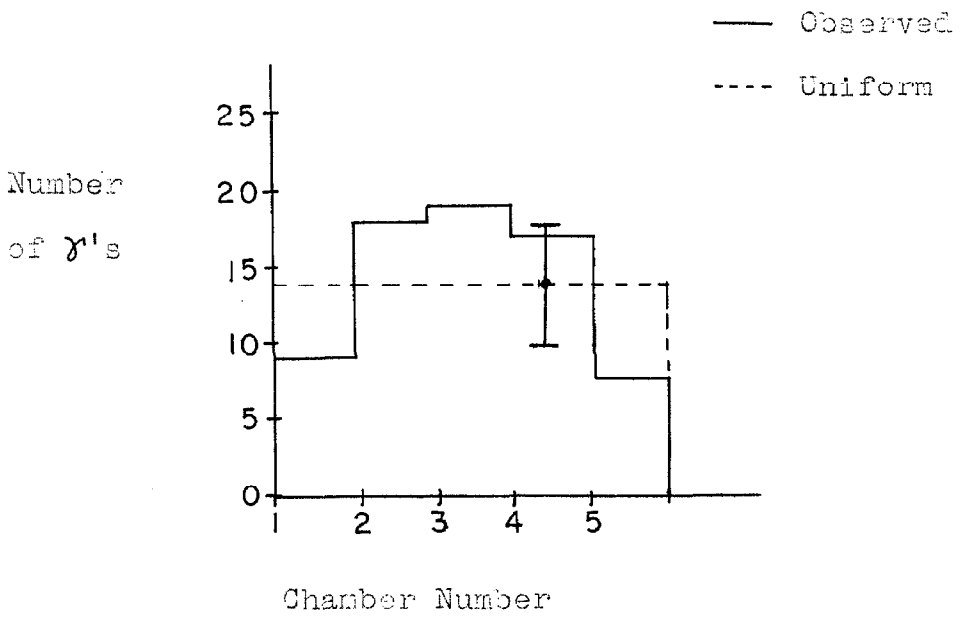

The distribution of the number of γ's per frame would be Poisson if the γ's were completely random. The two γ's from the decay of a π^o produced by π^+ charge exchange in the stopper are correlated. The extent to which this correlation modifies the Poisson distribution depends on the probability that both γ's enter the chambers and convert. The data for type L events tabulated below would indicate a small chance for both γ's entering the chambers:

TYPE L γ DISTRIBUTION

Number of γ Frames	Number of Frames Observed	Poisson Fit
0	234	226
1	44	55
2	6	7
3	5	1
Total	289	289

For the $K_{\pi 2}$ case, apart from accidentals, the γ's for the π^o decay should be peaked in chamber 3 opposite the π hodoscope. A Monte Carlo program described in more detail in Appendix VI was coded to compute the azimuthal angular distribution for one and two γ events, the γ conversion point distributions, and the relative number of zero, one, and two γ events. The results of the calculation -- after being corrected for accidentals, as determined from type L events, for the dilution from $K_{\pi 2}$ events,

and for conversions of γ's in the stopper - compare favorably with the data for type S events which are plotted below:

TYPE S γ DISTRIBUTION

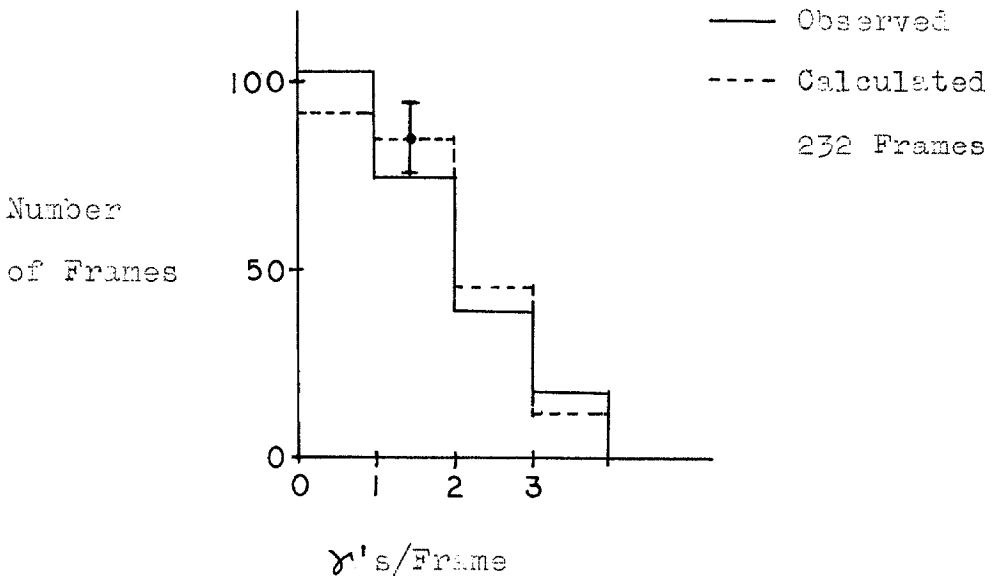

TYPE S γ AZIMUTHAL ANGULAR DISTRIBUTION

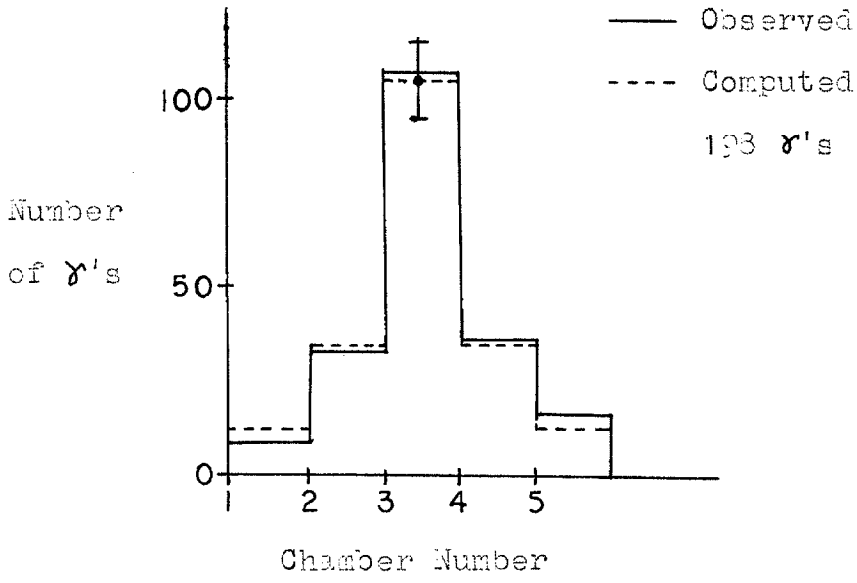

On the basis of the K decay branching ratios in Table I in Section I and solid angle considerations in the hodoscope, type S events are computed to be 60% $K_{\pi 2}$ and 40% $K_{\mu 2}$, while type L should be nearly 100% $K_{\mu 2}$. These considerations also predict the value of the ratio,

$$\frac{\text{No. of Type S events}}{\text{No. of Type S + No. of Type L Events}}$$

to be 0.38 ± 0.03, which is compared with the observed value of 0.44 ± 0.04.

3. Backgrounds

The background rate of accidental γ's for the $K_{\pi_2 \gamma}$ runs would be best obtained by triggering the spark chambers in the middle of the beam spill in a way uncorrelated with particles going through the K telescope. One way is to use a trigger with given delay from the start of the spill. This was done in the earlier part of the experiment well before the spark chambers were rebuilt. The data from this run are presented below:

γ ACCIDENTALS

γ/Frame	No. Frames
0	157
1	40
2	3
	200

Chamber	No. γ's
1	7
2	9
3	14
4	6
5	10
	46

One observes that (22 ± 3)% of the frames had accidental photons, and that, within the statistics, the γ's are uniformly distributed over the chambers.

During the part of the experiment which was analyzed for $K_{\pi_2\gamma}$ some runs were made triggering on $K_{\mu 2}$ events for checking the $K_{\mu 3}$ experiment. The triggering rate was low, about one event per two beam pulses. This insures that one is averaging over all the beam spill profile and not just over the lower intensity front part as in the case of the calibration runs. The γ like tracks show the proper conversion length for photons and are distributed uniformly over the chamber. These 265 γ's were combined with the 71 γ's from type L events of the calibration runs to give the conversion point distribution plotted in Figure 14. The γ angular distribution is plotted below:

γ AZIMUTHAL ANGULAR DISTRIBUTION

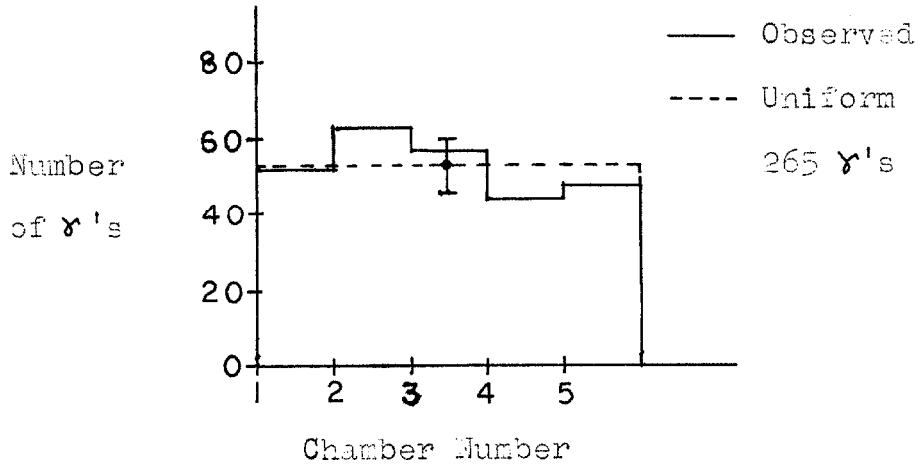

The distribution of the number of γ's per frame is tabulated below and is compared with a Poisson distribution using the average number of photons actually observed:

γ DISTRIBUTION

γ/Frame	Number of Frames	
	Observed	Poisson (av. = 0.382)
0	501	475
1	134	181
2	49	35
3	11	4
Total	695	695

The deviation from the Poisson distribution indicates slightly more multiple γ accidentals than expected. One contribution to the excess of multiple γ accidentals arises from the fact that there are two γ's from a π^o decay and occasionally both may be detected. The model giving the Poisson distribution assumes the γ's are uncorrelated in space and time. Inelastic charge exchange scattering where another π^o is produced would also increase the fraction of multiple γ's. Also, on occassion, a shower from a single photon will be mistaken for two showers because a shower electron happened to produce a wide angle bremsstrahlung where the secondary photon converts several gaps away.

The last data presented show that (28 ± 2)% of the frames had one or more accidental γ's. The previously discussed sample from the early part of the experiment was lower with (22 ± 3)%. The best that can be concluded is that accidental γ's occur for 20 to 30% of the frames and that they are mostly single γ events which are nearly uniform in their azimuthal distribution.

Charged particles are detected as tracks that have sparks in first and second gaps of the γ chambers. Most charged particles will be accidentals from π^+ scattering in the K telescope and stopper because essentially none can come from K^+ decay triggers. One possibility is from τ decay, however, for τ events with π's that get into channel 1, very few of the other charged π's have enough energy to get out of the stopper and penetrate three plates of the γ chambers. Another possibility is electrons from the conversion of photons in the stopper. However, only about 10% of the photons produced in the stopper will convert there. Charged particles, if they are as prevalent as photons, can thus serve as a monitor on the accidental rates.

Thirty-eight percent of the 695 frames from the $K_{\mu 2}$ events discussed earlier had charged particles. These charged particles behave as expected for charged π's scattered from the beam. The angular distribution is uniform as an examination of the following plot will show.

CHARGED PARTICLE AZIMUTHAL ANGULAR DISTRIBUTION

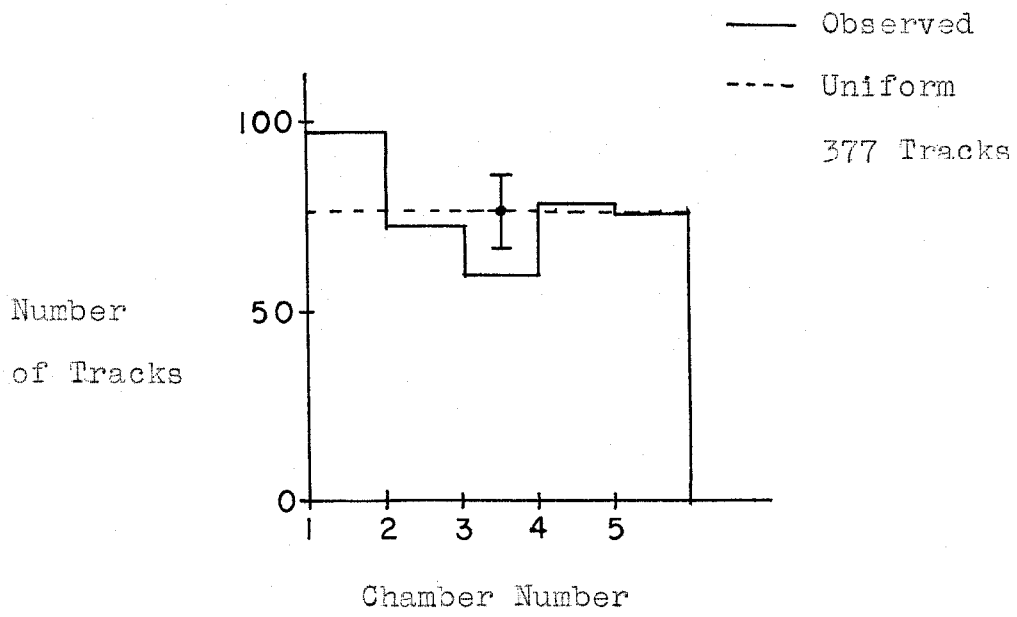

The distribution of charged particles per frame is tabulated below and is compared to a Poisson distribution using the observed average.

CHARGED PARTICLE DISTRIBUTION

Charged/Frame	Number of Frames	
	Observed	Poisson (ave. = 0.543)
0	430	404
1	170	219
2	82	60
3	9	10
4	4	2
Total	695	695

Here as with the accidental γ's slightly more two track events were observed than were expected from Poisson statistics. Inelastic π^+ scattering where another π^+ is produced and observed would increase the fraction of two track events.

If charged particles are to be a good monitor of accidentals, then the ratio of γ accidentals to charged accidentals should be constant and independent of the accidental rate. This is the case for the two different $K_{\mu 2}$ runs which had considerably different accidental rates. The average number of accidental γ's per frame was 0.25 ± 0.030 for the calibration run and 0.38 ± 0.023 for the other $K_{\mu 2}$ run, while the ratio of the number of γ accidentals to charged accidentals is very nearly the same for both runs, i.e., 0.79 ± 0.12 for the first and 0.70 ± 0.056 for the latter.

4. Channel 1 and 6 Events

It is now possible to discuss the spark chamber evidence referred to earlier which corraborates the fast display evidence showing that the π^+ identification criteria worked. The evidence consists mainly of three experimental distributions which are derived from channel 1 or 6 events and which can be compared with predictions for their behavior. For channel 1 the total number of events can also be predicted. Three distributions are considered; one is the distribution of the number of γ's per frame, another is the γ azimuthal angular distribution and the other is the distribution of the height (Y_K) of the stopping K^+ in the stopper. The situation for channel 1 will be discussed first and followed by a consideration of channel 6.

a. Channel 1

The events with good π-μ decays which stop in channel 1 of the π^+ hodoscope should be τ and τ' decays. The predictions of the total number of events and of the two γ distributions are described in detail in Appendix X. The predictions are limited by uncertainties of experimental numbers for the high energy portions of the π^+ spectra from τ and τ', the stopping K^+ height (y coordinate) distribution in the stopper and the branching ratio for τ and τ'. The calculation described in Appendix XI predicts 330 channel 1 events, 16% of which are τ and 84% τ'. Three hundred sixteen events were observed, a number which is in excellent agreement with the predicted number. The distribution of number of γ's per frame agrees with the prediction when accidentals are included in the calculation. The data and predictions are tabulated below:

γ DISTRIBUTION (CHANNEL 1)

γ/Frame	Observed Number of Frames	Predicted No. of Frames with accidentals	Predicted No. of Frames No accidentals
0	175	192	268
1	92	64	13
2	26	35	19
3	18	17	13
4	4	6	3
5	1	2	0
Total	316	316	316

It should be noted that accidentals contribute over half the total number of γ's in the predictions. The charged particle distributions, both the distribution of number per frame and the azimuthal angular distribution, agree quite well with those obtained from the $K_{\mu 2}$ background runs discussed in Section III C 3. Detailed considerations are presented in Appendix XII; the main point is that agreement between charged particle distributions and rates for the background runs and the channel 1 events is evidence that γ accidental distributions and rates for both should also agree.

Because the two π's from the τ' decays that can be observed in channel 1 are moving slowly, their γ angular distribution should be nearly uniform. Accidentals should also be uniformly distributed; therefore it is expected that all γ's for channel 1 events should be uniformly distributed. The data plotted below agree with this prediction.

γ AZIMUTHAL ANGULAR DISTRIBUTION (CHANNEL 1)

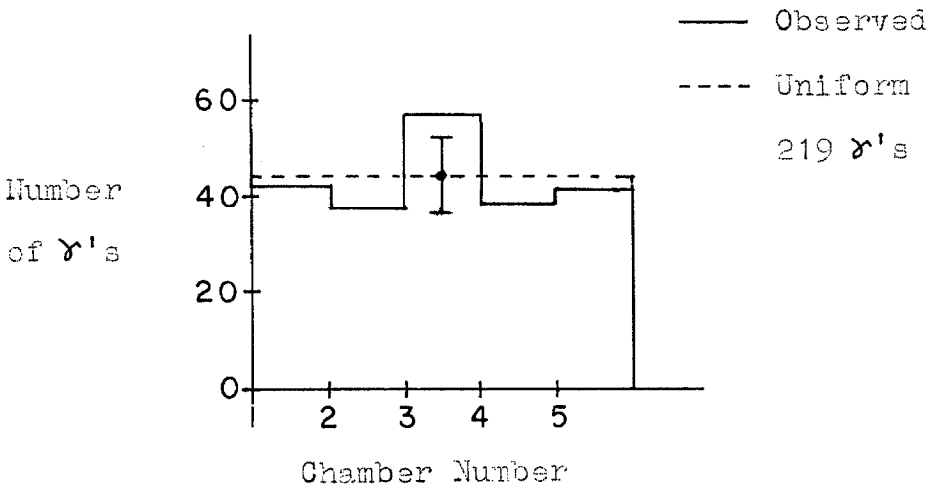

One last item of qualitative evidence supporting the conclusion that the channel 1 events are τ and τ' decays is seen in the distribution of the height of the K^+ (y coordinate) in the stopper. Most π^+'s from τ or τ' decays cannot get into channel 1; only those that stop near the top of the stopper or those that have an energetic π^+ can reach channel 1. Thus, an enhancement of the larger y coordinate values is expected for τ and τ' events compared to an unbiased stopping K^+ distribution. Such an enhancement is seen in the channel 1 data plotted below when a comparison is made with the distribution obtained from the $K_{\pi 2}$ and $K_{\mu 2}$ calibration events. The calibration events form an unbiased sample with respect to the position of stopping K's.

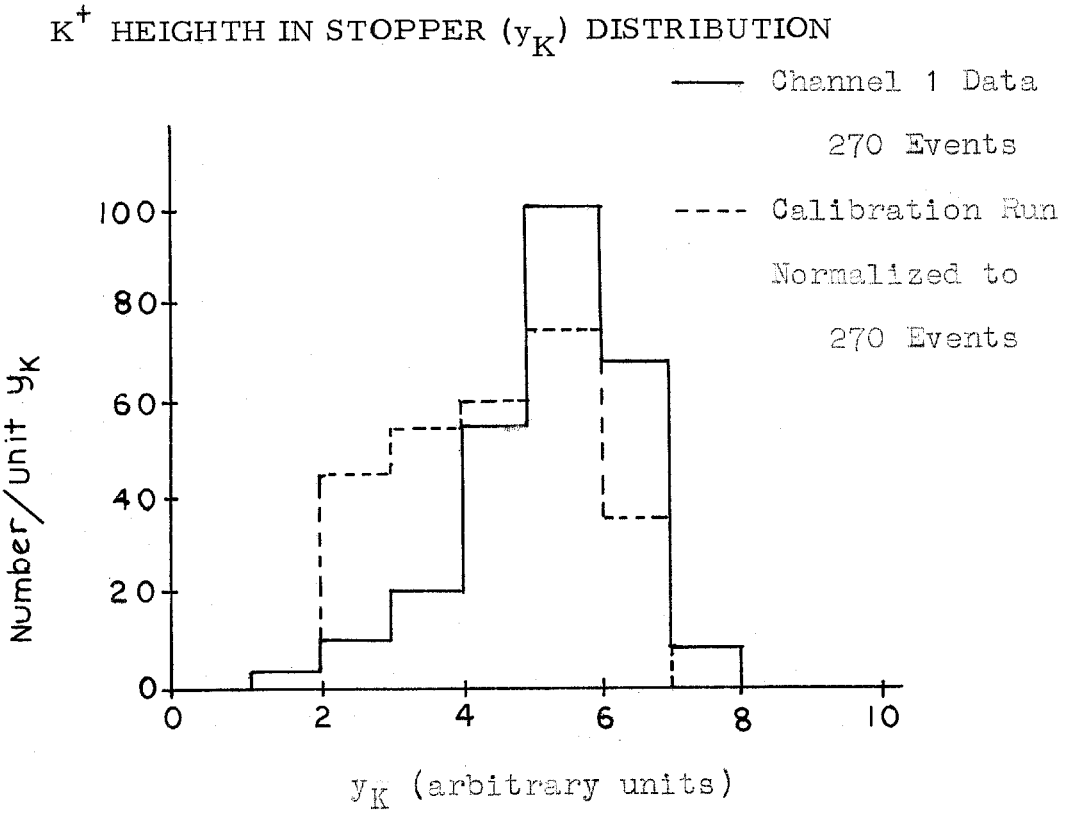

b. Channel 6

For channel 6 it is more difficult to predict what should happen. A good prediction requires a careful computation using good differential scattering cross sections, a good range energy relation, a good range straggling distribution, an accurate stopping K spatial distribution and attention to geometrical effects; particularly to compute the expected number of events. What can be done, however, is to compare the angular distribution of γ's and the distributions of the number of γ's per frame with what is expected for simplified models.

One model, denoted as model A, assumes that all channel 6 events are ordinary $K_{\pi 2}$ events plus accidental photons except that something happens to the π^+ after the π chamber to cause it to stop in channel 6. The π^+ may inelastically scatter in the wedge or hodoscope or it may scatter elastically and increase its actual range through geometrical effects. The other model, labeled B, assumes that all channel 6 events are $K_{\pi 2}$ inelastic interactions in the stopper. Model B uses the results of the Monte Carlo program described in Appendix VII for those scattered π's that stop in channel 6. The predictions for model A have been discussed previously in Section III D 2 and in Appendix VI. For Model B certain differences with respect to A are observed; i.e., the number of zero γ events increases and the γ's peak in chambers 1 and 5 instead of 3. These differences arise because the inelastic scattering cross section peaks in the backward direction; therefore

the π^o distribution will be peaked toward the hodoscope. The experimental distributions and the predictions for channel 6 based on model A, model B and an equal mixture of the two are tabulated and plotted below:

γ DISTRIBUTION (CHANNEL 6)

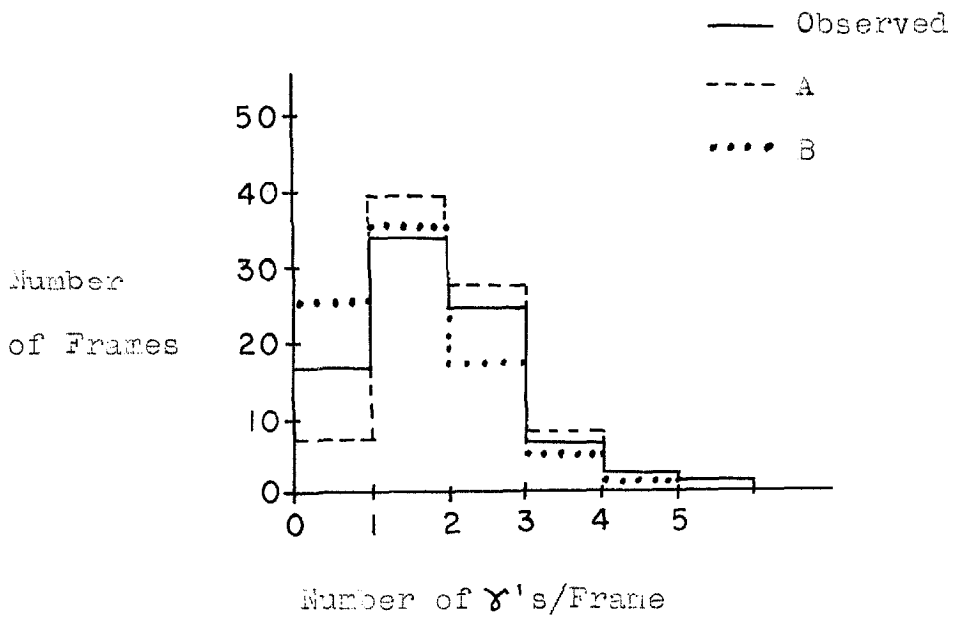

γ DISTRIBUTION (CHANNEL 6)

		Predicted No. of Frames		
γ/Frame	Observed No. of Frames	A	B	(A + B)/2
0	16	7	25	16
1	34	39	35	37
2	24	27	17	22
3	6	8	5	6
4	2	2	1	2
5	1	0	0	0
Total	83	83	83	83

γ AZIMUTHAL ANGULAR DISTRIBUTION

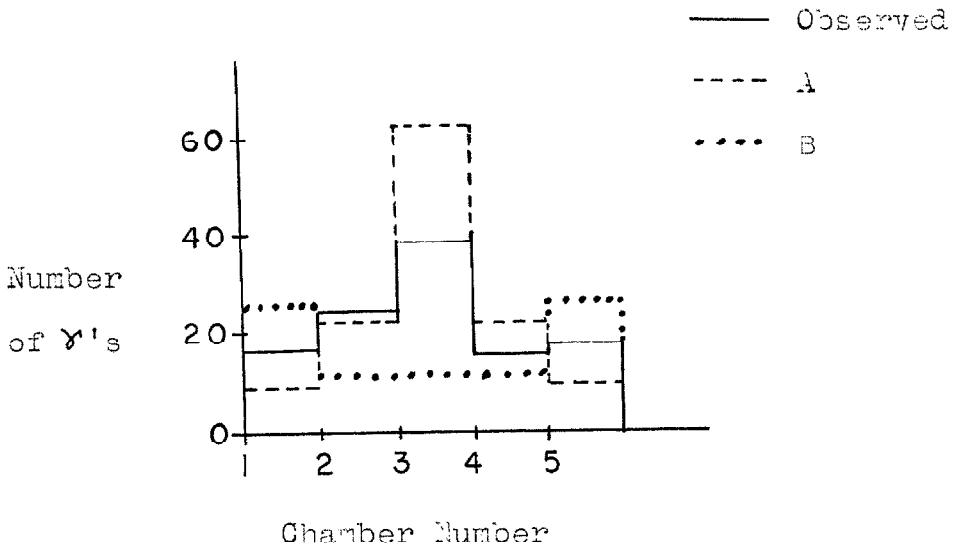

γ AZIMUTHAL ANGULAR DISTRIBUTION (CHANNEL 6)

Chamber	Observed No. of γ's	Predicted No. of γ's		
		A	B	(A + B)/2
1	17	9	26	17
2	24	22	12	17
3	38	64	12	38
4	16	21	12	17
5	18	9	26	18
Total	113	125	88	107

The predictions have been normalized to the 83 frames. From these results it can be seen that the data best agree with a mixture of the two models.

The distribution of the y coordinate of the stopping K for single K chamber tracks is shown below and agrees well with the distribution for the unbiased calibration events.

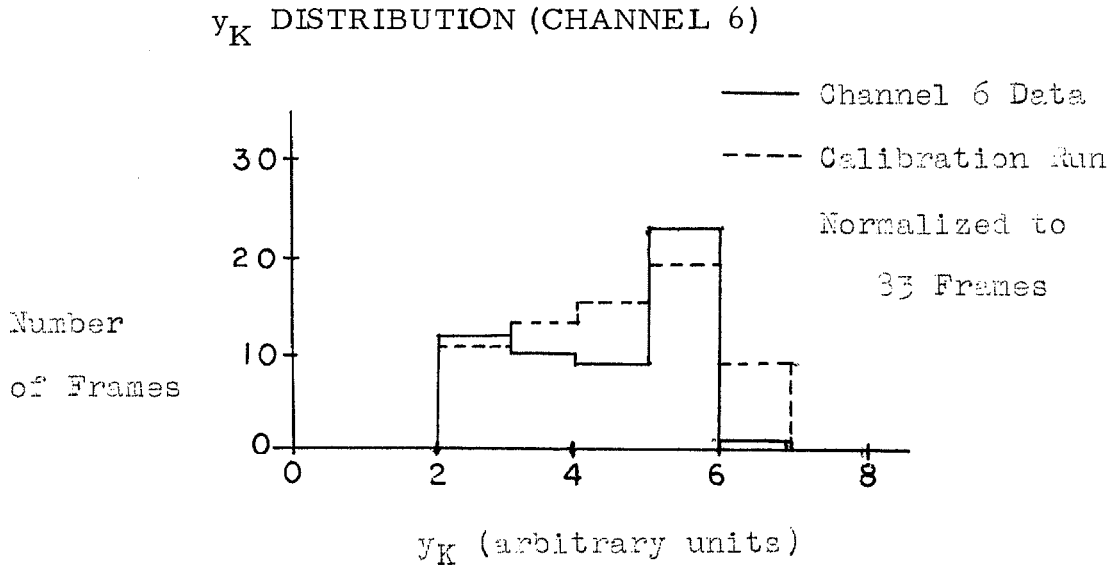

For channel 6 as well as for channel 1 and the 174 $K_{\pi_2\gamma}$ candidates the charged particle data agree with the data for the $K_{\mu 2}$ background runs. The conclusion is that γ accidental rates and distributions of the $K_{\mu 2}$ background runs can be used for the channel 1 and 6 events and the 174 $K_{\pi_2\gamma}$ candidates. Appendix XII presents the charged particle data in more detail.

c. Summary

In brief, the main features of the channel 1 events are in agreement with what is expected for τ and τ' events and they differ significantly from channel 6 events, which are

consistent with being normal $K_{\pi 2}$ or $K_{\pi 2}$ inelastically scattered events. For channel 1 many frames have no γ's; the γ's are uniformly distributed over the chamber and the K's stopped high in the stopper. For channel 6 nearly every frame has at least one γ; the γ's are peaked in chamber 3 and the stopping K's y coordinate distribution is more nearly uniform. The number of channel 1 events agrees with what is expected for τ and τ' triggers. This evidence indicates that the scheme for identifying π^+ from K decays did work with the computed efficiency.

5. Spark Chamber Data for the 174 $K_{\pi_2\gamma}$ Candidates

The 174 $K_{\pi_2\gamma}$ candidates were those events where a π-μ decay was observed for a particle stopping somewhere in channels 2 through 5 of the K^+ hodoscope. In addition a "good" π chamber track was required. The final step in the analysis would be to utilize those events with three or more photons and make kinematic fits in order to isolate the $K_{\pi_2\gamma}$ events. Before proceding to the kinematic fits, the qualitative spark chamber data pertaining to various distributions of γ tracks will be presented for the 174 $K_{\pi_2\gamma}$ candidates. The charged particle data are discussed in Appendix XII and show no change in the accidental rates or distributions.

Channel 2 can still be reached by π^+'s from τ and τ'. For this reason channel 2 events are separated from events in channels 3 through 5 in the discussion that follows. Assuming that all of the channel 2 events are τ and τ', the previous predictions for

channel 1 can be normalized to the number of channel 2 events for a comparison with the data. This was done for the two plots that follow.

γ DISTRIBUTION (CHANNEL 2)

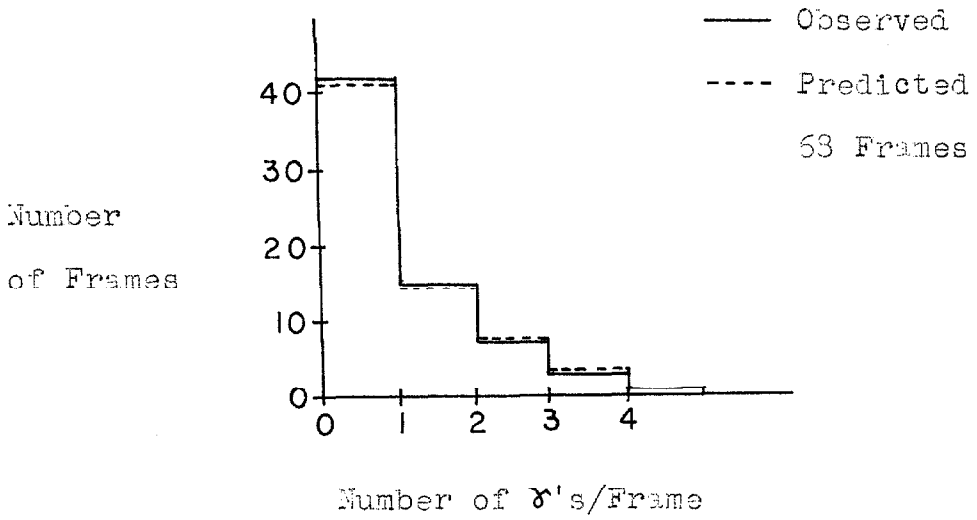

γ AZIMUTHAL ANGULAR DISTRIBUTION (CHANNEL 2)

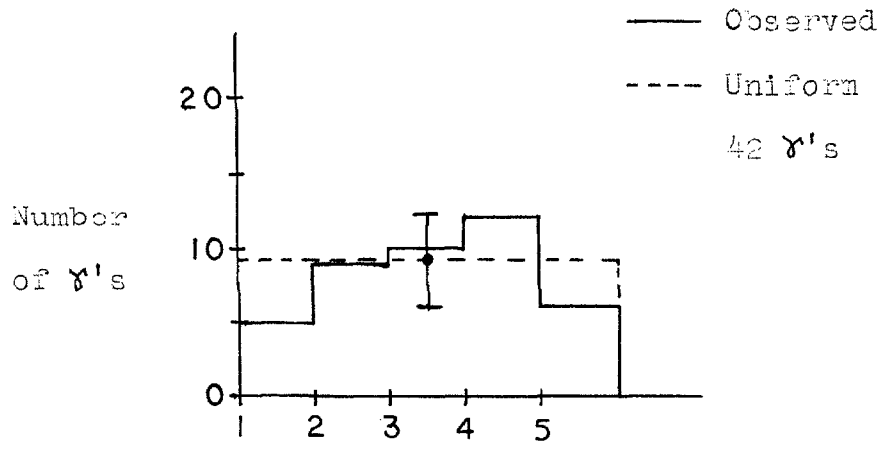

A total of 46 photon tracks is predicted compared to 42 observed for channel 2.

In the plots that follow the data for channels 3 through 5 are compared to predictions made assuming equal numbers of $K_{\pi 2}$ interactions in the stopper and in the hodoscope. Interactions in the hodoscope will give nearly the same γ distribution as the case where the π goes through the hodoscope. The Monte Carlo calculation, described in Appendix VII, provides the expected γ distributions for the $K_{\pi 2}$ interactions in thestopper. Using an equal admixture of the two types of $K_{\pi 2}$ interactions normalized to the 106 frames observed, 139 photon tracks are predicted compared to 108 observed.

γ DISTRIBUTION (CHANNELS 3 THROUGH 5)

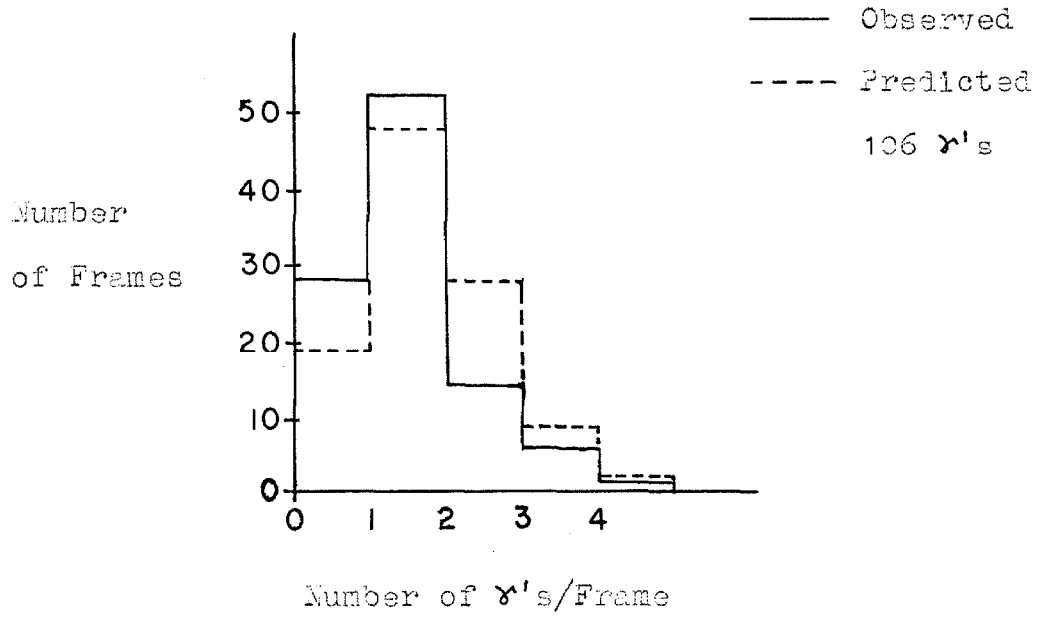

γ AZIMUTHAL ANGULAR DISTRIBUTION
(CHANNELS 3 THROUGH 5)

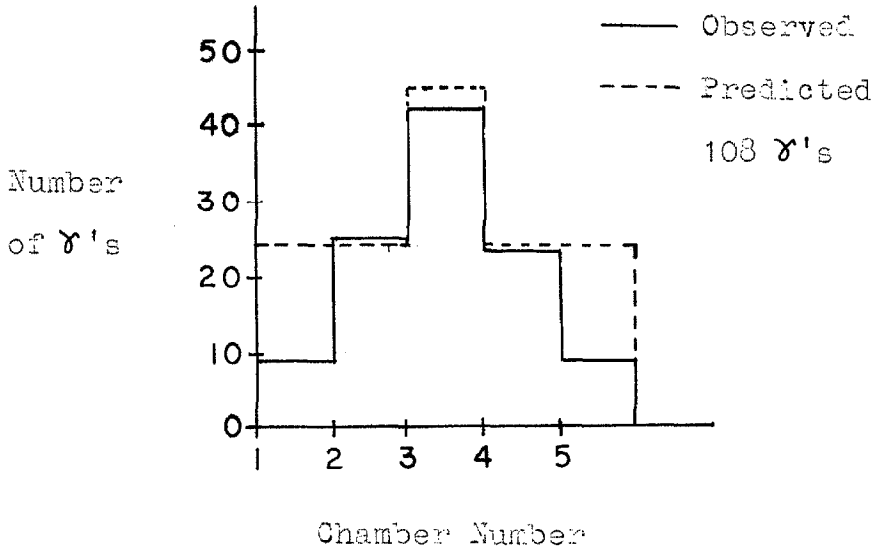

There are two main features of the γ data plotted above:

(a) Channel 2 has many frames devoid of γ's and seems to agree with what is expected of τ and τ' events.

(b) Channels 3 through 5 have a higher fraction of frames with γ's and the γ's are peaked away from the hodoscope. The data are only roughly consistent with predictions based on equal numbers of $K_{\pi 2}$ events interacting in the stopper and $K_{\pi 2}$ events interacting after the π chamber.

In principle, if there were no accidentals present, observing three photons with an intermediate range π^+ from a K^+ decay would be sufficient to identify $K_{\pi_2 \gamma}$. Without resorting to

kinematic fits, an upper limit on the branching ratio is obtained by requiring three or more photons in the γ chambers.

However, the refinement of the branching ratio obtained by utilizing the qualitative spark chamber information is small. Eleven of the 174 candidates have three or more γ's, but the efficiency of $\sim 15\%$ for the detection of all three γ's makes up for the reduction in number of candidates so that one has nearly the same upper limit as before. Two of the eleven events have FC-75 pulses and two or three more have poor pulse height fits. The 6 or 7 remaining events give an upper limit of approximately 1×10^{-3} on the $K_{\pi_2\gamma}$ branching ratio.

E. Kinematic Fitting

1. Description

Since most of the $K_{\pi_2\gamma}$ candidates, even those with 3 γ's, can be explained as $K_{\pi 2}$ interactions plus accidental γ's, kinematic fitting must be relied on to select $K_{\pi_2\gamma}$ events from the backgrounds. Figure 5, which was seen earlier in Section II indicates the measurements used for kinematic fitting. Measurements on the spark chamber photographs, which were made with a digitized measuring table and reduced to meaningful numbers by computer programs, locate the points of conversion of the γ's, (i.e., $\vec{R}_1$, $\vec{R}_2, \vec{R}_3$), the point $\vec{P}_K$ where the K^+ entered the stopper, and two points on the π^+ trajectory chosen for convenience to be $\vec{R}_4$ and $\vec{R}_5$. Because only one gap of the K chamber was working the K^+

direction was lost; however, since the K^+ beam was confined to 5^o the one point, $\vec{P}_K$, where the K entered the stopper gives the x and y coordinates of the decay vertex, $\vec{R}_o$, to about 0.5 cm for an average K. Measurements of the π chamber track yield the parameters of the π trajectory which were chosen to be the two points, $\vec{R}_4$ and $\vec{R}_5$. The π^+ direction plus the pulse height in the stopping counter give the range of the π^+ in the hodoscope.

These measurements were fit in the maximum likelihood sense, or since all errors were treated as gaussianly distributed, in the minimum χ^2 sense to the "best" parameters describing each event. This procedure yields not only the "best" value of parameters describing the event, but also the value of χ^2 at the minimum which can be used for a "goodness of fit" criterion.

The details of the fitting procedure are treated in Appendix VIII. The basic method is to write down the log of the likelihood function which in this case is:

$$-\log L = W = \sum_{i=1}^{N} \frac{(d_i - f_i(\vec{P}))^2}{2\,\sigma_i^2(\vec{P})} + \sum_{i=1}^{N} \log \sigma_i(\vec{P}) + \text{const.}$$

where the d_i are the measurements, the σ_i are the standard errors on the measurements which can be a function of the parameters $\vec{P}$, and the f_i are known functions of the parameters describing the event as a $K_{\pi_2\gamma}$ decay. W is minimized with respect to the m dimensional parameter variable, $\vec{P}$, to obtain the best values for the parameters. Because the variations of $\log \sigma_i$, for this problem, are negligible

compared to variation of the first sum, the method becomes a least squares or minimum chi squared method, with χ^2 equaling twice the value of the first sum evaluated at the minimum. The minimization of this formidable function was accomplished with computer programs using the "Variable Metric" minimization package of W. C. Davidon (21) as the basic routine.

For kinematic fitting to be useful, especially when the χ^2 goodness of fit criterion is to be used, the errors must be known with accuracy. The complete list of errors in Appendix X shows that the major uncertainties are in the location of the decay vertex. The large uncertainties here are most crucial because they affect all angles of the γ's and the range of the π^+. Uncertainties in the x and y coordinates of vertex arise from the following causes:

(a) The K^+ beam angular spread is about 0.1 radian and since the K^+ direction is not measured, the angular uncertainty means approximately 0.5 cm error in x and y coordinates for an average stopping K^+.

(b) Multiple scattering of the stopping K^+ in the stopper gives an error of about 0.2 cm.

(c) Uncertainties in the orientation of the K chamber mirrors lead to systematic uncertainties of about 0.3 to 0.5 cm.

For the z coordinate great uncertainty arises from extrapolating an uncertain π direction back to the stopper. The polar angle of the

π has large uncertainties because the depth measurements have large errors and because the sample of the π trajectory seen by the π chamber is short. The depth uncertainty arises from the following causes:

(d) The small angle of the mirror means that a large factor (about 10 for one reflection, 5 for two reflections) relates distance between spark and reflection to the depth. This magnifies distance uncertainties to an error of 0.2 to 0.3 cm.

(e) The calibration of mirror angles is good to only 1 to 2%; this yields a depth error of 0.3 to 0.5 cm for an average depth of 25 cm.

These errors compound to give a vertex uncertainty of 1.1 cm (two reflections) and 1.8 cm (one reflection) for the z coordinate. The γ conversion points have depth errors of the order of 0.5 cm for the same reasons that the π^+ does. A more detailed discussion of errors is available in Appendix X.

A good test of the entire procedure is afforded by the $K_{\pi 2}$ calibration events. The π^+ range is not available, but like $K_{\pi_2\gamma}$ events, the kinematics are overdetermined by two parameters. Successful fitting of $K_{\pi 2}$ events will show that the error assignments are valid and give confidence in the application of kinematic fitting to the $K_{\pi_2\gamma}$ events.

2. Fits to $K_{\pi 2}$

All multiple track events in the calibration runs were measured and fitted to the $K_{\pi 2}$ hypothesis. When more than two γ tracks were encountered, fits with various combinations of tracks taken two at a time were made. The resulting χ^2 distribution for all the two γ fits is shown in Figure 17. For comparison, the χ^2 distribution for 3 degrees of freedom, normalized to the number of events with $\chi^2 < 12$, is also shown. The peak in the data at $\chi^2 \simeq 2.5$ which is clearly separated from the poor fits, is heartening to see. It shows that the errors are fairly well determined, since for example, a 30% decrease in errors would scale χ^2 up by a factor of 2.

The number of good fits, 36, agrees well with the 38 expected on the basis of a calculation discussed in Appendix XI. Further agreement is found between the distribution of a π^o decay parameter, for example, the opening angle of the photons, and the expected distribution. Both the experimental and the expected opening angle distributions are shown in Figure 18.

3. Fits to Backgrounds

One question which the calibration events do not answer about the quality of the fitting procedure is the probability for backgrounds to fit. The number of three γ events in the calibration runs is not large enough to answer this question experimentally so two different types of backgrounds were calculated by Monte Carlo methods.

FIGURE 17

χ^2 DISTRIBUTION FOR $K_{\pi 2}$ KINEMATIC FITS

The observed χ^2's for fits to all two γ events of the calibration runs for the $K_{\pi 2}$ hypothesis are plotted in this figure. When more than two γ tracks were encountered in an event all two γ combinations were fit. The dashed curve is the histogram for a χ^2 distribution of 3 degrees of freedom normalized to the number of events with $\chi^2 < 12$. The cutoff at 12 corresponds to a confidence limit of 1%.

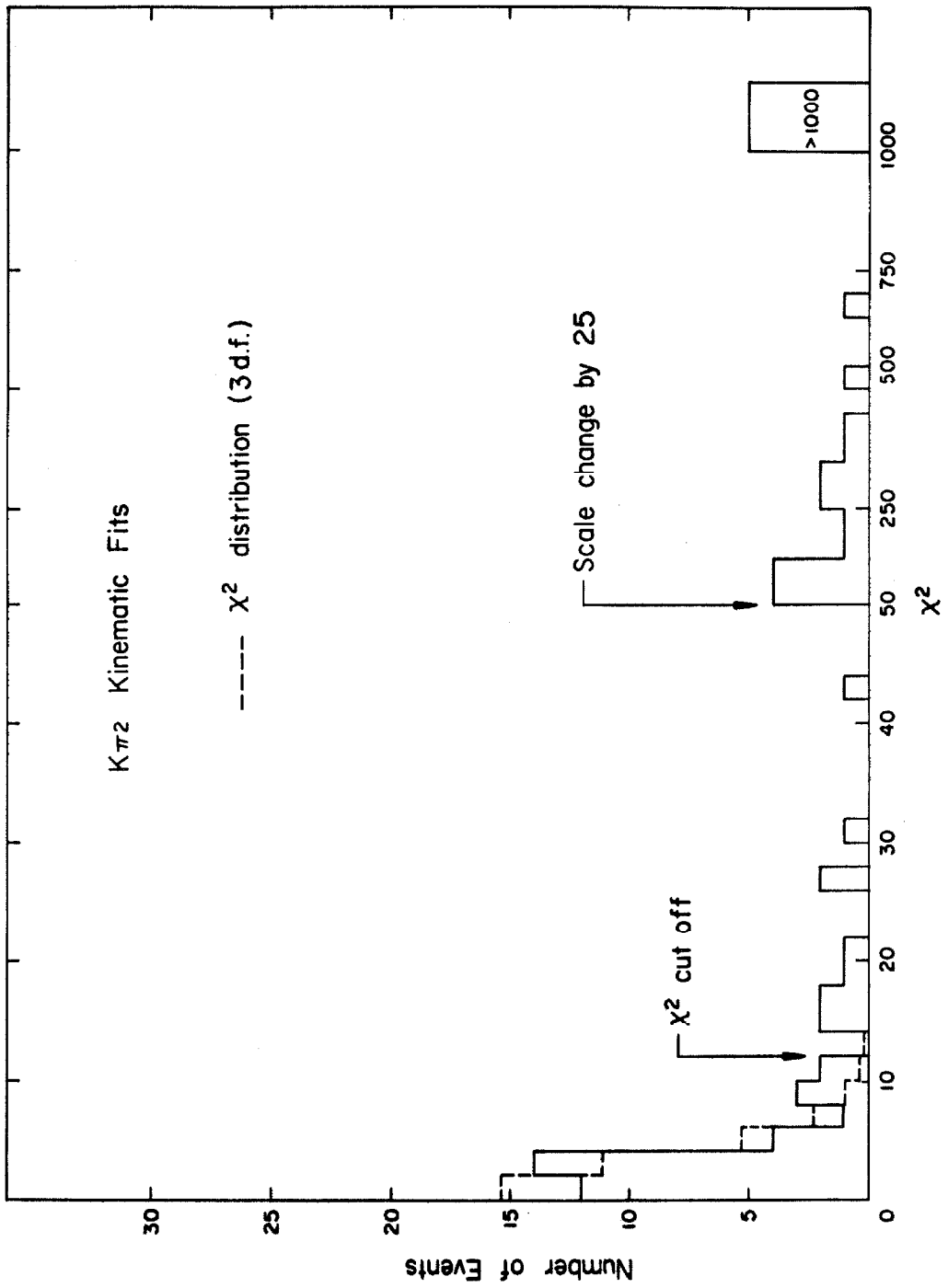
Kπ2 Kinematic Fits
---- χ² distribution (3 d.f.)
Scale change by 25
χ² cut off
Number of Events
χ²
>1000

Figure 17

FIGURE 18

OPENING ANGLE DISTRIBUTION

The opening angle distribution for the 36 events having $\chi^2 < 12$ for fits to the $K_{\pi 2}$ hypothesis are plotted in Figure 18. The opening angle is expressed in radians; the histogram bin width is 0.1 radians. A dashed curve labeled "expected distribution" is the histogram expected from the monoenergetic π^o's of $K_{\pi 2}$ decays. For these π^o's, the minimum opening angle is 1.16 and is shown in the figure.

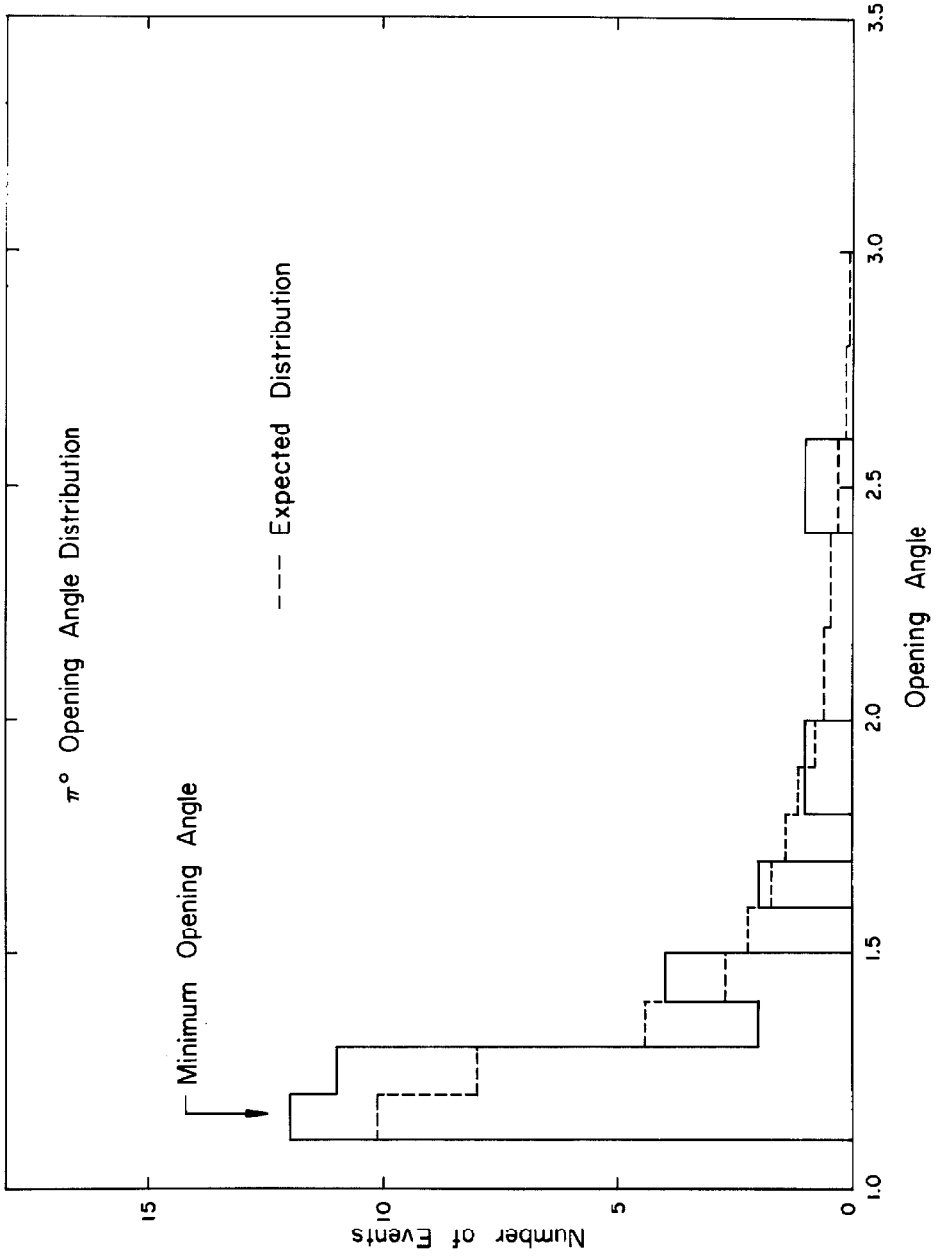
π° Opening Angle Distribution
--- Expected Distribution
Minimum Opening Angle
Number of Events
Opening Angle
0
5
10
15
1.0
1.5
2.0
2.5
3.0
3.5

Figure 18

The first model for a $K_{\pi 2}$ background is a $K_{\pi 2}$ decay with one photon from the π^o and one accidental photon. These were generated by taking $K_{\pi 2}$ events that fit and substituting for one observed γ a random γ generated with pseudo-random numbers such that the random γ's have isotropic spatial distributions. The second model used two random γ's substituted for the real ones. The events so generated for either model were then fit by the usual $K_{\pi 2}$ fitting procedure. For the first model 13% of the 180 events tried gave acceptable fits when using a χ^2 cut-off equal to 12, while for the second model 4.5% of the 180 events tried gave acceptable fits. The events that fit were mostly those with wide opening angles or, said another way, those with a very asymmetric energy partition of the π^o photons. These are easy to fit because the kinematic parameters are insensitive to changes in the direction of the backward photon, i.e., almost any backward γ direction will do.

Kinematic fitting to $K_{\pi_2\gamma}$ has one additional complication which increases the chance for backgrounds to fit. An inherent ambiguity in identifying the primary photons necessitates making three different fits, choosing each time a different pair of γ's as coming from the π^o decay. The $K_{\pi_2\gamma}$ kinematic fits are also subject to a greater variety of backgrounds than $K_{\pi 2}$ of which essentially three kinds were considered, namely:

(a) $K_{\pi 2}$ events with accidental γ's where the π^+ inelastically scattered in the stopper.

(b) $K_{\pi 2}$ events with accidental γ's where the π^+ inelastically scattered after the π chamber.

(c) Events with all accidental γ's.

Events of type (a) were generated by adding one or two random γ's to the $K_{\pi 2}$ interaction events generated by the Monte Carlo program described in Appendix VII which computed contributions from π^+ inelastic scattering in the stopper. The results of fits to these events for one or two random γ's are summarized in the first two rows of Table VII. Events of types (b) and (c) were generated by using the $K_{\pi 2}$ events that gave good fits to the $K_{\pi 2}$ kinematics and adding a π^+ having the range distribution observed for the 174 $K_{\pi_2\gamma}$ candidates. The three γ's for these events contained either one, two, or three randomly generated γ's and either two, one or zero real γ's respectively. The results of fits to these events are tabulated in the last three rows of Table VII. Appendix IX describes more details of the kinematic background computations.

The most serious background, which has a 50% chance of fitting, is a $K_{\pi 2}$ event with one accidental γ where the π^+ interacts after the π chamber. Some, but not all, of this type of interaction will be rejected by the pulse height fitting criterion. One other possibility for detecting this serious type of background event is to fit the $K_{\pi_2\gamma}$ candidates to the $K_{\pi 2}$ hypothesis disregarding the π^+ range and using the three γ's two at a time. For this procedure to be useful it is desirable to know what the chance would be for a bona fide $K_{\pi_2\gamma}$ event to give a good $K_{\pi 2}$ fit. To compute this probability requires a detailed knowledge of the π^o spectra and of the γ-π^o correlations. In view of this fact and in view of the

TABLE VII

$K_{\pi_2\gamma}$ BACKGROUND FITTING RESULTS

For each type of background listed, five numbers are presented. The first three columns show the number of background events that were tried (A), the number of those tried that gave good fits (B), and (C) the results in column B presented as a percentage of the number tried. Column D shows the number of each type of background that would be expected in 174 triggers selected according to the criteria used for the 174 $K_{\pi_2\gamma}$ candidates. Column E gives the number of those events in D that would be expected, on the basis of the results in C, to give good $K_{\pi_2\gamma}$ kinematic fits.

TABLE VII

$K_{\pi_2\gamma}$ BACKGROUND FITTING RESULTS

	A	B	C	D	E
Type of background	No. Tried	No. Fit	% Fit	No. expected in 174	No expected to fit in 174
Type (a) with one random γ	51	0	0+1.3	~ 2	~ 0.03
Type (a) with two random γ's	59	7	12±5	~ 4	$\sim .5$
$K_{\pi 2}$ with one random γ	60	28	47±9	~ 5	~ 2.5
$K_{\pi 2}$ with two random γ	60	11	18±6	~ 5	~ 1
$K_{\pi 2}$ with three random γ	60	9	15±5	~ 1	$\sim .2$

limited number of events, such a calculation using a phase space or inner bremsstrahlung model was not made, although had the experiment been better it would have been useful.

4. Fits to $K_{\pi_2\gamma}$

Table VIII tabulates interesting parameters describing the eleven $K_{\pi_2\gamma}$ candidates with three or more γ tracks. Four of the eleven candidates have reasonable χ^2 for fits to the $K_{\pi_2\gamma}$ kinematics with three degrees of freedom. Spark chamber photographs of these four survivors are shown in Figure 19 through 22. Of these four, two or perhaps three give poor pulse height fits which leaves one or two events, 57344 and 54604, as likely $K_{\pi_2\gamma}$ events. These two events give a branching ratio of $\sim 2 \times 10^{-4}$ that is most honestly presented as an upper limit on the branching ratio.

One other attempt was made to improve the results. This was an attempt to eliminate accidental γ's by using measurements on the γ showers to get a measure of the γ direction independent of the decay vertex. The direction came from a fit to the first few sparks (up to seven) of the γ shower. The fitting procedure took into consideration measuring errors and multiple scattering of the shower particles, but the resulting angular resolutions of 8° for the azimuthal angle and 13° for the polar angle were not sufficient to be of great use in eliminating accidentals.

TABLE VIII

$K_{\pi_2\gamma}$ CANDIDATES HAVING THREE OR MORE γ'S

The frame number for each $K_{\pi_2\gamma}$ candidate with three or more γ's is listed in the first column of Table VIII. Column A gives the counter in which the π stopped; column B presents the χ^2 for fits to the pulse height data, and column C indicate whether the event produced an FC-75 counter pulse or not. Column D shows the smallest χ^2 obtained by fitting to the $K_{\pi_2\gamma}$ hypothesis using three γ's at a time until all three γ combinations were exhausted. In column E is shown the χ^2 obtained by fitting the π^+ direction and two of the three γ's, which were used to obtain the results in D, to the $K_{\pi 2}$ hypothesis. The γ's were used two at a time for all combinations of the three γ's and the smallest χ^2 is shown in E. Column F shows the π^+ kinetic energy as obtained from the $K_{\pi_2\gamma}$ fit whose χ^2 is shown in D.

TABLE VIII

$K_{\pi_2\gamma}$ CANDIDATES WITH THREE OR MORE γ'S

	A	B	C	D	E	F
Frame	Stopping Counter	χ^2 dL/dx	FC-75 Pulse	χ^2 $K_{\pi_2\gamma}$	χ^2 $K_{\pi 2}$	T_{π^+} (MeV)
51498	2A	42.0	No	5.0	0.4	49
54505	5B	4.1	No	29	4.0	69
54604	3A	33	No	1.4	4.2	67
54718	4A	355	No	1.7	8.2	82
56333	5B	0.9	Yes	539	10^5	79
56334	2B	1.4	No	8×10^4	5×10^4	65
56470	2B	0.3	No	26	35	47
56793	5A	1.3	Yes	129	154	80
57069	2B	0.6	No	193	157	48
57344	5A	3.1	No	5.9	222	78
58035	5A	4.5	No	4×10^4	62	82

FIGURES 19 THROUGH 22

SPARK CHAMBER PHOTOGRAPHS

Spark chamber photographs for the four $K_{\pi_2\gamma}$ events having χ^2's less than 10 are shown in these figures. Frame number 51498 is shown in Figure 19, 54604 in Figure 20, 54718 in Figure 21 and 57344 in Figure 22. Actually, the largest of the four χ^2's was 5.9 rather than 10; the confidence limit for 5.9 is 11%.

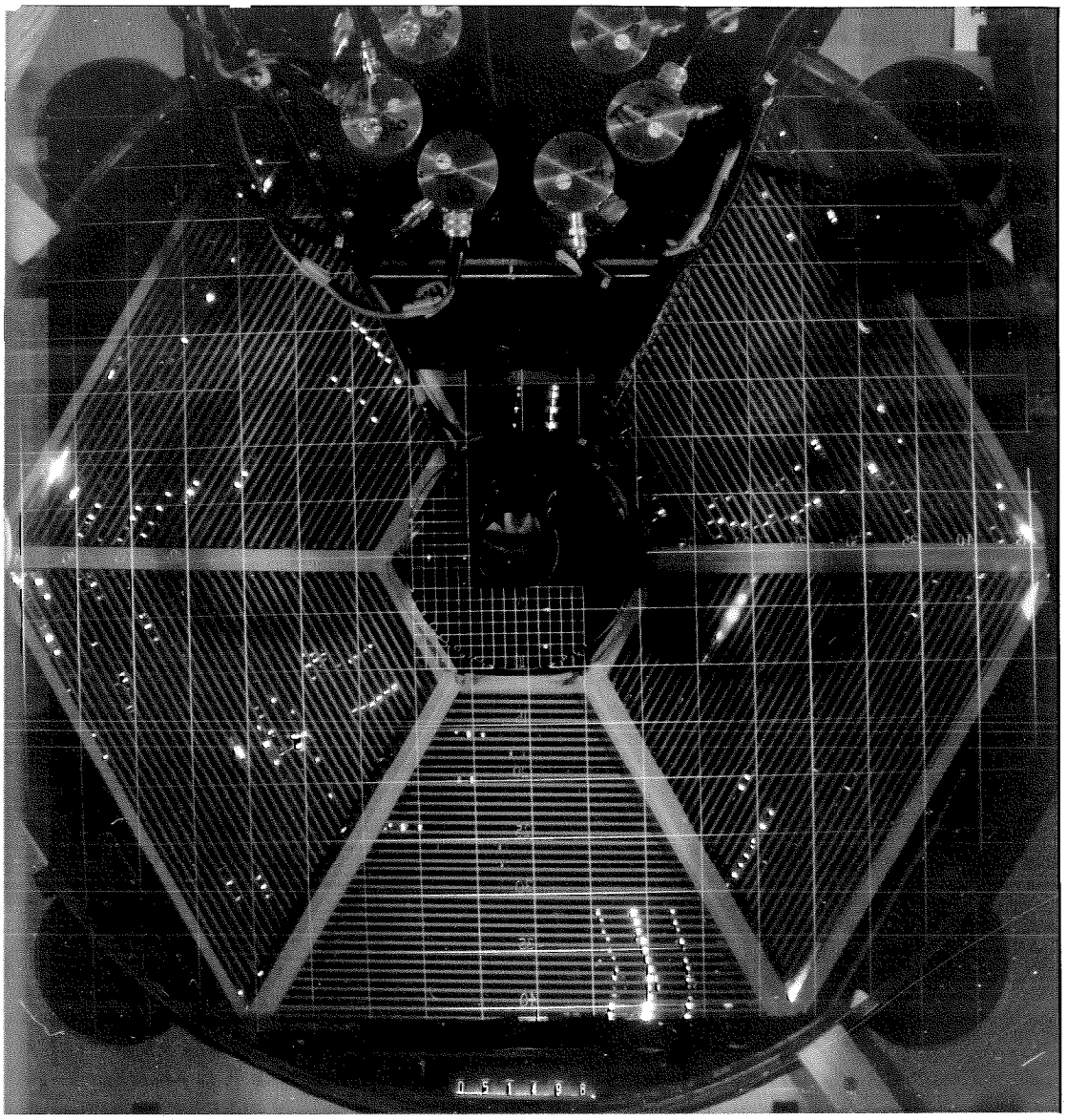

Figure 19

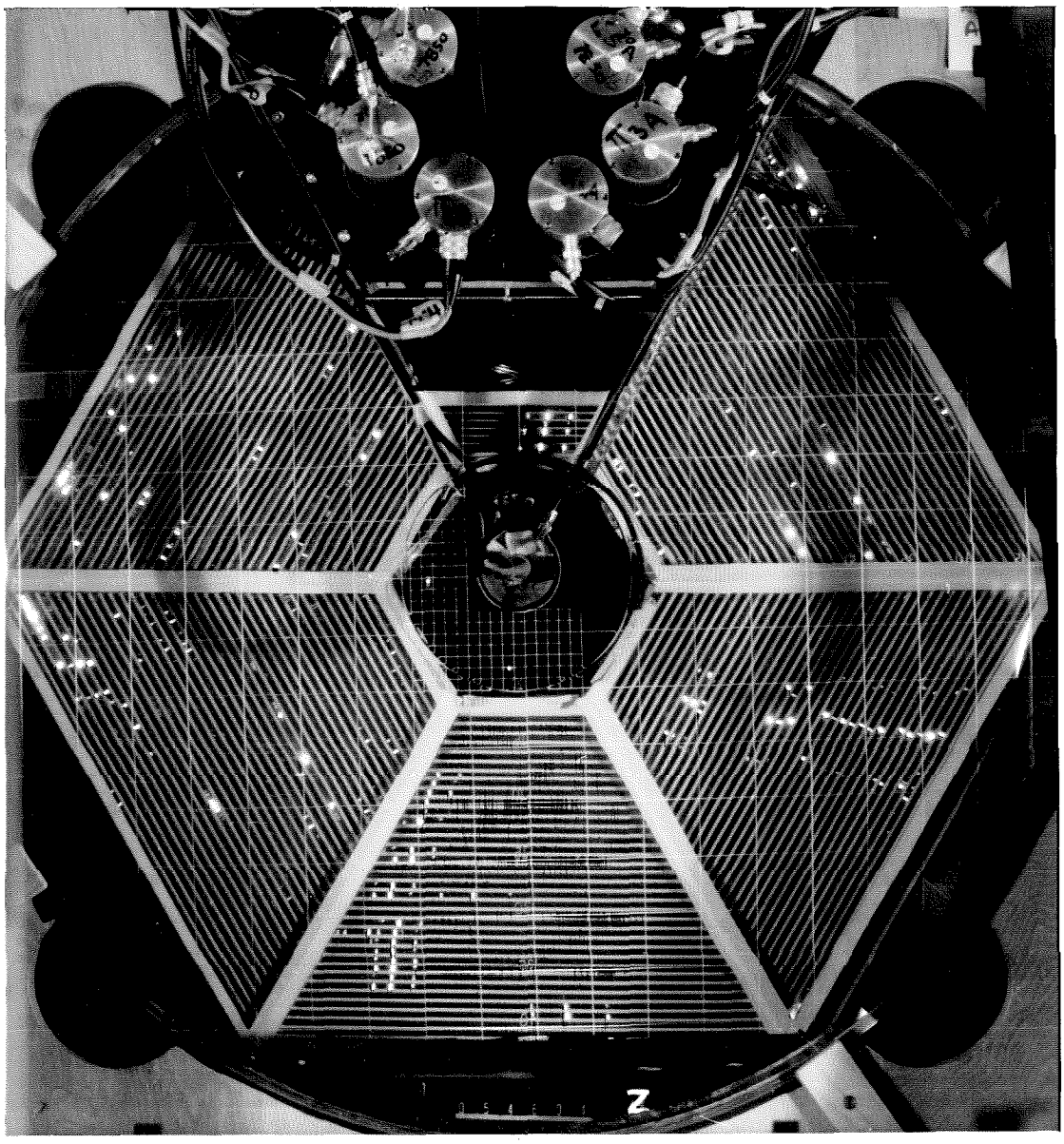

Figure 20

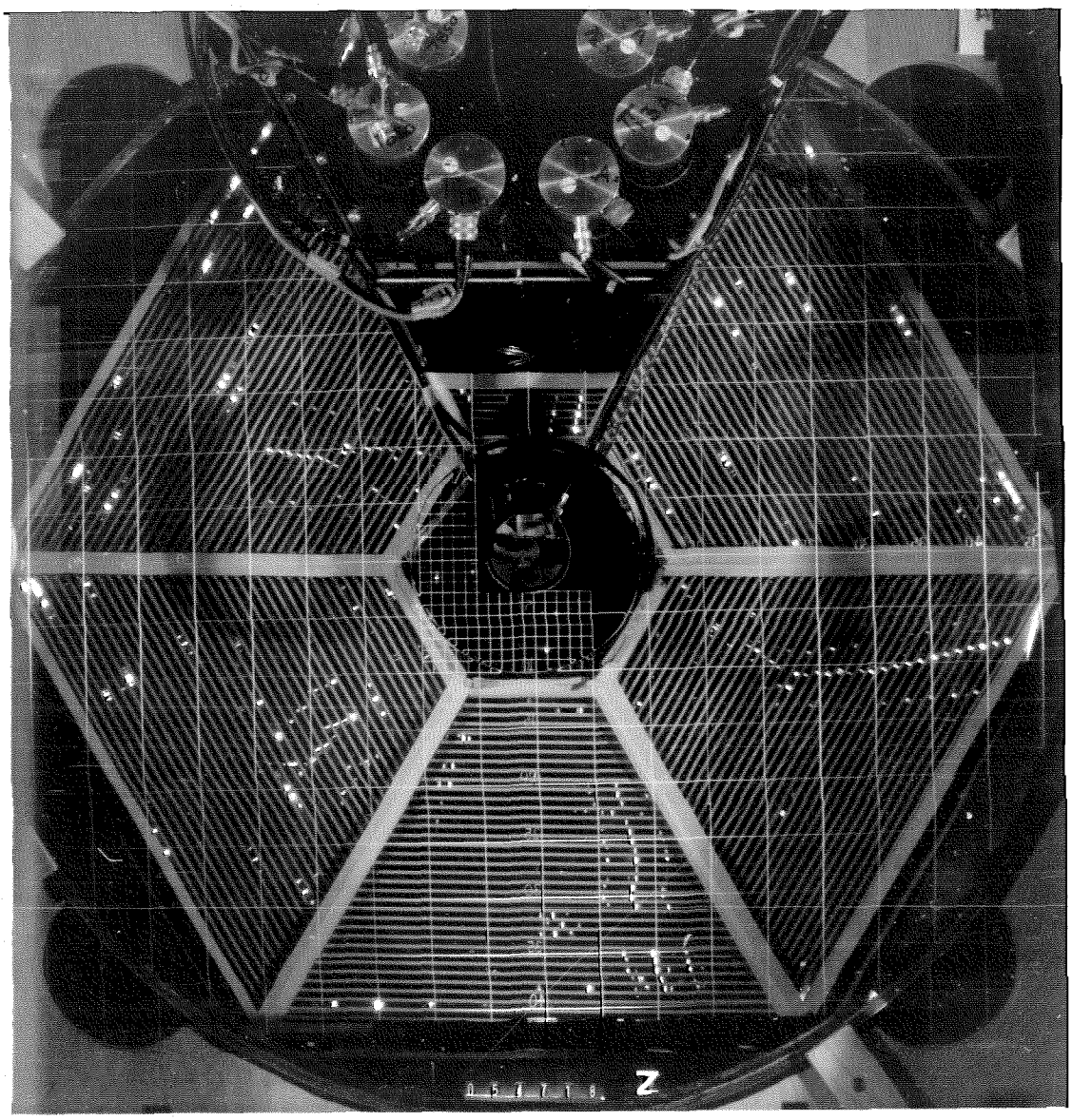

Figure 21

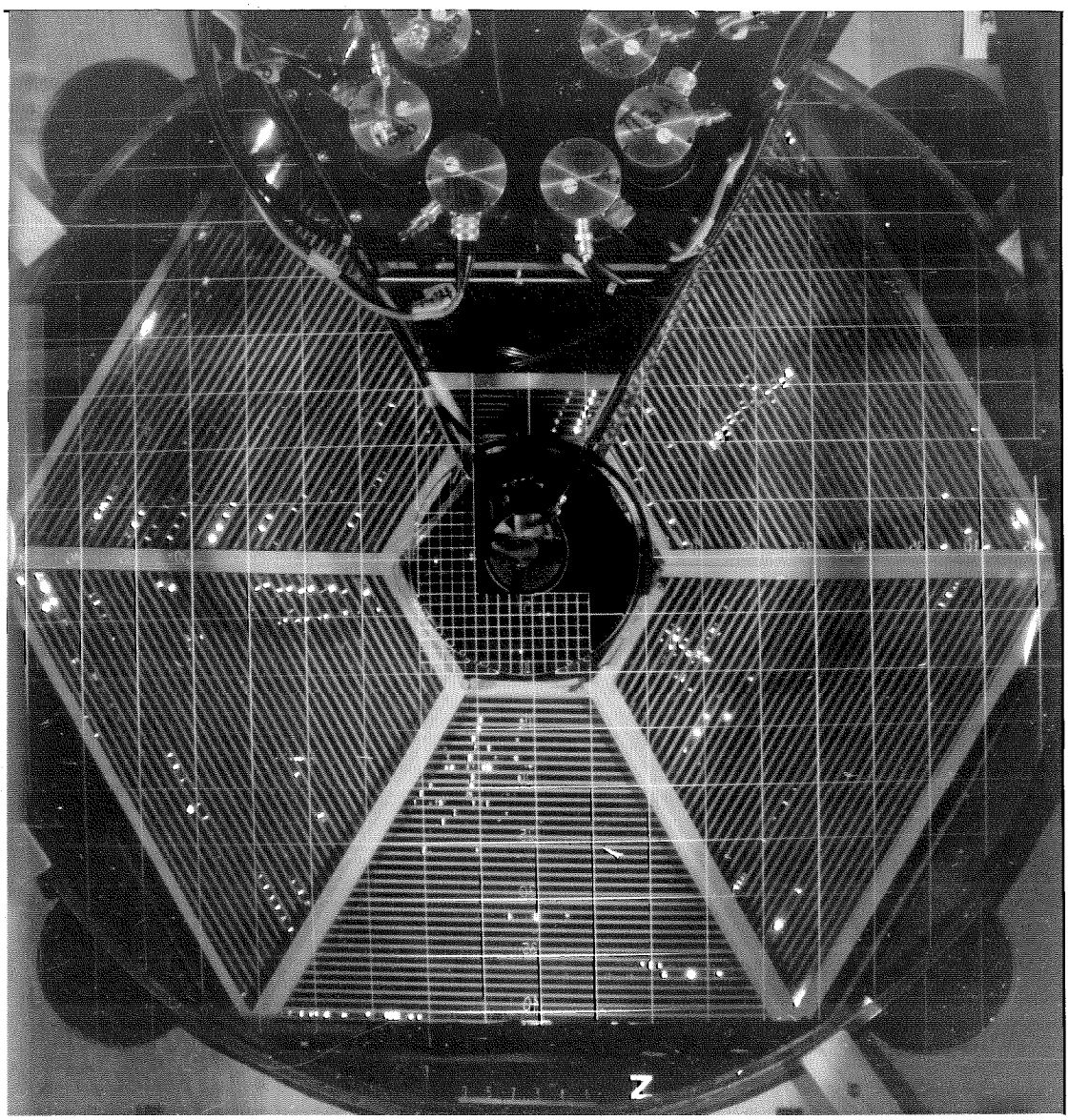

Figure 22

IV. CONCLUSIONS

The possible results of this experiment have been drastically compromised by the numerous difficulties encountered. The following list itemizes the major difficulties:

1. Because most of the running time was spent setting up and checking out the equipment, not enough time could be spent taking good data to insure good statistics. Only about three or four half days instead of twenty were spent taking "good" data.
2. The triggering rate was high enough to cause appreciable dead time (40%) and resulted in many pictures taken per good event. The π-μ gate seems to have been moved in close enough to the stopping pulse to trigger on any stopping pulse (except smaller pulses) whether or not there was a distinguishable second pulse.
3. The rate of accidental photons in the γ chambers was high; around 25% of the frames have one or more accidental photons. These result from the long sensitive time of the spark chambers, which were set for at least five μsec as required by $K_{\mu 3}$ experiment but probably were closer to ten μsec.
4. The μ pulse height was depressed on the scope display because of the nonlinear gain of amplifiers driving the CRT. This made the already small μ pulse difficult to

see and distinguish from noise, such as reflections, oscillations, and other wiggles that appeared on the trace, especially when the main pulse was large.

5. The K chamber had only one gap working during most of the useful running time, hence the direction of the K is not measured. With the K^+ direction lost the decay vertex location becomes more uncertain.

6. The depth measurement had large uncertainties because of the large factor relating distance between spark and reflections to the depth coordinate. When the π trajectory is extrapolated to the stopper over a distance three times the length of the trajectory sampled, the uncertainty in the z coordinate of the decay vertex is compounded to a large number.

7. The geometrical constants describing the location and orientation of the stopper, the K chamber and its mirrors, the orientation and depth calibrations of the γ chambers were not measured as precisely as would be desirable.

8. The cross section for inelastic scattering of π's from $K_{\pi 2}$ is high enough, such that, for the amount of material in the stopper and the wedge, one can account for nearly all of the 174 intermediate range π's seen. Inelastic scattering in the hodoscope is also a problem.

The difficulties mentioned in 3 and 8 mean that greater reliance must be made of kinematic fitting to reject false $K_{\pi_2\gamma}$ events. Unfortunately, pions from $K_{\pi 2}$ that scatter after the π chamber give rise to events that can readily fit $K_{\pi_2\gamma}$ kinematics, given some of the large errors (items 5, 6, and 7) in this experiment.

Much information of a somewhat imprecise nature is available from this experiment. In addition to the information required for identification of $K_{\pi_2\gamma}$ there is the pulse heigths of all the π counters, the "dE/dx" counter pulse height, and the FC-75 counter pulse. The showers in the γ chambers might yield useful information about the direction and energy of the photon independent of knowledge of the decay vertex. A number of these possibilities were investigated and analyzed with very limited success in overcoming the major short-comings of this experiment.

The results of this experiment can be presented as a series of upper limits of the branching ratio, arranged in order of the credibility of the evidence used. First, from the hodoscope alone, the short range π's with good π-μ decays and good π chamber tracks minus a lower limit on π^+ inelastic scattering yield a reasonably convincing upper limit of 1.8×10^{-3}. The π^+ spectrum for these events is similar to that of Cline and Fry, but which is also what could be expected from π^+ inelastic scattering. Second, requiring three γ's in the spark chamber does not improve the branching ratio much unless a lower limit on the number of $K_{\pi 2}$ with two γ's and an

accidental γ is obtained. Third, requiring good kinematic fits and pulse height fits does improve the result because only one or at best two events survive yielding an upper limit of $\sim 2 \times 10^{-4}$.

It is tempting to say that the one event satisfying all requirements including pulse height and kinematic fits is an example of $K_{\pi_2\gamma}$ where all products of the decay are seen. However, the chance for the most serious $K_{\pi 2}$ background to fit is large; Table VII shows that two or three of this type of background are expected to fit from the sample 174 $K_{\pi_2\gamma}$ candidates. This most serious background, a $K_{\pi 2}$ interaction after the π chamber that has one accidental γ, can be tested for by fitting the events to the $K_{\pi 2}$ hypothesis. When this is done for the event in question; when all the two γ combinations are tried, not one combination fits the $K_{\pi 2}$ kinematics. It may still be a $K_{\pi 2}$ that interacts after the π chamber, but one that has only one or zero γ's from $K_{\pi 2}$ and the rest accidentals. These two types of backgrounds have 15 to 20% chance to fit. Assuming that an appreciable fraction of 174 events, say 50, are $K_{\pi 2}$ interactions after the hodoscope, the event with two accidental γ's and one γ from $K_{\pi 2}$ is expected to fit the $K_{\pi_2\gamma}$ kinematics. Thus, there is still a good chance that the one event could be a background.

An interesting question to ask is would the experiment have worked had ten times as much data been collected. On the basis of the analysis on what was collected it is not likely unless the accidental problem is solved, or the measurement errors

significantly reduced. The sensitive time of the spark chambers could easily be reduced by a factor of 10, thereby reducing accidentals by the same factor. Considerable improvement in the measuring errors could be obtained if all K chamber gaps were made to work and the π chamber made shorter and put on top of the stopper. It would help to move the top γ chambers out a bit to avoid π's going through the chamber edges. With the extra room above the stopper a 90^{o} stero view of the shortened π chamber is feasible. It would be desirable to increase the lever arm on the π^{+} trajectory so as to decrease π^{+} angle errors by adding more gaps or by splitting the π chamber into two separated sets of gaps. It might be possible to reject a few more inelastic scatterings by removing material from the top of the stopper and making up for it with another scintillation counter.

For a small reduction on detection efficiency, the first few plates of the γ chambers could be removed and twice as large an angle used for the tilted mirrors, thereby improving γ depth measurement. Further improvement in the γ measurements would require 90^{o} stereo and the use of rectangular spark chambers.

APPENDIX I

TRIGGERING SCHEME

A. The K^+ Telescope

The K^+ beam design is best understood by referring to Figure 23 which shows the beam layout and Figure 3 which shows a side view of spark chambers, π hodoscope, and some of the K telescope in place. Secondary particles from a platinum target in the Berkeley Bevatron are focussed by Q_1, momentum analyzed by C_1 so that positively charged particles with a central momentum of 600 Mev/C are imaged on the Fitch counter, whose physical size sets $\Delta P/P$ (momentum window) at $\pm$ 5%. Protons which have now lost more energy than π's or K's in going through the Fitch counter are swept aside in C_2, while K's and π's enter the aperture of Q_2 and are focussed on the stopper. The amount of material in the beam is such that K's will stop in the stopper, while π's will go all the way through and protons which are not swept aside by C_2 will stop well before the stopper.

The fact that the ratio of K's to π's in the beam is approximately 1/100 is important to further consideration of the K^+ signature because in order to have less than 1% π contamination of the K^+ signatures, the scheme must accept most of the K's and reject more than 99.99% of the π's. The essential difference between π's and K's in the beam insofar as the triggering is concerned is a difference in velocity. This fact is made use of for each of the four counters in the K telescope.

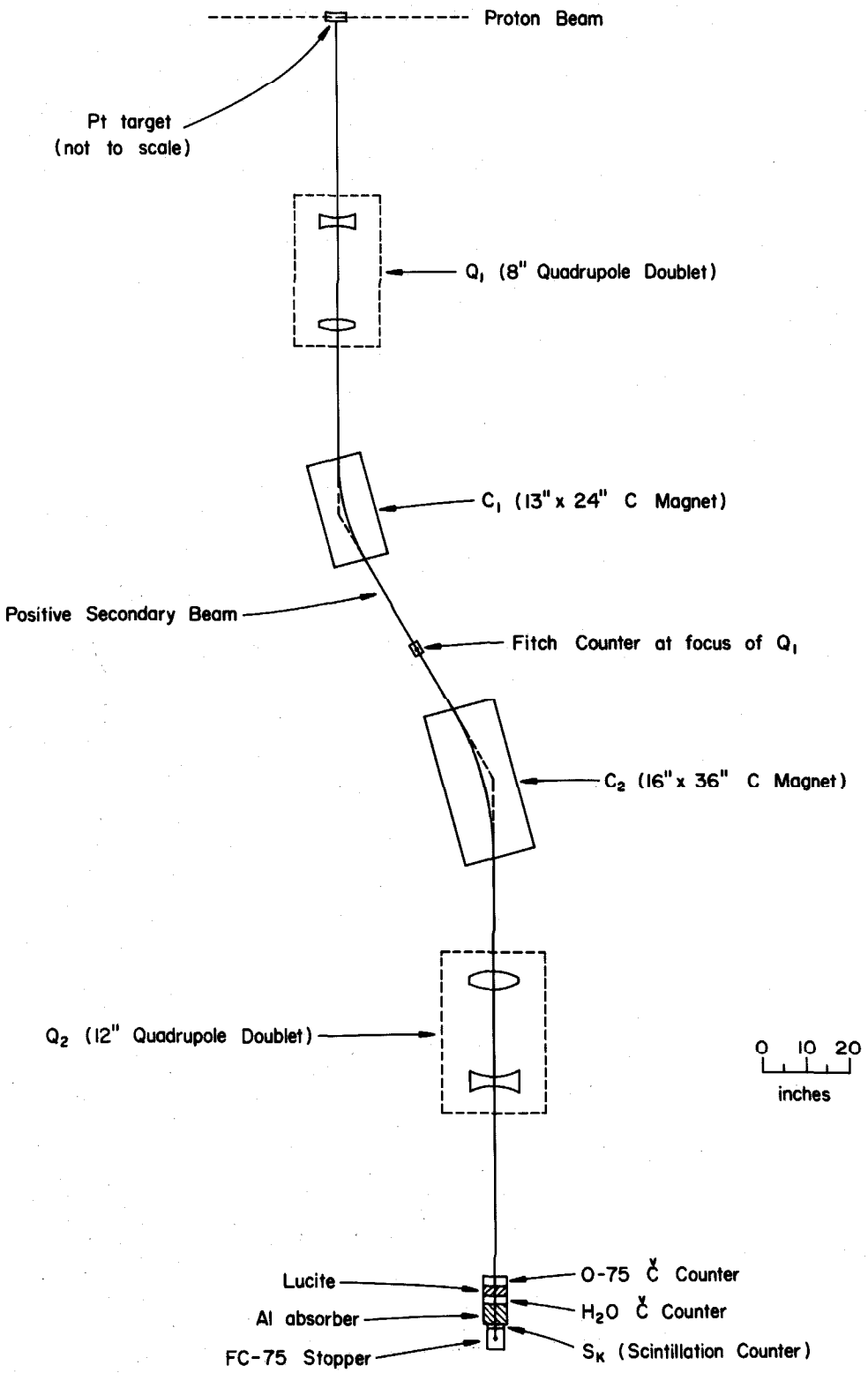
Proton Beam
Pt target
(not to scale)
Q_1 (8" Quadrupole Doublet)
C_1 (13" x 24" C Magnet)
Positive Secondary Beam
Fitch Counter at focus of Q_1
C_2 (16" x 36" C Magnet)
Q_2 (12" Quadrupole Doublet)
0 10 20
inches
Lucite
Al absorber
FC-75 Stopper
O-75 $\check{C}$ Counter
H_2O $\check{C}$ Counter
S_K (Scintillation Counter)

Figure 23

The Fitch counter whose construction is shown in Figure 24 makes use of the angular difference in the behavior of Cerenkov light from particles of different velocity. At the Fitch counter the velocities and the corresponding angles for Cerenkov radiation in lucite for the π's, K's, and P's in the beam are shown in the table below.

Particle	Central Velocity	C Angle	Max. Velocity	C Angle	Min. Velocity	C Angle
π	0.98	46.8	0.98	47.0	0.97	46.5
K	0.77	30.0	0.79	32.0	0.76	28.0
P	0.54	--	0.56	--	0.52	--

Some of the light from K's is transmitted through the downstream face of the lucite radiator. Light from π's, on the other hand, is at an angle greater than the critical angle of 41.9° for lucite and so is internally reflected causing most of it to be lost by absorption at the blackened upstream face of the radiator or to be transmitted out through the sides of the radiator. The Fitch counter then gives a pulse for K's and not for π's or for protons because protons are below the velocity threshold of 0.67 for making Cerenkov light.

The other Cerenkov counters in the telescope, namely, the 0-75 and the H_2O counters, operate as velocity threshold counters so as to give pulses for π's but not for K's or P's. The fourth counter, a scintillation counter labeled S_K (also called "dE/dx"), was placed next to the FC-75 stopper; by discriminating against

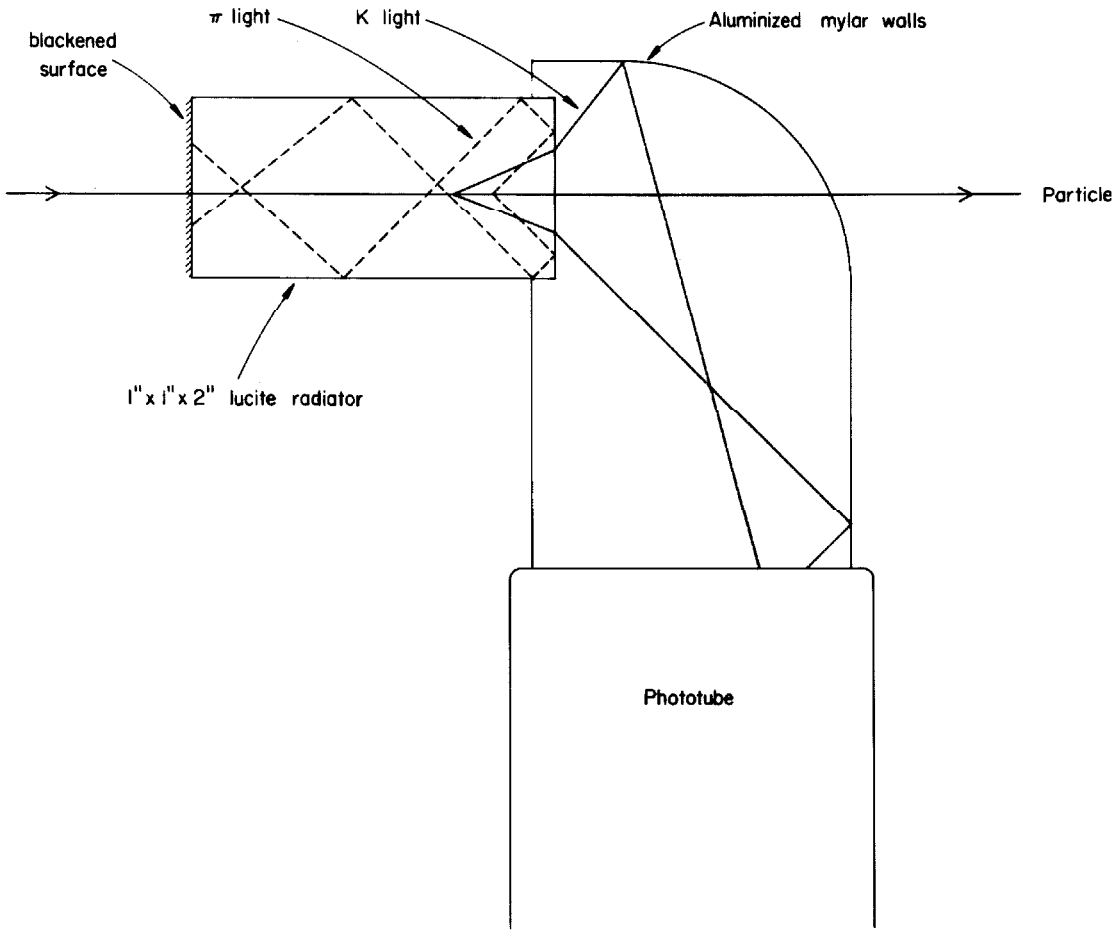

Fitch Counter

Figure 24

pulses from S_K that are less than three times minimum ionizing, a signal is obtained for K's but not for π's. Figure 25 is a plot of β versus residual range in the telescope for the various energy π's, K's and P's available. For each particle three curves are shown, one each for the maximum, the minimum and the central energies accepted by the system. The "velocity acceptance windows", i.e., the velocity regions which will produce pulses in the various counters, are also shown in Figure 25 and show graphically the requirements for a K signature. A particle entering the Fitch counter faces the equivalent of 77 grams/cm^2 of lucite; as it procedes through the system it slows down according to one of the curves shown. A pion will produce pulses in the 0-75 and H_2O counters and also the FC-75 stopper but not in the S_K or the Fitch counters; a kaon activates the Fitch and S_K counters but not the others and a photon will not activate any of the counters.

The K telescope electronic logic is shown schematically in the diagram of Figure 26. The Fitch counter is delayed with respect to the rest of the telescope by the amount needed to compensate for the time of flight of K's. The Fitch flux is defined by a coincidence between delayed signals from Fitch and S_K set for the K time of flight and in anti-coincidence with a slightly earlier Fitch signal and a slightly later S_K signal. The veto's insure that no signal is generated if another particle comes in just before or just after the K. The π flux is determined by a coincidence with 0-75, H_2O and S_K. The final K signal requires coincidence of the Fitch flux with

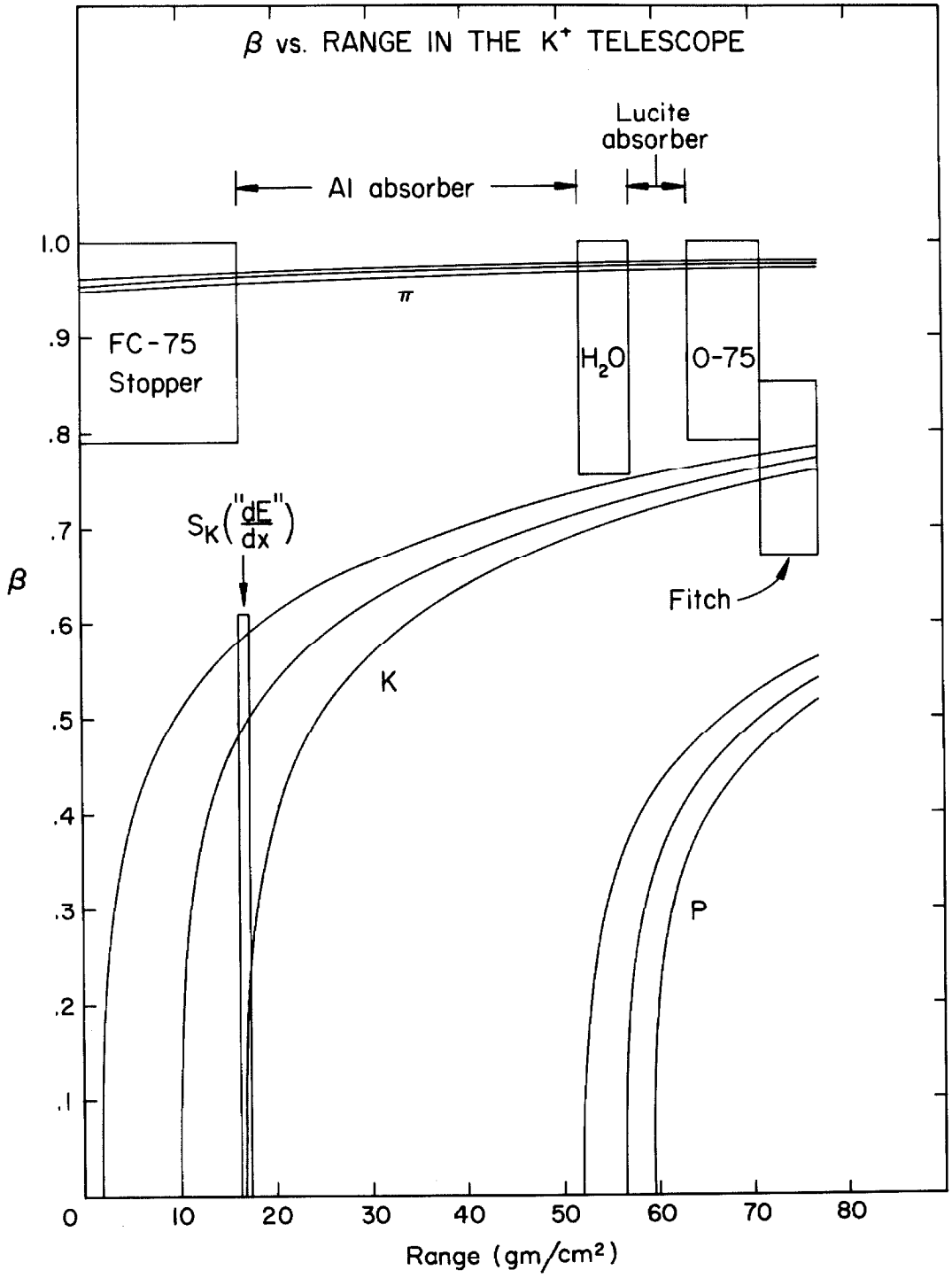
β vs. RANGE IN THE K⁺ TELESCOPE
Lucite absorber
Al absorber
1.0
.9
.8
.7
.6
.5
.4
.3
.2
.1
β
π
FC-75 Stopper
H₂O
O-75
Fitch
K
P
Sₖ("dE/dx")
0
10
20
30
40
50
60
70
80
Range (gm/cm²)

Figure 25

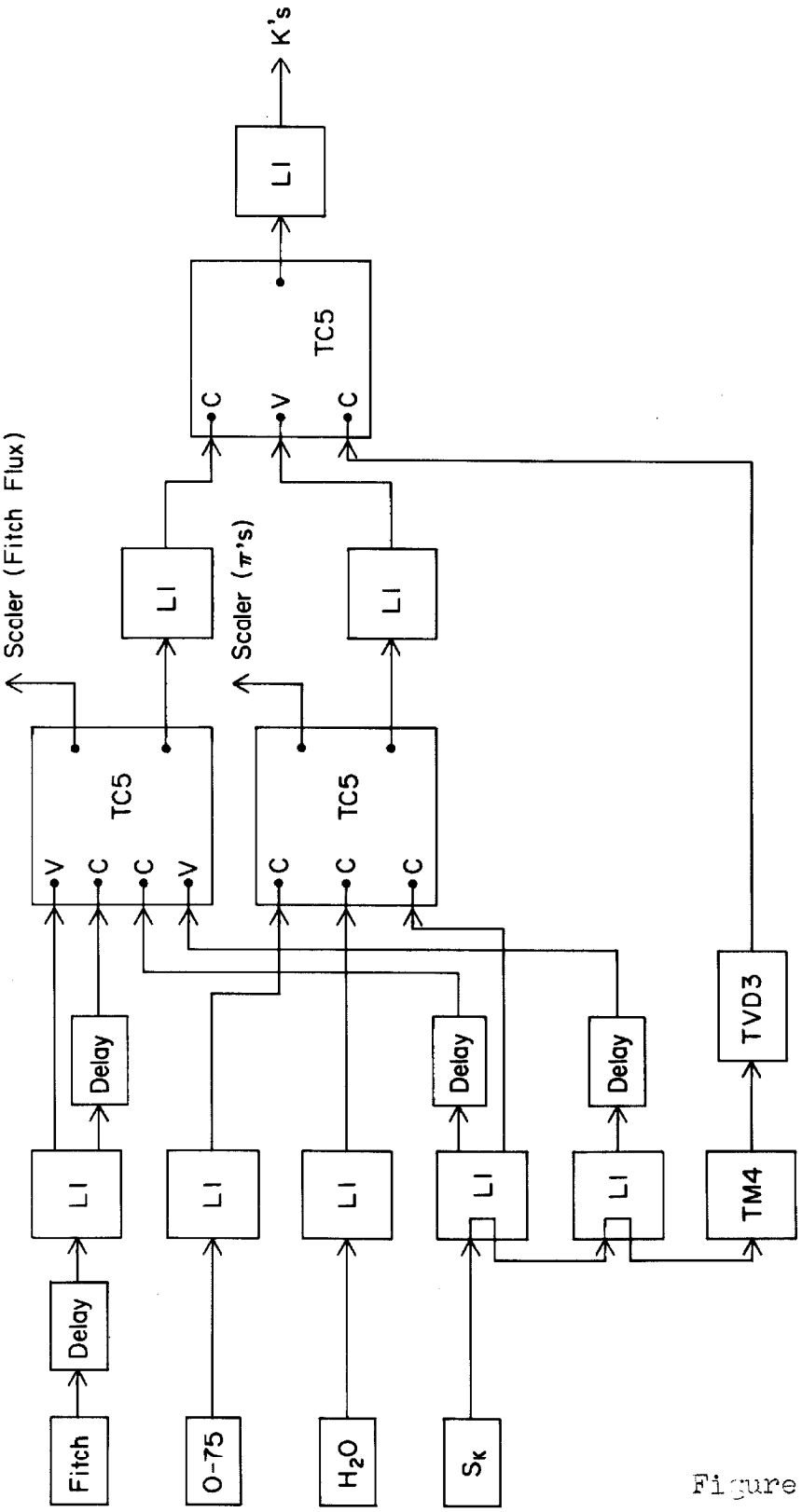

K⁺ Telescope Electronic Logic

Figure 26

signals from S_K, which pass through the discriminator set to discriminate against minimum ionizing π's, and an anti-coincidence with the π flux.

The electronics used in the experiment, some of which is shown in the schematics of Figure 26, were designed by Professor Tollestrup in collaboration with Dr. Ricardo Gomez. The electronics were designed as transistorized modules with connections on the front and are discussed elsewhere in detail (22). The L1 is a limiter used to produce standard shape pulses for use with the TC5, a coincidence-veto circuit. The TM4 is a multiplexer, while the TVD3 is a fast voltage discriminator.

In brief, a clean K^+ signature was obtained by use of velocity selection based on time of flight of the K's, on velocity thresholds for Cerenkov radiation in H_2O, 0-75 and Fitch counters, on the angular dependence of Cerenkov light with velocity in the Fitch counter and finally on ionization differences in the S_K counter.

B. The π^+ Hodoscope and $K_{\pi_2\gamma}$ Triggers

It is the function of the π^+ hodoscope and its associated electronics to detect those short range π's from K decays that produce a π-μ decay in one of the hodoscope counters. Basically this was accomplished by requiring the electronics to detect a particle which enters the hodoscope within a few K^+ lifetimes from the time the K stops and is detected in the K telescope, which stops in channel 1 through 6 of the hodoscope, and which produces a second pulse within a few π lifetimes of the time the π stops in the

stopping counter. The manner in which this was accomplished is best understood by referring to Figures 2 and 3 which show the geometry of the hodoscope counters and Figures 27 and 28 which schematically show the electronic logic of the π hodoscope and the $K_{\pi_2\gamma}$ triggering scheme.

The π_n signals are simply the sum of signals from the A and B counters of the n-th channel. This is shown in the first part of Figure 28. By referring to Figure 27 ones sees that the K signal from the K telescope electronics turns on a 35 n. s. wide gate by activating a TVD3. Requiring this signal to be in coincidence with π_1 insures that the π signal occurs within about three K lifetimes of the time the K^+ stopped. A signal satisfying the above requirements is designated K_{S+L} where the subscripts S and L refer to the fact that both slow and fast π's from K decays satisfy these requirements. An FC-75 pulse occurs for particles with β greater than 0.79 originating in the FC-75 stopper; thus, the K_S (slow or short range π's from K decays) signals are defined by K_{S+L} in anti-coincidence with FC-75, while K_L (fast or long range π's from K decays) signals are defined by K_{S+L} in coincidence with FC-75. The K_{S+L} signal turns on 100 n. s. wide gate which is used for detecting π-μ decays.

Figure 28 shows the rest of the $K_{\pi_2\gamma}$ logic. The μ_n signal which should occur when there is a π-μ decay in the n-th channel is defined by a coincidence of π_n signal from the fast L2 limiter with the slightly delayed μ gate which is turned on by K_{S+L} signal. The chronology of the pulses for μ_n is schematically shown below:

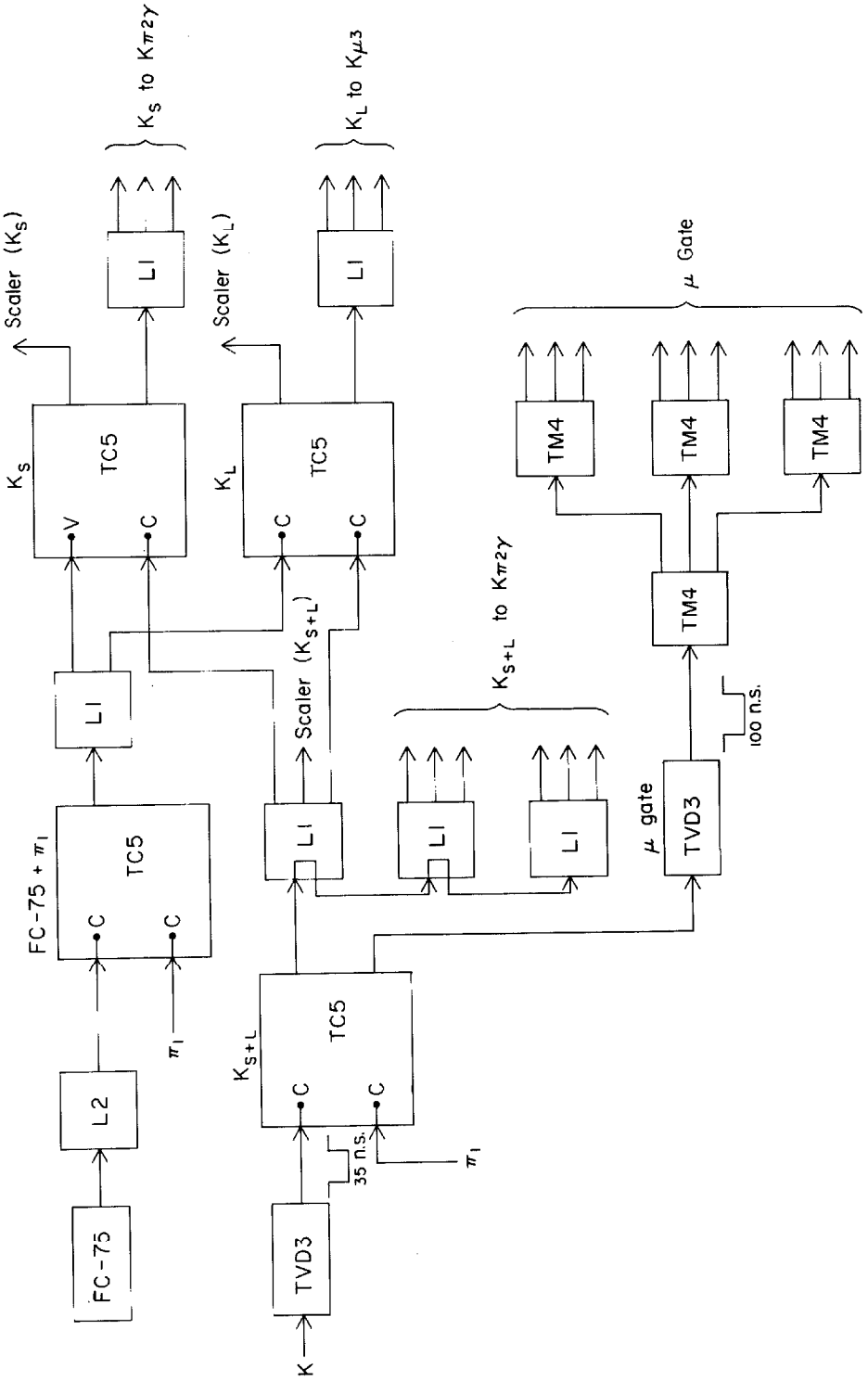

Figure 27

Electronics Common to Kμ3 and Kπ2γ

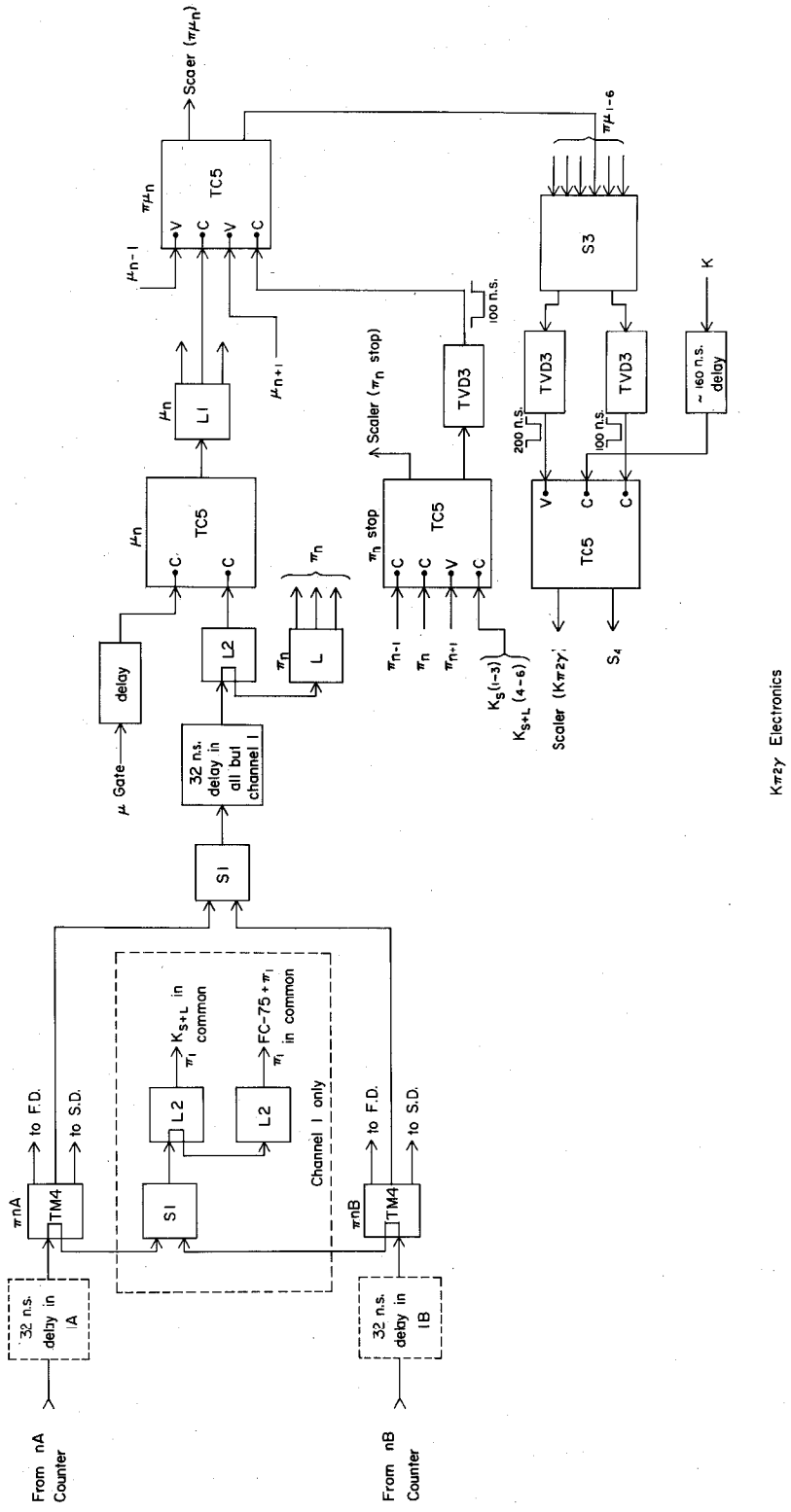
From nA Counter
From nB Counter
32 n.s. delay in 1A
32 n.s. delay in 1B
πnA
πnB
TM4
to F.D.
to S.D.
S1
L2
Channel I only
Kπ2y Electronics

Figure 28

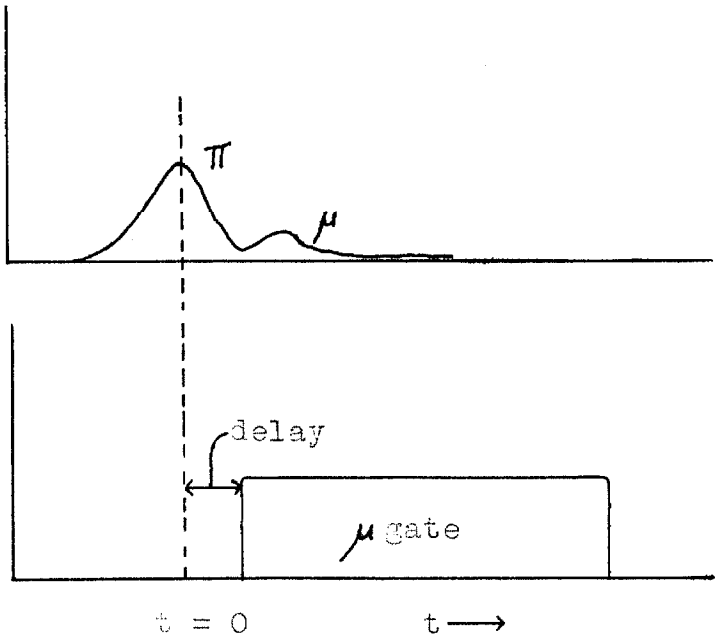

The π_n stop signal requires a π_{n-1} signal in coincidence with π_n and K_S for channels 1 through 3 or K_{S+L} for channels 4 through 6, but an anti-coincidence with π_{n+1}. The $\pi\mu_n$ signal, which should be generated when a π-μ decay occurs in the n-th channel, is defined by the μ_n signal in coincidence with a 100 n. s. wide pulse turned on by a π_n stop signal and in anti-coincidence with μ_{n-1} and μ_{n+1} signals.

All six $\pi\mu_n$ channels are added in S3 whose two outputs are sent to TVD3's. One TVD3 is set to discriminate against pulses smaller than those obtained for just one $\pi\mu_n$ pulse coming into S3; when an event occurs that activates two or more $\pi\mu_n$ channels the TVD3 gets a pulse larger than the discriminator bias setting, hence one TVD3 puts out a 200 n. s. wide pulse.

The other TVD3 is set at a lower bias and produces a 100 n. s. wide pulse when one or more $\pi\mu_n$ channels produce pulses. The final $K_{\pi_2\gamma}$ trigger is generated by a delayed K signal in coincidence with 100 n. s. wide pulse from the TVD3 with the lower bias and in anti-coincidence with the 200 n. s. wide pulse from the TVD3 with the higher bias. The $K_{\pi_2\gamma}$ trigger is sent to activate circuit S4 which in turn triggers the spark chamber, the oscilloscopes and the camera advance.

A number of signals for monitoring purposes were fed into 10 megacycle scalers. They were the K_S, K_L, K_{S+L}, $\pi\mu_n$, and $K_{\pi_2\gamma}$ signals. The electronic noise generated when the spark chambers fired was picked up by some of the scalers and hence reduced the quality of information available from the scalers. Electronic calibration runs where the spark chambers did not fire were made periodically to get counts free of spark chamber noise pickup.

APPENDIX II

DISPLAY SCANS

A. Slow Display Scan

Pulses from all of the scintillation counters of the π hodoscope and from the additional scintillation counters of the $K_{\mu 3}$ experiment were displayed on a double beam oscilloscope set for a 4 or 5 μsec sweep time. This display served two purposes: (a) to separate the $K_{\pi_2 \gamma}$ and $K_{\mu 3}$ triggers, and (b) to show which counters the electron, from the decay of μ's stopping in the precessor, went through and the time delay before the stopping μ decayed. The first consideration is relevant to the $K_{\pi_2 \gamma}$ experiment while the second is of interest only to the $K_{\mu 3}$ experiment.

The pattern that would be seen on the slow display from pulses originating at the same time in all the counters is shown in the sketch below:

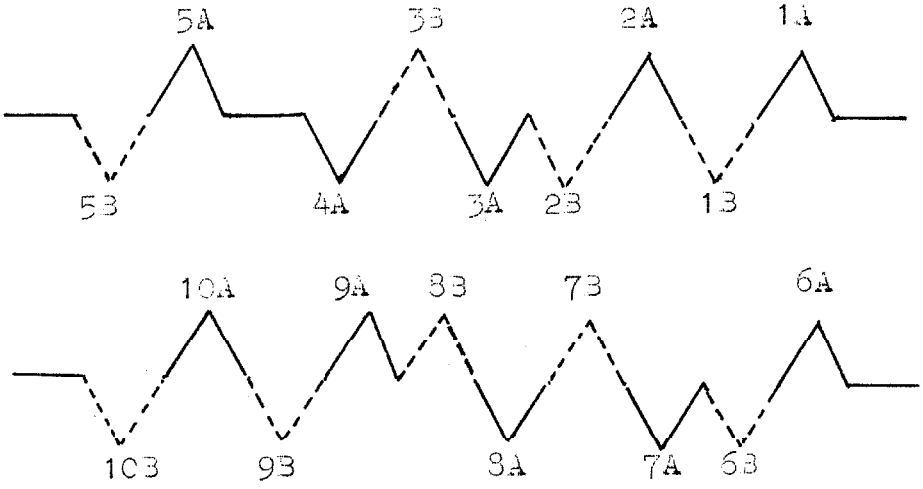

A sample photograph for an event stopping in counter 5A is shown in Figure 29.

The criterion for a $K_{\pi_2\gamma}$ candidate was that the pattern starting at t = 0 on the left show no pulse from channels 7 through 10 and that it show pulses only from channels 1 through 6. A $K_{\mu 3}$ event typically shows two pulses at t = 0 either from channels 7 and 8 or channels 9 and 10 depending upon what direction the electron went from the μ decay in the precessor. Preceding these two pulses in time, i.e., to the right in the photographs, would be a pattern showing a particle going through channels 1 through 8. Thus, the event in Figure 29 is a $K_{\pi_2\gamma}$ trigger. The pulse pattern for both types of events, information about accidentals, and for $K_{\mu 3}$ trigger, the delay between the electron and the stopping μ and delays of certain accidentals are coded and punched onto IBM cards with one card for each event. The cards could then be managed conveniently with card handling equipment to sort, classify and summarize data.

B. The Fast Display Scan

Essential to the $K_{\pi_2\gamma}$ experiment was the capability of observing the π-μ decay for a positive identification of the stopping π^+ and of making a measurement of the energy lost by the π^+ in the stopping counter. Also important was a method to verify that the logic for the K^+ signature had been fulfilled for any event of interest. To achieve these ends pulses from the π hodoscope counters, channels 1 through 6, as well as the dE/dx counter, Fitch and FC-75 counter of the K^+ telescope were displayed on a four beam fast oscilloscope

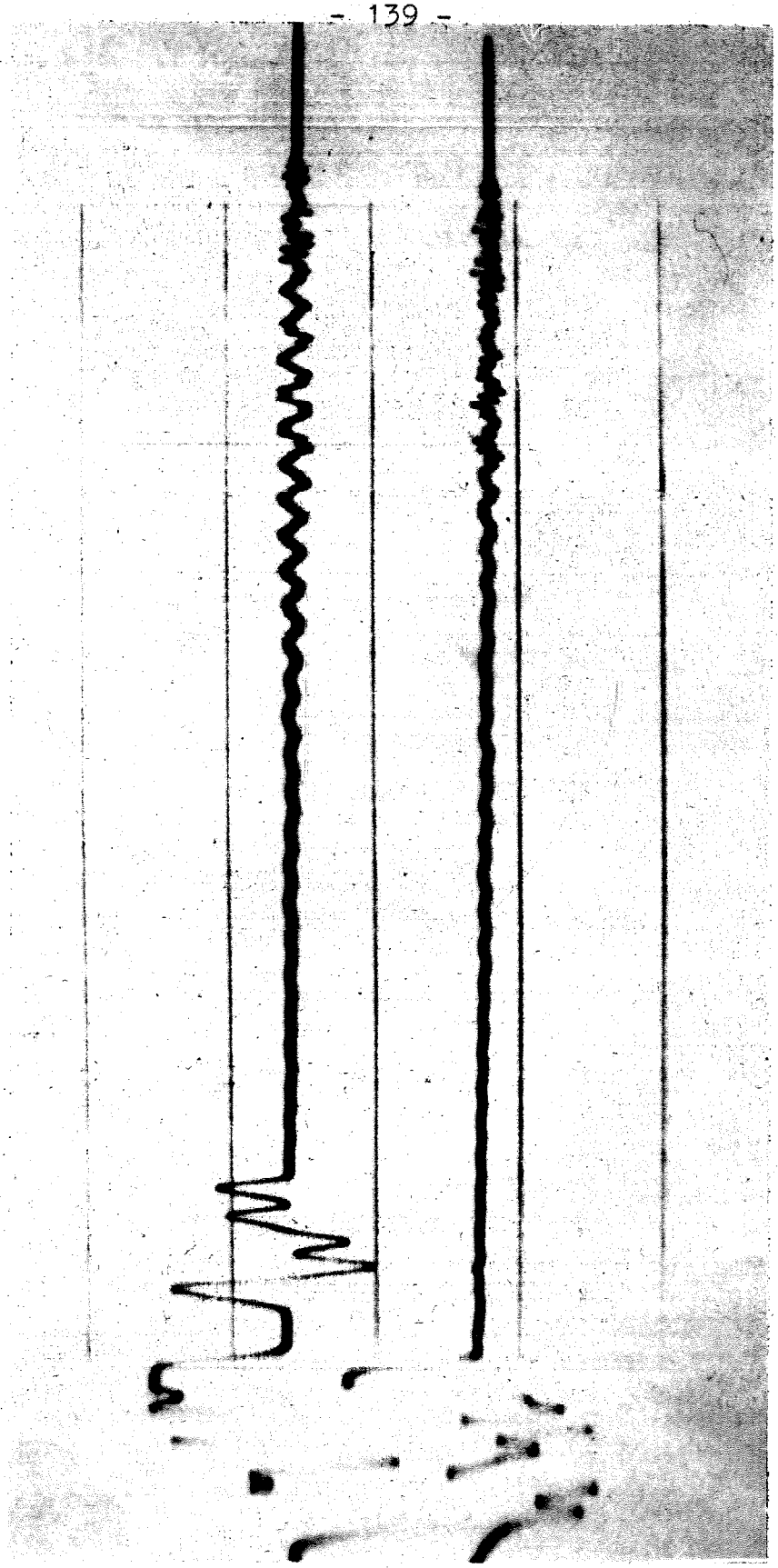

FIGURE 29

with a sweep speed of 30 ns/cm. Here, as with the slow display, the pattern of pulses identified which counters were activated. A sketch of the pattern that would be seen by pulses originating simultaneously from all counters is shown below.

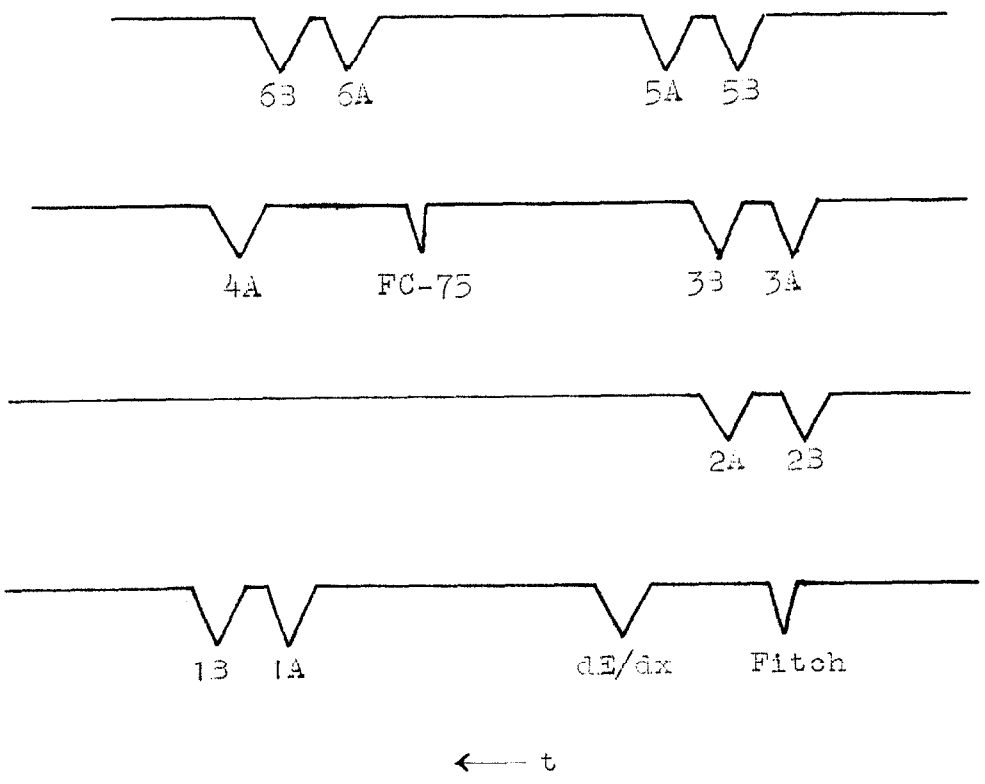

A sample photograph showing a $K_{\pi_2\gamma}$ trigger where the particle stopped in counter 5A is shown in Figure 30. The hodoscope counter pattern is delayed from the pattern above by the amount of time it took the K^+ to decay.

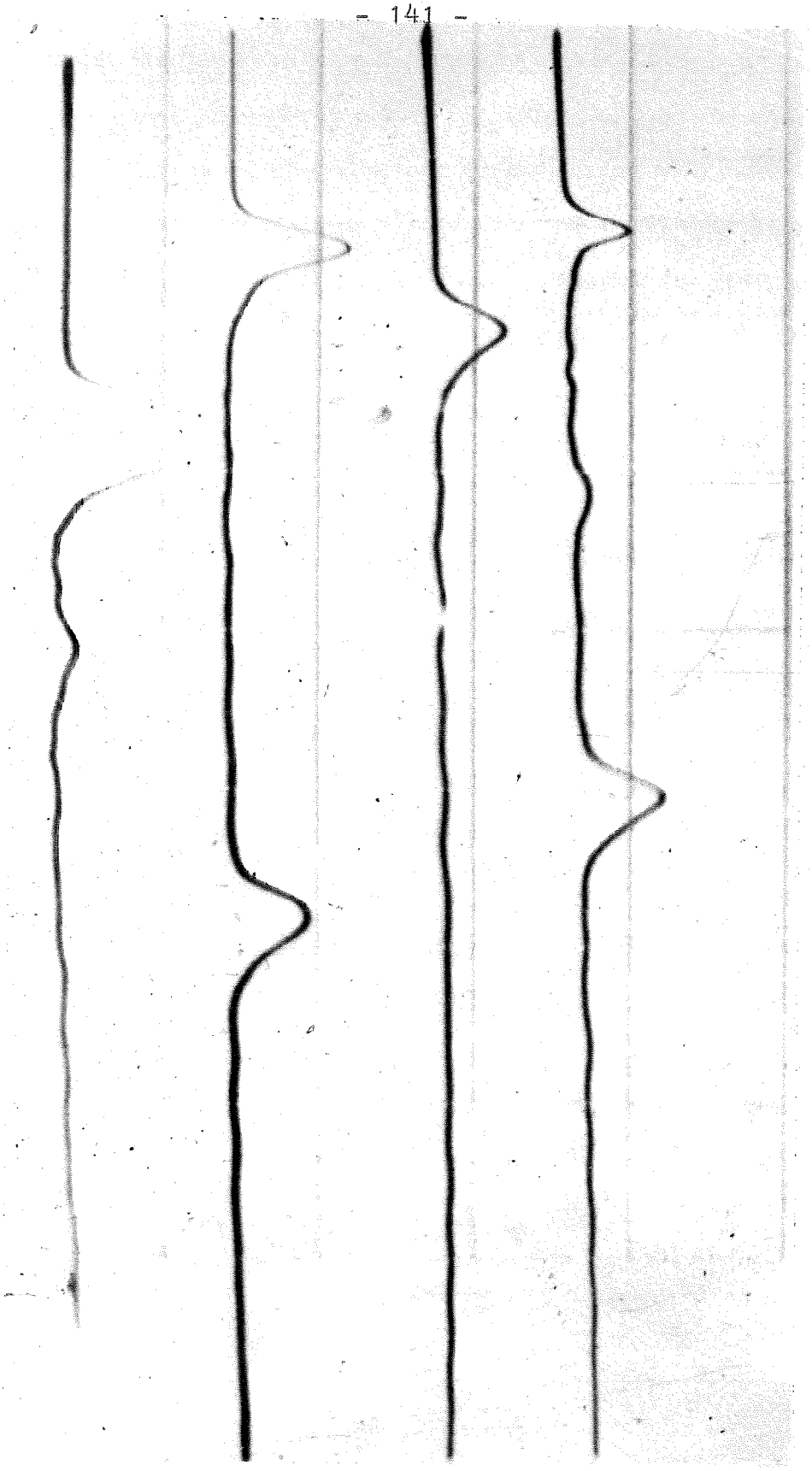

FIGURE 30

The fast display scan was designed to extract as much information as was possible to obtain from the photographs and get it onto IBM cards which could then be processed with data handling equipment. Only those events selected as $K_{\pi_2\gamma}$ triggers on the basis of the slow display scan were utilized in the fast display scan. The $K_{\mu 3}$ events seldom had a prompt enough μ decay to show up on the fast display.

The fast display scan consisted of identifying, from the pulse pattern, those counters which gave pulses, of measuring all pulse heights and the Fitch to dE/dx counter delay and the Fitch to 1A or 1B counter delay, and of searching for possible π-μ decays in the stopping counter. If a π-μ candidate was observed, the μ pulse height and the peak to peak delay of the π to μ pulses were also measured. To insure that the events selected for the fast display scan were $K_{\pi_2\gamma}$ triggers, the Fitch pulse was required to be fixed in time with respect to the oscilloscope trigger. For $K_{\pi_2\gamma}$ triggers the oscilloscope trigger timing was determined by the K telescope signal, whereas for a $K_{\mu 3}$ trigger the oscilloscope trigger timing was determined by the decay electron signal. The sketch below shows how the pulse heights and delays were measured. The measurements were made with graph paper templates while the display was projected onto a table screen.

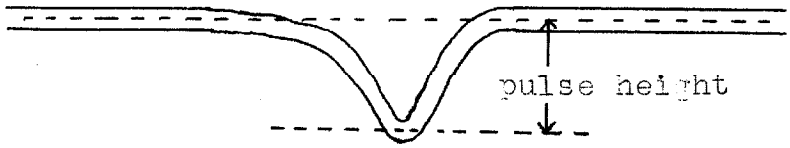
pulse height

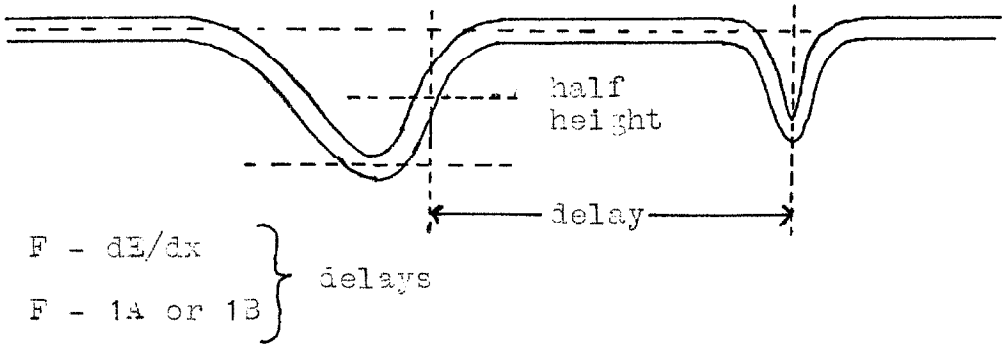
half
height
delay
F - dE/dx
F - 1A or 1B
delays

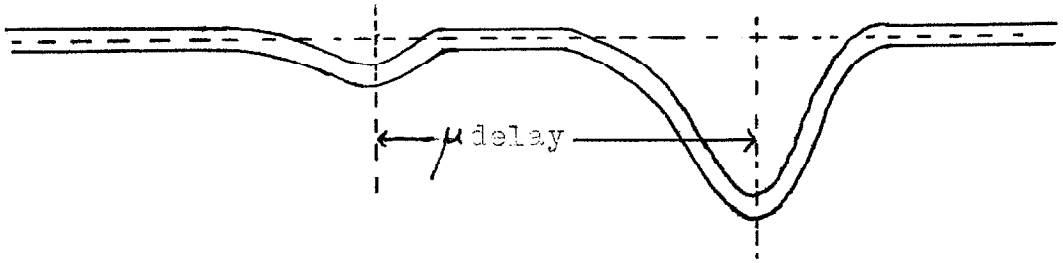
μ delay

A remark was coded for those μ candidates that were close to the π pulses. The three situations are sketched below:

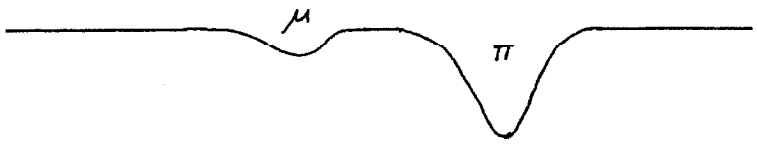

Normal

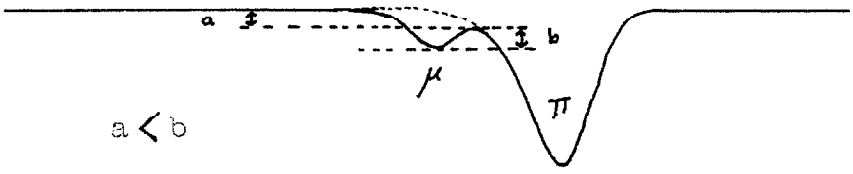

Riding Low

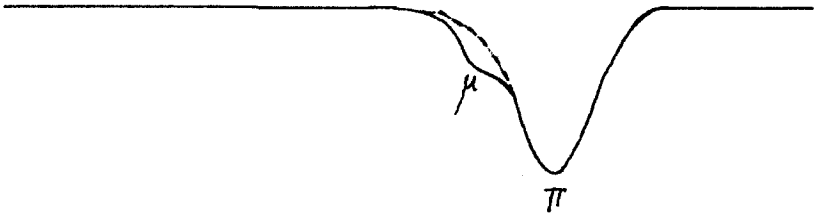

Riding High

The remark also noted if there were two or more μ candidates. The existence of accidental pulses not fitting a stopping particle pattern were acknowledged by recording the number of accidentals appearing on each of the four traces of the display.

The pulse heights, delays, and remarks along with the frame number and other indexing information was punched onto an IBM card for each event. The raw data on these cards was processed by 7090 program which corrected the data for the nonlinearities in the gain and sweep speed of the recording system. A new card was punched with delays in n.s. and pulse heights in terms of photo-multiplier output volts normalized to minimum ionization for each counter. For each event a graphical display was printed of the normalized pulse heights for each succeeding counter. The graph could quickly be compared with a template showing the Bragg curve for normal stopping π's or protons. In this way gross anomalies in energy loss characteristics, for example, from an interaction, could be spotted quickly. A sample graph is shown below; where the ordinate is pulse height and the abscissa is counter number.

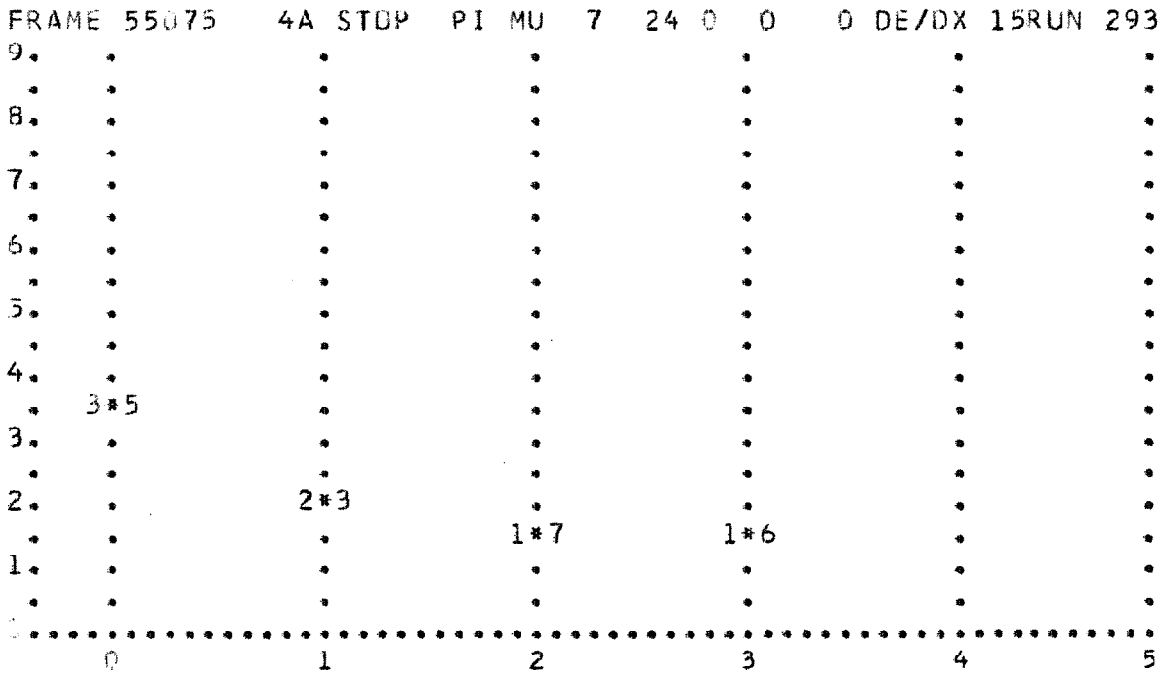

Counters are numbered backwards along the π trajectory with the stopping counter labeled 0. The heading contains the frame number, the stopping counter designation, the pulse height and delay and remarks for the μ candidate, if any, the dE/dx counter pulse height and the run number.

APPENDIX III

CALIBRATIONS

A. Fast Display Pulse Height Calibration

The pulses from the photomultipliers that eventually are displayed on the fast display are first multiplexed by the TM4 circuit then sent to an adder (TS-1) to be mixed. After the adder the pulses go through a chain of four Hewlett-Packard Model 460B Amplifiers the last two of which operated in the pulse mode, then to the input of the special four beam CRT of the modified Tektronic 517 oscilloscope used for the fast display. The amplifiers used in the pulse mode are not linear over their entire range. In order to use the pulse height information available from the fast display it is necessary to have (a) gain curves relating oscilloscope displacement to input voltage at the point in the systems where the photomultipliers are connected and (b) one point relating the photomultiplier voltage pulse height to the energy lost or light output in a counter.

The overall gain curves for each counter were obtained by multiplying two gain curves, one being the gain curve for the oscilloscope trace and the other being the gain curve of the electronics from the multiplexer input to output of the last amplifier stage. Each gain curve was obtained by putting in a known amplitude voltage pulse from an SKL pulser and measuring the output amplitude either on a linear oscilloscope for the electronics gain or measuring the oscilloscope displacement on film for the oscilloscope gain. A typical overall gain curve is that for counter 4A shown in Figure 31.

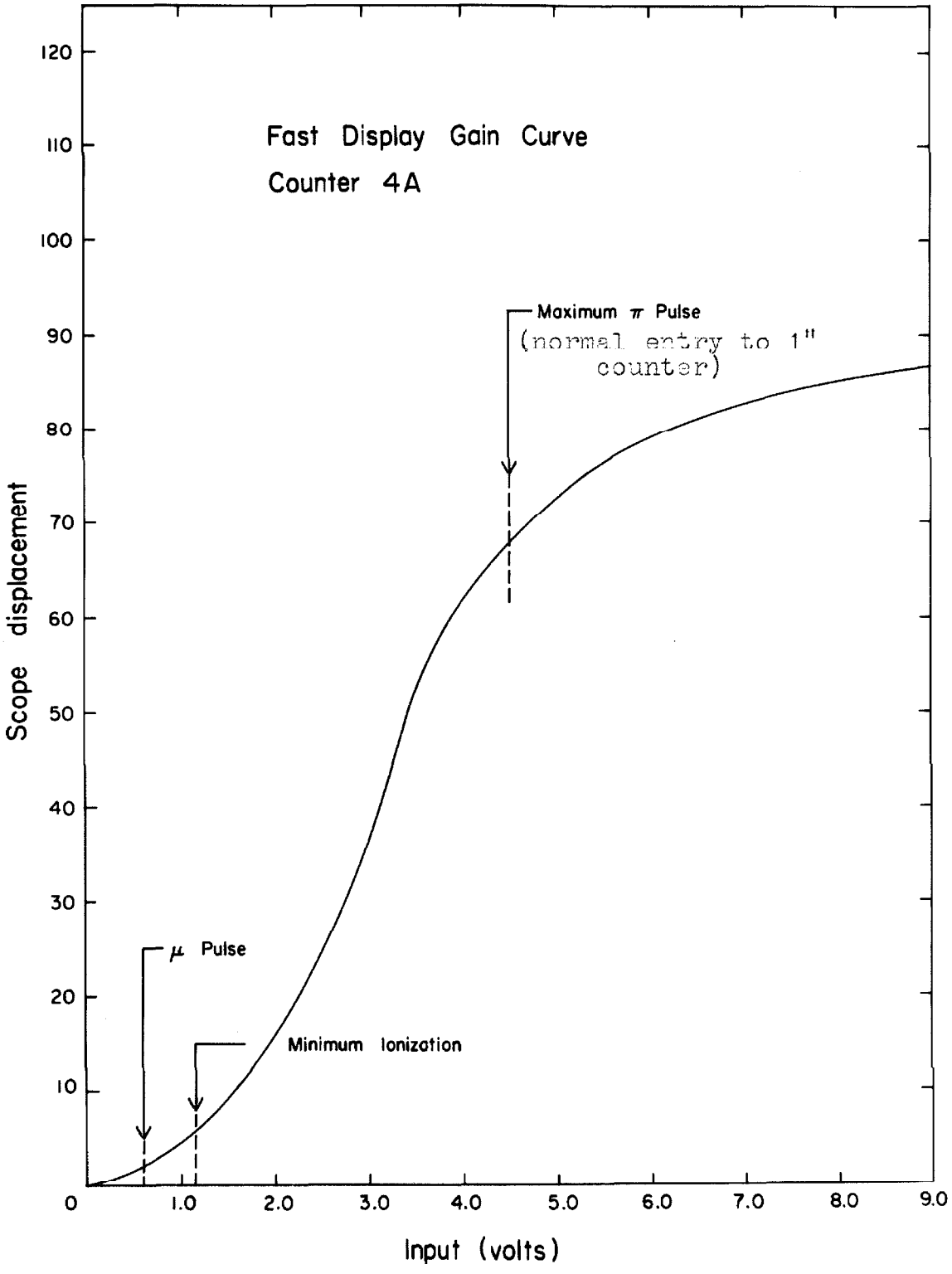
Fast Display Gain Curve
Counter 4A
Maximum π Pulse
(normal entry to 1" counter)
μ Pulse
Minimum Ionization
Scope displacement
Input (volts)
0
10
20
30
40
50
60
70
80
90
100
110
120
1.0
2.0
3.0
4.0
5.0
6.0
7.0
8.0
9.0

Figure 31

The calibrating point relating the photomultiplier voltage to light output in a counter was chosen to be the point given by a minimum ionizing particle. As a source of nearly minimum ionizing particles one has the μ's from $K_{\mu 2}$ decays. Certain runs described in the text as $K_{\mu 2}$ runs were used for this purpose. One plots the pulse height (photomultiplier pulse height) spectrum of these μ's for each counter and computes the average of the distribution. The light output for an average μ going through the counter in question can be obtained from standard curves relating dL/dx to residual range (23). All counters in the π hodoscope were calibrated in this manner. The pulse height spectra used for counters 1A, 6A, 3B are shown in Figure 32.

Because of the limited number of calibration events, only about 150 pulse heights for each counter are available for calibracting purposes. This is sufficient for computing a good average, although it doesn't provide detailed information on the shape of the spectra. The widths of the distributions are larger than normally encountered for scintillation counters one inch thick. A prototype counter, which was tested with a well calibrated beam of 500 MeV electrons confined to a one inch square in the center of a counter 1 inch x 6 inches x 18 inches, showed a half width of about 15%. Additional fluctuations for the μ event can come from:

1. Measuring error on the projection table which was about 10% for the small pulses encountered.

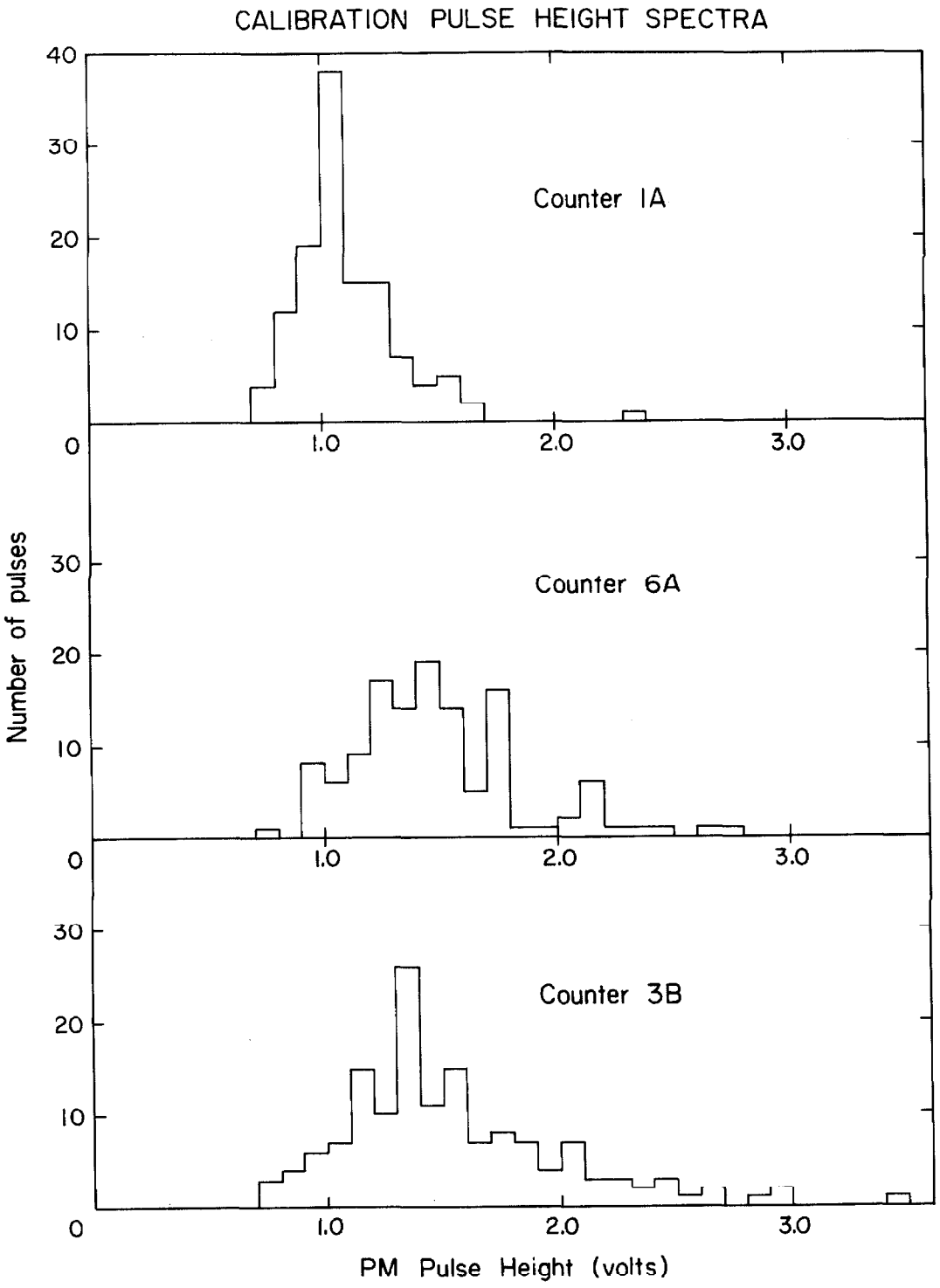
CALIBRATION PULSE HEIGHT SPECTRA
Counter 1A
Counter 6A
Counter 3B
Number of pulses
PM Pulse Height (volts)
0
10
20
30
40
1.0
2.0
3.0

Figure 32

2. Geometrical effects from μ's going at large angles to the counter normals (5%).

3. Absorption effects from one end of the scintillator to another (7%).

4. Variation in light collection efficiency over the scintillator.

B. Fast Display Sweep Calibration

The sweep calibration for each trace was obtained from measurements on photographs of displays of a signal from a known frequency oscillator. The calibration was performed once during the midpoint of the experiment. The results showed some non-linearities at the extremities of the sweep.

C. Spark Chamber Depth Calibrations

One of the limitations on the accuracy of the depth measurements in the spark chambers is the accuracy of the relationship connecting the distance between sparks and reflections to the depth. For a plane mirror all that is required is the angle of the mirror with the optical axis and the location of one point on the mirror. In this case the depth, Z, is given by

$$Z = \frac{d}{\sin 2\alpha} + X \tan \alpha + C.$$

The sketch below shows how various quantities are defined with all quantities shown in the positive sense. C is a constant depending on

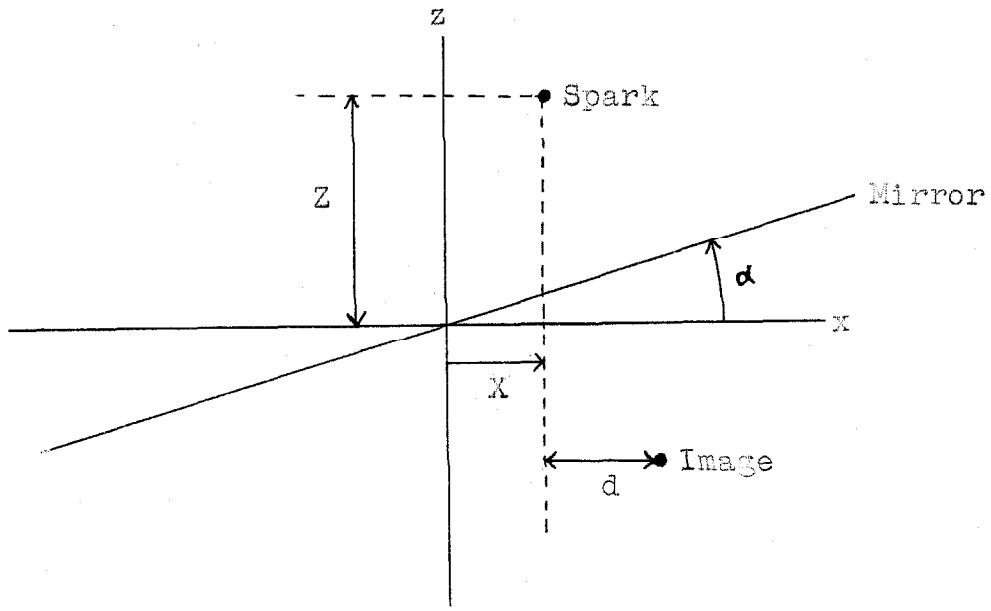
z
Spark
Z
Mirror
α
x
X
Image
d

thickness and refractive index of plane refracting material between spark and mirrors. The angle α has a value around 3^{o} which means $1/\sin 2\alpha \simeq 10$.

The midpoint of the spark chambers is about 25 cm from the mirrors so that a 1% error in α means an error of 0.25 cm in the Z coordinate of an average spark. In the π chamber, where about 3.5 cm of the π trajectory are sampled, an uncertainty of 0.25 cm in depth means a nearly 5^{o} uncertainty in the polar angle of the π trajectory. Extrapolating the π trajectory with 5^{o} uncertainties back to the stopper to find the decay vertex results in an uncertainty of about 1 cm in the location of the decay vertex. Such uncertainties seriously weaken the effectiveness of kinematic fits for rejecting false events.

An error of 1% for α is difficult to avoid considering the construction of the spark chambers, therefore an in situ calibration of the depth measuring scheme is necessary. The plate glass mirrors were mounted with double-sided tape in grooves milled in a 1-inch thick lucite plate. The mirror angles with respect to the back surface of the plate were quite uniform and could be measured to less than 1%. However, when the plates were screwed to the spark chamber they could twist and alter the mirror angles in a systematic manner by more than 1% of α. Twisting could also bow the long mirrors, thereby changing the total mirror angles. The spark chambers themselves were tilted slightly with respect to the optical axis, thus resulting in additional uncertainty in the depth calibration.

At the end of the experiment a series of overexposed photographs were made with the flash tubes on the fiducial plates as bright as possible. The grid lines on the fiducial plate served as a source of light at a known distance from the mirrors. By making measurements on the lines and reflections from these lines, it is possible to solve for α and tabulate it as a function of position in the chamber. Since the changes in α from the average are small and vary smoothly with position, it was useful to fit the data on α to a quadratic function of x and y, using a minimum chi squared technique. This procedure had an additional advantage in that it "smoothed out" statistical fluctuations in the data that are due to random errors so that α at a given point is more accurate than using the result of one measurement in the vicinity of that point.

The calibration, using the overexposed fiducial plate, was limited in its accuracy because:

(a) The distance of the fiducial plate to the mirrors was not accurately known at all points over the chamber.

(b) The camera angle changed significantly between the production runs and the depth calibration run.

(c) On all chambers except number 3 the grid lines made small angles with respect to the gaps. Under these conditions the difficulty in locating corresponding points on the source and the distorted reflection results in an uncertain calibration. For chamber number 3 some

grid lines ran perpendicular to the gaps; here reflections were better and the difficulty in locating corresponding points doesn't affect the calibration.

In each gap there were two mirrors, one at an angle $+ \alpha_o$ and the other at $- \alpha_o$ with respect to the mirror plate. The results in chamber 3 indicate that the angle between adjacent mirrors was a constant $2\alpha_o$, but that the angles with respect to the optical axis changed systematically over the chamber.

Assuming that the angle between adjacent mirrors is constant, it is possible to calibrate using measurements on sparks from tracks where both reflections of a spark are present. For this situation only two parameters, the depth of the spark and the angle of one of the mirrors with respect to the optical axis, are unknown and can be computed from the measurements. A calibration of all chambers was achieved utilizing this method and measurements on tracks that pointed towards the stopper. These tracks were perpendicular to the plates and thus avoided the problem of locating corresponding points on reflections and source. Here, as before, the data on α were fit with a quadratic function of position, (x, y), of the spark by a minimum chi squared technique. Good fits were obtained for all chambers using 100 to 200 points scattered uniformly over each chamber.

The second calibration procedure rests on the assumption that the angle between adjacent mirrors is constant and accurately known. Sometime after the experiment the mirror plates were removed and

the mirror angles measured while the mirror plate was mounted on a mill bed. The measurements indicated that angles were constant to about 1/2%. Mounting the mirror plates to the spark chambers could only twist the plate and result in a slow change as a function of position for the angles with respect to the optical axis but not affect the angle between adjacent mirrors. The measurements on the over-exposed fiducial plate for chamber 3 showed that the angles between adjacent mirrors were constant to within 1%, which was within the precision of the technique.

All measurements used in the calibrations were made on a digitized measuring table. Nonlinearities due to the field lens, camera and projection systems were eliminated by measuring three fiducial points in the vicinity of the sparks being measured and using these points to determine a local transformation of the data to the laboratory coordinate system.

APPENDIX IV

ADDITIONAL EVIDENCE FOR K^+ IDENTIFICATION

A. The dE/dx Counter Spectra

In Section III B on the K^+ identification it was pointed out that the dE/dx counter pulse height spectrum for all the 5584 $K_{\pi_2\gamma}$ triggers agreed with the spectrum expected for stopping K's. The details for this evidence as well as the spectra for events with good π-μ decays in channels 2 through 5 and for the 174 $K_{\pi_2\gamma}$ candidates will be presented in this appendix.

From measurements on the π and K chamber tracks for events from the $K_{\pi 2}$ and $K_{\mu 2}$ calibration runs discussed in Section III C 2, it is possible to determine the K^+ decay vertex and hence the range of the K^+ after the dE/dx counter. This range then specifies what the energy of the K^+ was at the dE/dx counter. Using standard curves (23) for dL/dx and $\int(\frac{dL}{dx})\,dx$ as functions of the residual range coupled with a measurement of the pulse height for minimum ionizing particles in the dE/dx counter allows the K^+ range to be transformed into an expected dE/dx counter pulse height. In this way the K^+ range distribution was transformed into the expected dE/dx counter pulse height distribution which is plotted in Figure 33A. Not all of the $K_{\pi 2}$ and $K_{\mu 2}$ calibration events were measured; only those with two or more γ tracks. This should in no way bias the K^+ range distribution. The observed dE/dx counter spectrum for all the $K_{\pi 2}$ and $K_{\mu 2}$ calibration events

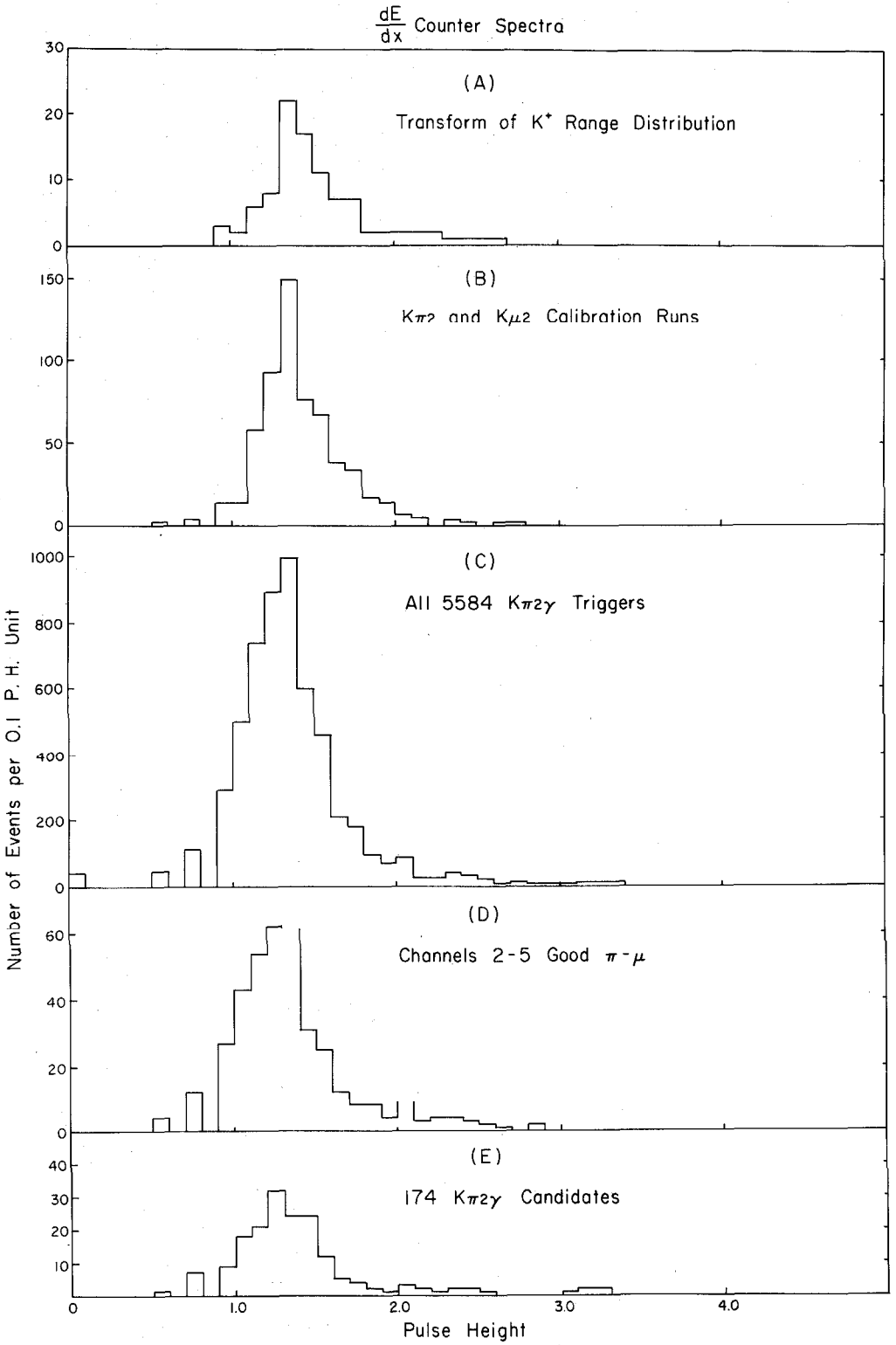
dE/dx Counter Spectra
(A)
Transform of K+ Range Distribution
(B)
Kπ2 and Kμ2 Calibration Runs
(C)
All 5584 Kπ2γ Triggers
(D)
Channels 2-5 Good π-μ
(E)
174 Kπ2γ Candidates
Number of Events per 0.1 P.H. Unit
Pulse Height
0
1.0
2.0
3.0
4.0

Figure 33

is plotted in Figure 33B and compares favorably with the transform of the K^+ range distribution.

The triggering requirements for the $K_{\pi 2}$ and $K_{\mu 2}$ calibration runs should not cause the calibration events to have any different K range distribution than the K's which stopped in the production runs. The dE/dx counter pulse height spectra observed for all 5584 $K_{\pi_2\gamma}$ triggers, for the events with good π-μ decays in channels 2 through 5, and for the 174 $K_{\pi_2\gamma}$ candidates are plotted in Figures 33C, 33D and 33E respectively. Each of these spectra are consistent with observed spectrum (B) of the $K_{\pi 2}$ or $K_{\mu 2}$ calibration runs and the expected spectrum (A) of the calibration runs.

B. Additional K^+ Lifetime Plots

Figure 6 in the main text exhibited the Fitch to counter 1A and the Fitch to counter 1B delays as measured on the fast display for all 5584 $K_{\pi_2\gamma}$ triggers. These delays essentially measure the time elapse from the time the K^+ stopped until it decayed. The curves in Figure 6 gave excellent agreement with the K^+ lifetime.

Figure 34 presents similar plots for a particularly important subclass of the 5584 $K_{\pi_2\gamma}$ triggers known as Group II, or those events with π's stopping in channels 2 through 5 and showing a good π-μ decay. The corresponding plots for the 174 $K_{\pi_2\gamma}$ candidates are shown in Figure 35; in each case the agreement with the K^+ lifetime is excellent as can be seen from high χ^2 probabilities.

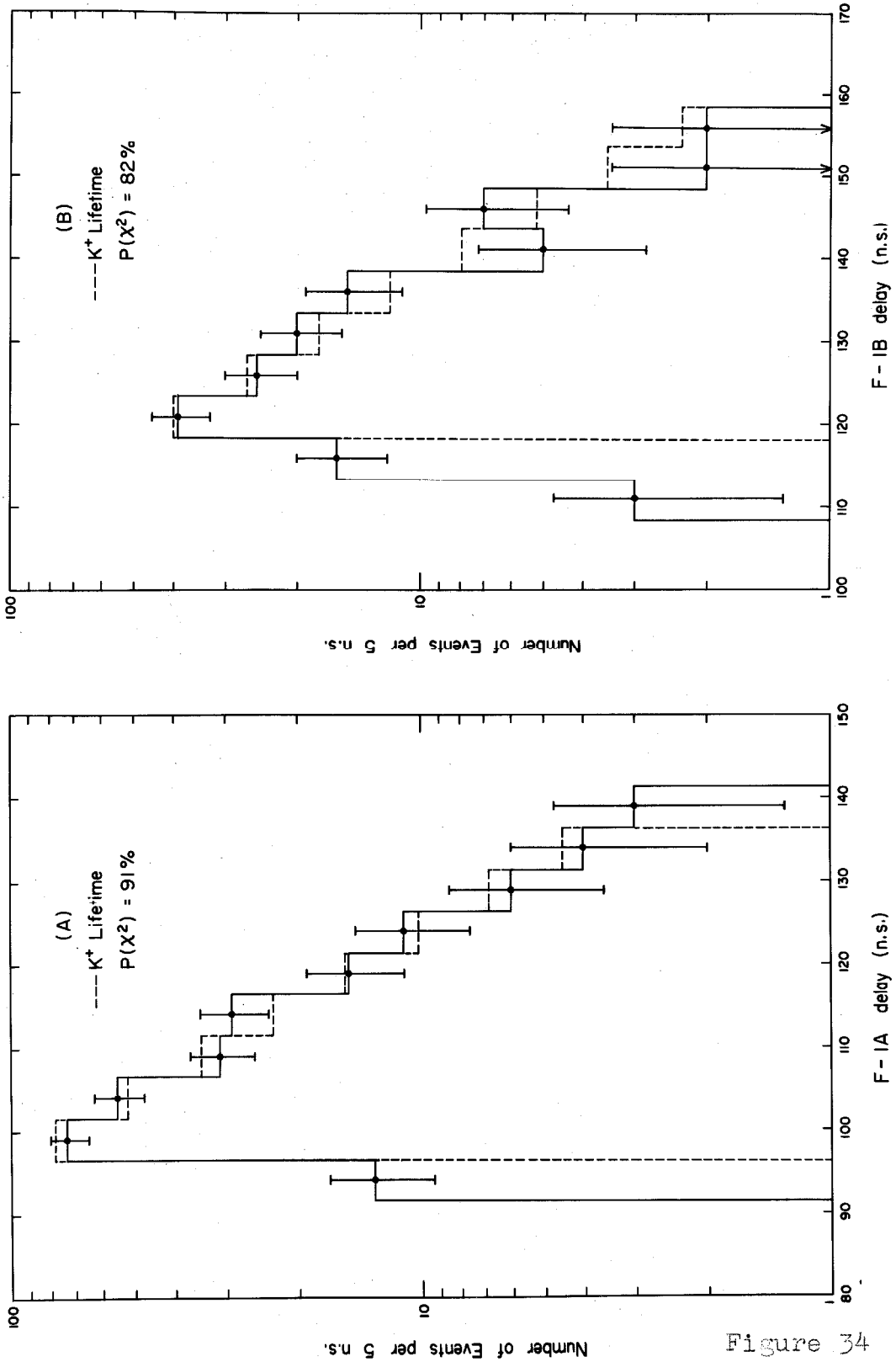
(A)
---K⁺ Lifetime
P(χ²) = 91%
Number of Events per 5 n.s.
F - IA delay (n.s.)
(B)
---K⁺ Lifetime
P(χ²) = 82%
Number of Events per 5 n.s.
F - IB delay (n.s.)

Figure 34

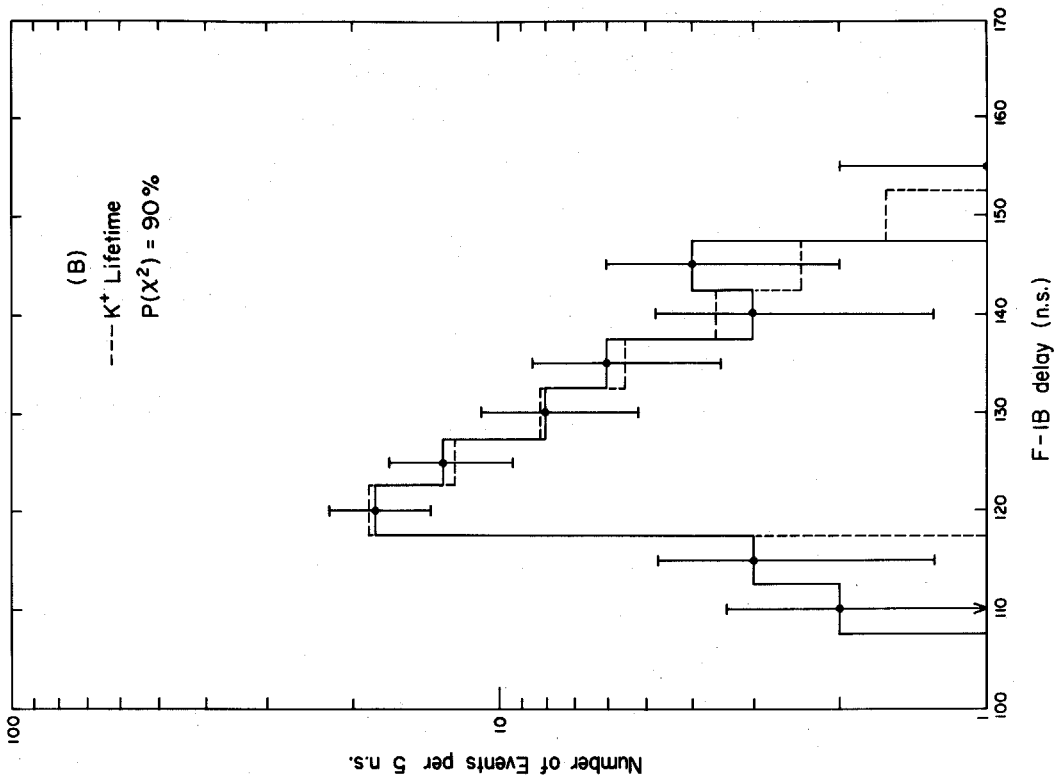
(B)
---K⁺ Lifetime
P(χ²) = 90%
Number of Events per 5 n.s.
F-IB delay (n.s.)

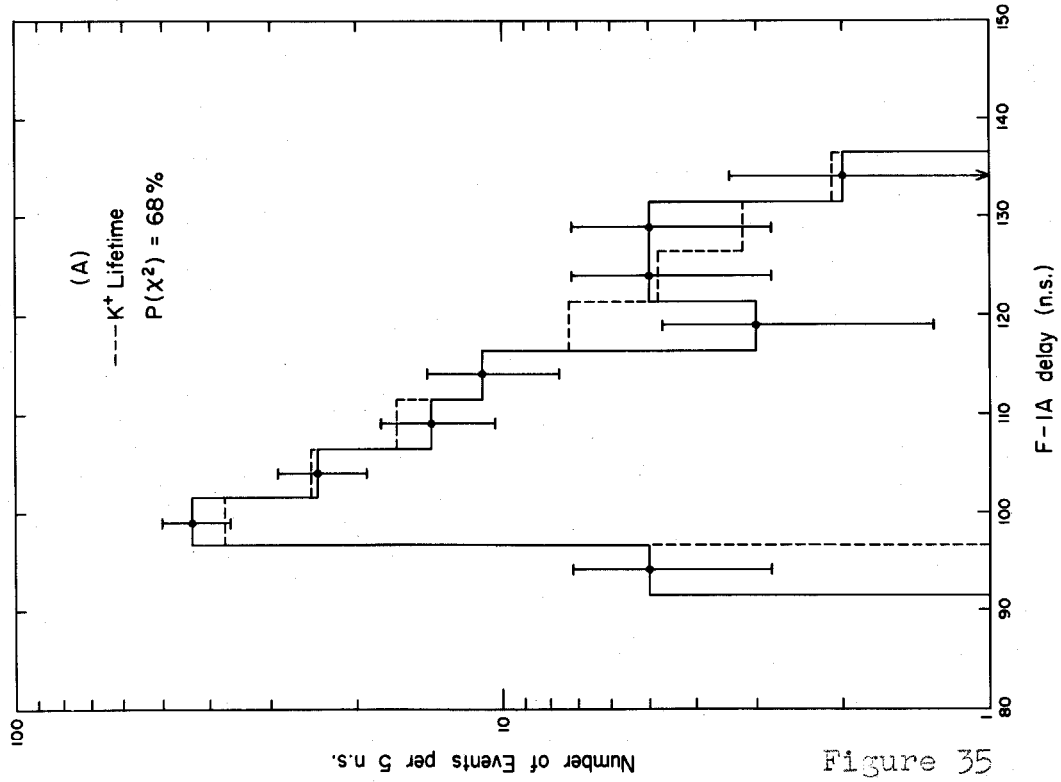
(A)
---K⁺ Lifetime
P(χ²) = 68%
Number of Events per 5 n.s.
F-IA delay (n.s.)

Figure 35

APPENDIX V

ADDITIONAL π-μ DECAY DATA

A. Mu delay Versus π Pulse Height Dot Plots

Figure 7 in the main text was a dot plot of the μ candidate delay versus the stopping π pulse height for counter 5B, the counter most plagued with reflections. As was discussed in Section III C 1, the dot plots such as shown in Figure 7 were used to eliminate the reflections and oscillations by discarding the events in the anomolous regions of the dot plots. A more representative sample of plots for a few other counters will be presented and discussed in this appendix.

The output of a computor program which sorted and tallied the two variables into a matrix will be presented instead of actual dot plots. Figure 36 is the output for counter 1A after allowing the program to "digest" the cards containing the fast display information for all $K_{\pi_2\gamma}$ triggers. The column of numbers to the left margin and the row of numbers at the very bottom are the μ candidates delay (t) and the stopping π pulse height (h) values (times ten) for the lower left hand corner of the appropriate rectangle of the corresponding dot plot as shown below:

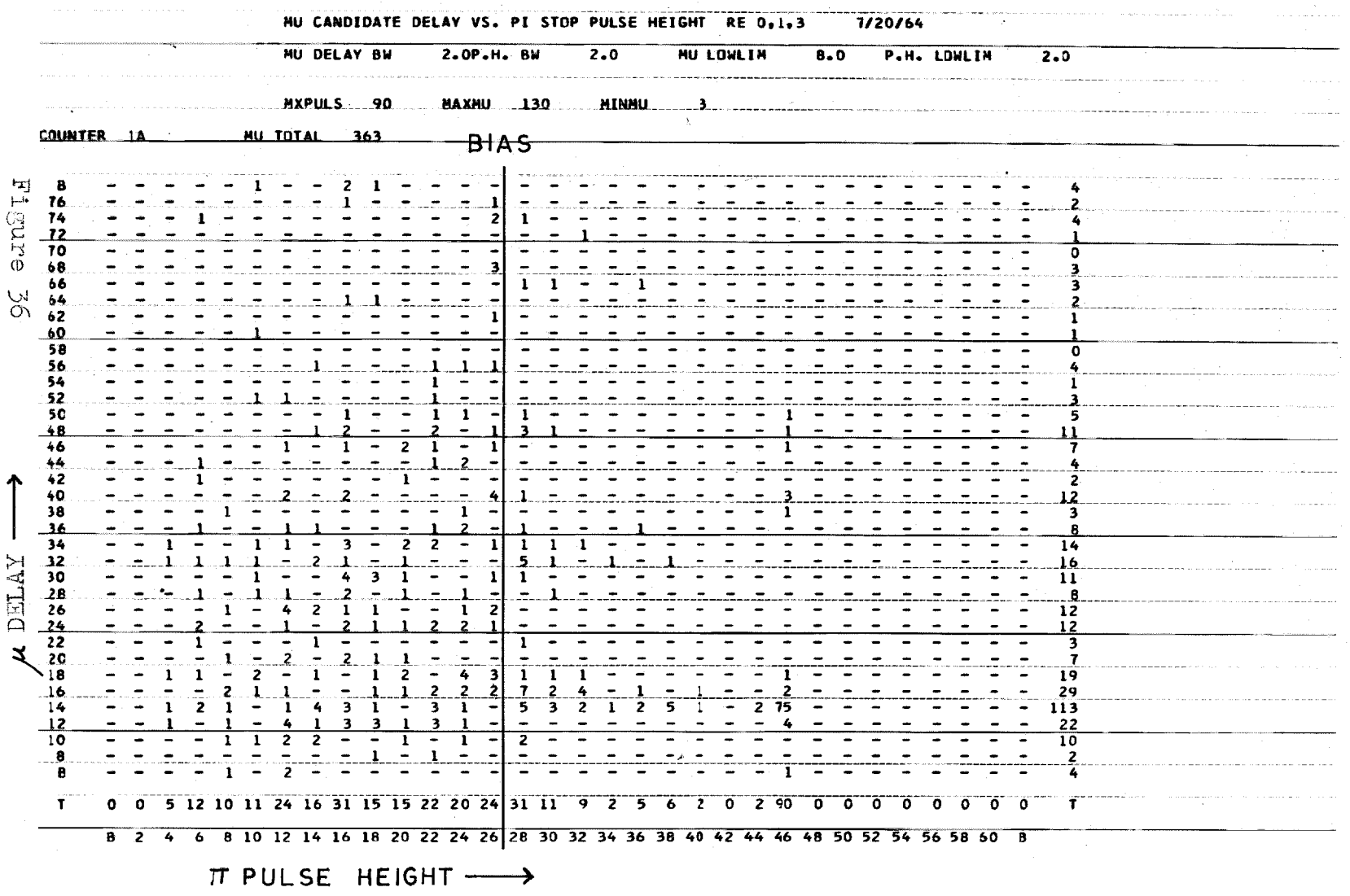
MU CANDIDATE DELAY VS. PI STOP PULSE HEIGHT RE 0,1,3 7/20/64
MU DELAY BW 2.OP.H. BW 2.0 MU LOWLIM 8.0 P.H. LOWLIM 2.0
MXPULS 90 MAXMU 130 MINMU 3
COUNTER 1A MU TOTAL 363
BIAS
B 0 0 5 12 10 11 24 16 31 15 15 22 20 24 31 11 9 2 5 6 2 0 2 90 0 0 0 0 0 0 0 0 T
B 2 4 6 8 10 12 14 16 18 20 22 24 26 28 30 32 34 36 38 40 42 44 46 48 50 52 54 56 58 60 B
μ DELAY ⟶
π PULSE HEIGHT ⟶

Figure 36

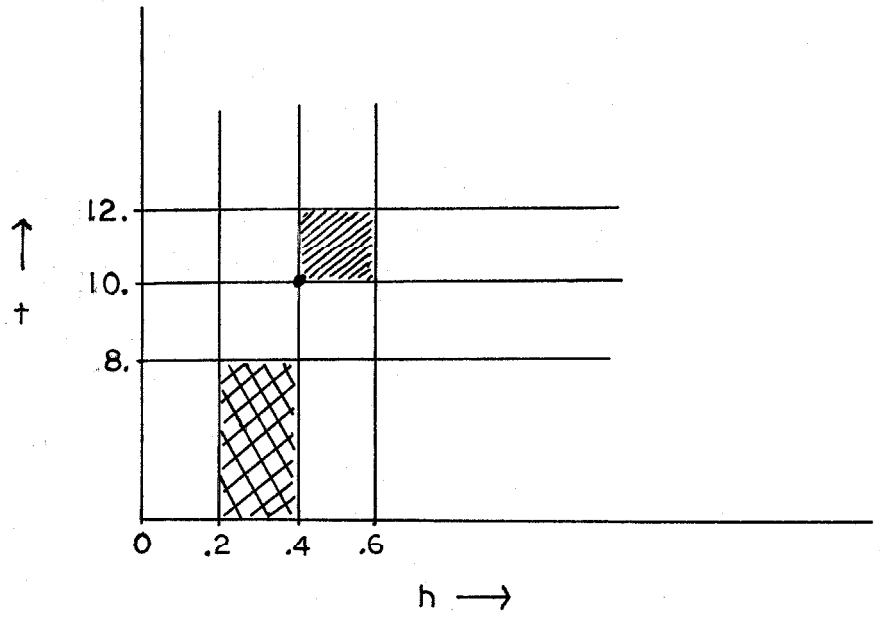

For example, the number of events falling in the shaded square would appear in the row labeled 10 and the column labeled 4 of the output. The two rows labeled B and the two columns labeled B in the computer output contain events falling in strips outside of the boundary which are given by the numbers next to the B's. For example, the number in lower B row and column labeled 2 in the computer output is for events falling in the cross hatch rectangular strip of the sketch above.

Each number in the row labeled T (at the bottom) contains the sum of all numbers in that column while each number in the column labeled T contains the sum of all numbers in that particular row. In this way the projections of the two dimensional distribution

onto either axis are easily read off. Additional information is contained in the heading; mu total is the total number of μ candidates observed, mu delay BW is the bin width of the μ delay variable, P. H. BW is the bin width on the pi pulse height, mu lowlim is the lower boundary on the μ delay, PH lowlim is the lower boundary of the π pulse height, maxpuls is the maximum π pulse height allowed; maxmu is the maximum μ delay allowed, and minmu is the smallest μ delay allowed.

The pulse height bias established to separate the anomolous region from the useful region is drawn in on the output. The plot for counter 1B is similar to the one shown for counter 1A in Figure 36. The plot for counter 2B shown in Figure 37 is similar to 2A, 4A and, except for total numbers, to 5A, 6A and 6B. Counter 3B shown in Figure 38 is unique in that its plot is all anomolous. Counter 3B should show very few π-μ decays because it was only 1/4 inch thick as compared to other counters such as 3A and was placed in front of the lower precessor. The pulse shape from 3B had a long tail which was often picked up by the scanners as a μ pulse riding on the tail of the π pulse. These events show up as the cluster at small μ delays and moderate π pulses heights. The cluster at the larger μ delay of 22 n. s. and at the larger π pulse heights appears to be from reflections.

B. Pi Lifetime Plots for Channels 1 and 6

The most convincing evidence for the proper identification of π-μ decays was seen in the histograms of the μ delay for those

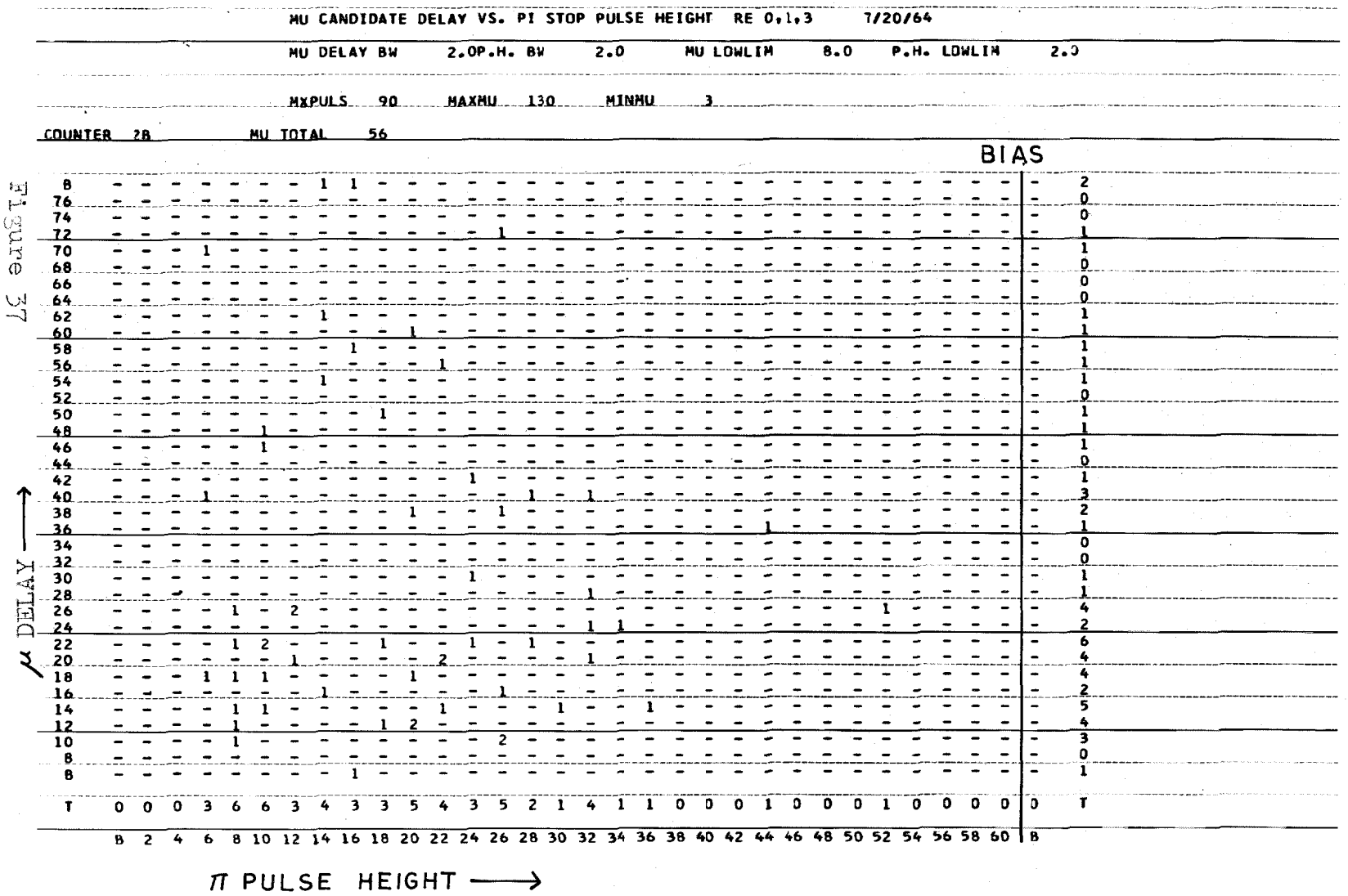
MU CANDIDATE DELAY VS. PI STOP PULSE HEIGHT RE 0,1,3 7/20/64
MU DELAY BW 2.0 P.H. BW 2.0 MU LOWLIM 8.0 P.H. LOWLIM 2.0
MXPULS 90 MAXMU 130 MINMU 3
COUNTER 28 MU TOTAL 56
BIAS
μ DELAY ⟶
π PULSE HEIGHT ⟶

Figure 37

MU CANDIDATE DELAY VS. PI STOP PULSE HEIGHT RE 0,1,3 7/20/64

MU DELAY BW 2.0 P.H. BW 2.0 MU LOWLIM 8.0 P.H. LOWLIM 2.0

MXPULS 90 MAXMU 130 MINMU 3

COUNTER 38 MU TOTAL 97

B	-	-	-	-	-	-	1	-	-	-	-	-	-	-	1	-	-	-	-	-	-	1	-	-	-	-	-	-	-	-	-	3
76	-	-	-	-	-	-	-	-	-	-	-	-	-	-	-	-	-	-	-	-	-	-	-	-	-	-	-	-	-	-	-	0
74	-	-	-	-	-	-	-	-	-	-	-	-	-	-	-	-	-	-	-	-	-	-	-	-	-	-	-	-	-	-	-	0
72	-	-	-	-	-	-	-	-	-	-	-	-	-	-	-	-	-	-	-	-	-	-	-	-	-	-	-	-	-	-	-	0
70	-	-	-	-	-	-	-	-	-	-	-	-	-	1	-	-	-	-	-	-	-	-	-	-	-	-	-	-	-	-	-	1
68	-	-	-	-	-	-	-	-	-	-	-	-	-	-	-	-	-	-	-	-	-	-	-	-	-	-	-	-	-	-	-	0
66	-	-	-	-	-	-	-	-	-	-	-	-	-	-	-	-	-	-	-	-	-	-	-	-	-	-	-	-	-	-	-	0
64	-	-	-	-	-	-	-	-	-	-	-	-	-	-	-	-	-	-	-	-	-	-	-	-	-	-	-	-	-	-	-	0
62	-	-	-	-	-	-	-	-	-	-	-	-	-	-	-	-	-	-	-	-	-	-	-	-	-	-	-	-	-	-	-	0
60	-	-	-	-	-	-	-	-	-	-	-	-	-	-	-	-	-	-	-	-	-	-	-	-	-	-	-	-	-	-	-	0
58	-	-	-	-	-	-	-	-	-	-	-	-	-	-	-	-	-	-	-	-	-	-	-	-	-	-	-	-	-	-	-	0
56	-	-	-	-	-	-	-	-	-	-	-	-	-	-	-	-	-	-	-	-	-	-	-	-	-	-	-	-	-	-	-	0
54	-	-	-	-	-	-	-	-	-	-	-	-	-	-	-	-	-	-	-	-	-	-	-	-	-	-	-	-	-	-	-	0
52	-	-	-	-	-	-	-	-	-	-	-	-	-	-	-	-	-	-	-	-	-	-	-	-	-	-	-	-	-	-	-	0
50	-	-	-	-	-	-	-	-	-	-	-	-	-	-	-	-	-	-	-	-	-	-	-	-	-	-	-	-	-	-	-	0
48	-	-	-	-	-	-	-	-	1	-	-	-	-	-	-	-	-	-	-	-	-	-	-	-	-	-	-	-	-	-	-	1
46	-	-	-	-	-	-	-	-	-	-	-	1	-	-	-	-	-	-	-	-	-	-	-	-	-	-	-	-	-	-	-	1
44	-	-	-	-	-	-	-	-	-	-	-	-	1	-	-	-	-	-	-	-	-	-	-	-	-	-	-	-	-	-	-	1
42	-	-	-	-	-	1	-	-	-	-	-	-	-	-	-	-	-	-	-	-	-	-	-	-	-	-	-	-	-	-	-	1
40	-	-	-	-	-	-	-	-	-	-	-	1	-	-	-	-	-	-	-	-	-	-	-	-	-	-	-	-	-	-	-	1
38	-	-	-	-	-	-	-	-	-	-	-	-	-	-	-	-	-	-	-	-	-	-	-	-	-	-	-	-	-	-	-	0
36	-	-	-	-	-	-	-	-	-	-	-	-	-	-	-	-	-	-	-	-	-	-	-	-	-	-	-	-	-	-	-	0
34	-	-	-	-	-	-	-	-	-	-	-	-	-	-	-	-	-	1	-	-	-	-	1	-	-	-	-	-	-	-	-	2
32	-	-	-	-	-	-	-	-	-	-	1	-	-	-	-	-	-	-	-	-	-	-	-	-	-	-	-	-	-	-	-	1
30	-	-	-	-	-	-	-	-	-	-	-	-	-	-	-	-	-	-	-	-	-	-	-	-	-	-	-	-	-	-	-	0
28	-	-	-	-	-	-	-	-	-	-	-	-	-	-	-	-	-	-	-	-	-	-	-	-	-	-	-	-	-	-	-	0
26	-	-	-	-	-	-	-	-	-	-	-	-	-	1	-	-	-	-	-	3	1	2	-	1	-	1	-	-	-	-	-	9
24	-	-	-	-	-	-	-	-	-	-	-	-	-	-	-	-	1	2	1	4	4	1	-	-	-	-	-	-	-	-	-	13
22	-	-	-	-	-	-	-	-	-	-	-	-	-	-	-	3	2	1	4	1	1	1	-	-	-	-	-	-	-	-	-	13
20	-	-	-	-	-	-	-	-	-	-	-	-	-	1	-	-	3	1	-	-	-	-	-	-	-	-	-	-	-	-	-	5
18	-	-	-	-	-	-	-	-	-	-	-	-	-	-	-	-	-	-	1	-	-	-	-	-	-	-	-	-	-	-	-	1
16	-	-	-	-	-	-	-	-	-	-	1	-	-	-	-	-	-	-	-	-	-	-	-	-	-	-	-	-	-	-	-	1
14	-	-	-	-	-	-	1	-	-	-	-	-	1	-	-	-	-	-	-	-	-	-	-	-	-	-	-	-	-	-	-	2
12	-	-	-	-	-	-	-	-	-	-	-	-	1	-	-	-	-	-	-	-	-	-	-	-	-	-	-	-	-	-	-	1
10	-	-	-	-	-	-	1	-	1	1	2	1	1	-	-	-	-	-	1	-	-	-	-	-	-	-	1	-	-	-	-	9
8	-	-	-	-	-	-	1	-	1	2	4	3	-	1	2	-	-	-	-	-	-	-	-	-	-	-	-	-	-	-	-	14
6	-	-	-	-	-	1	-	-	1	2	4	2	5	1	1	-	-	-	-	-	-	-	-	-	-	-	-	-	-	-	-	17
T	0	0	0	0	0	2	4	0	4	5	12	8	9	5	4	3	6	5	7	5	8	4	3	0	1	0	2	0	0	0	0	T
	8	2	4	6	8	10	12	14	16	18	20	22	24	26	28	30	32	34	36	38	40	42	44	46	48	50	52	54	56	58	60	8

μ DELAY ⟶

π PULSE HEIGHT ⟶

Figure 38

events tentatively designated as π-μ delays. For the group II events plotted in Figure 8 and the $K_{\pi_2\gamma}$ candidates in Figure 9 the histograms were exponential and quite consistent with the π^+ lifetime. Figure 39 in this appendix shows histograms for the 389 channel 1 and 206 channel 6 events which were the Group I and Group III events discussed in Section III C1. The channel 1 events fit the π^+ lifetime well and have a χ^2 probability of 57% considering the μ delay region from 12 to 77 ns. Channel 6 events give a χ^2 probability of 16% for the region from 10 to 50 ns. The μ delay region beyond 50 ns is about where the oscilloscope trace ends for most 6B events; for 6A there is about 20 more ns available. The cut off is not sharp, however, because the amount of oscilloscope trace left depends upon how long it took the K^+ to decay. The channel 6 data is consistent with the π^+ lifetime but is not as convincing as the data from the other channels.

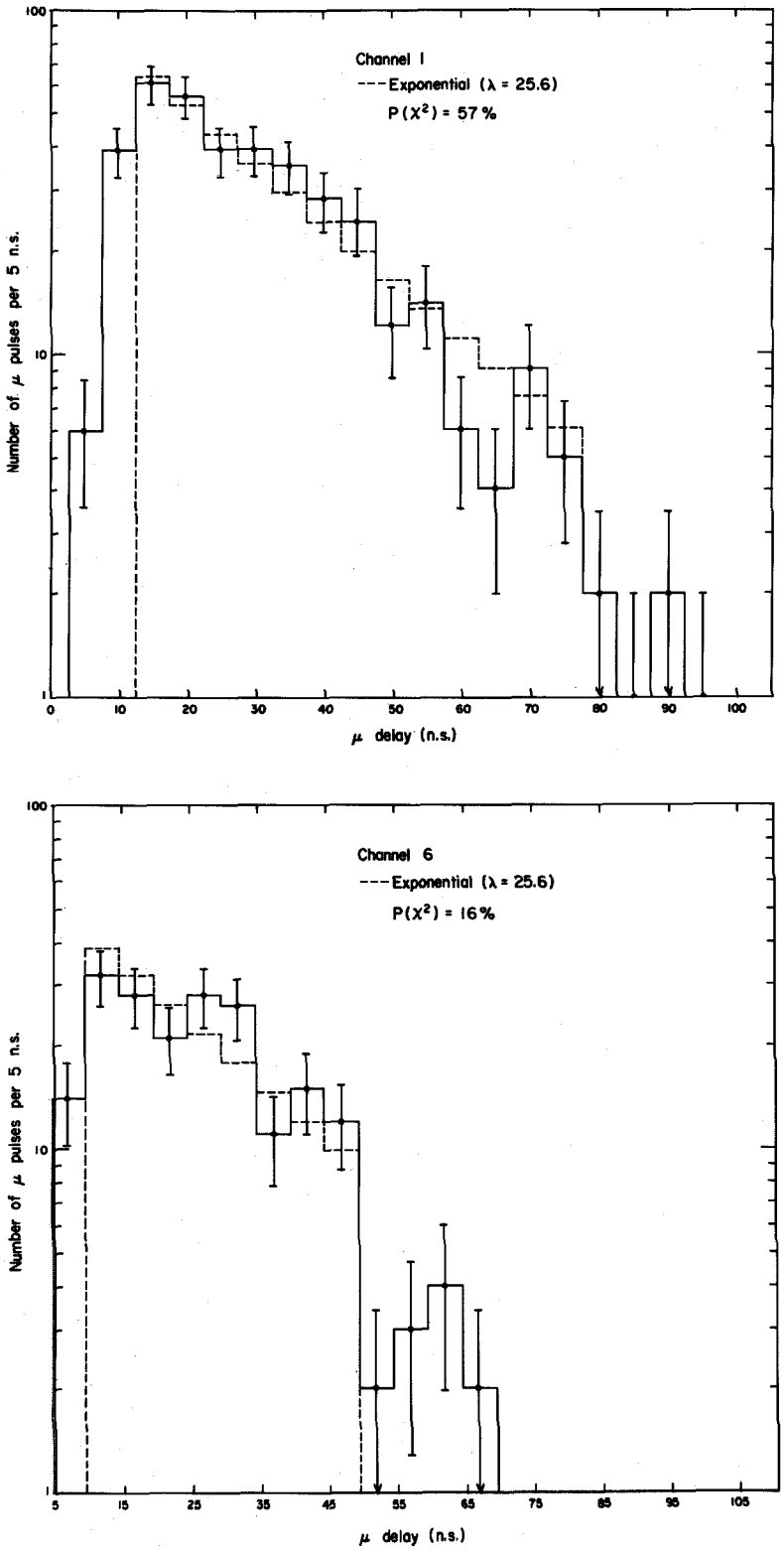
Channel 1
---Exponential (λ = 25.6)
P(X²) = 57 %
Number of μ pulses per 5 n.s.
μ delay (n.s.)
Channel 6
---Exponential (λ = 25.6)
P(X²) = 16%
Number of μ pulses per 5 n.s.
μ delay (n.s.)

Figure 39

APPENDIX VI

CALCULATION OF $K_{\pi 2}$ PHOTON DISTRIBUTIONS

The distributions of the various kinematic quantities describing the $K_{\pi 2}$ decay and subsequent π^o decay can be completely characterized and predicted. As a check on the experiment the predicted behavior can be compared with data from the $K_{\pi 2}$ "calibration" runs. For this purpose the quantities of interest are:

1. The fraction of $K_{\pi 2}$ decays satisfying the triggering scheme.
2. The azimuthal angle distributions for one and two γ events separately.
3. The relative number of zero, one and two γ events.
4. The distribution of the number of γ spark chamber plates traversed before the γ's convert.

A Monte Carlo program was coded to compute these quantites.

The calibration runs containing the $K_{\pi 2}$ events were triggered on K^+ decays in coincidence with channels 1, 5 and 6 of the π hodoscope. The simplified model of the experiment used in the calculation is shown schematically in Figure 40. The γ spark chambers have become a homogeneous medium bounded by the surfaces of two concentric cylinders with radii ρ_1 and ρ_2 where a pie shaped section is cut out for the π hodoscope. The three planes P_1, P_2, and P_3 are used to approximate the requirements

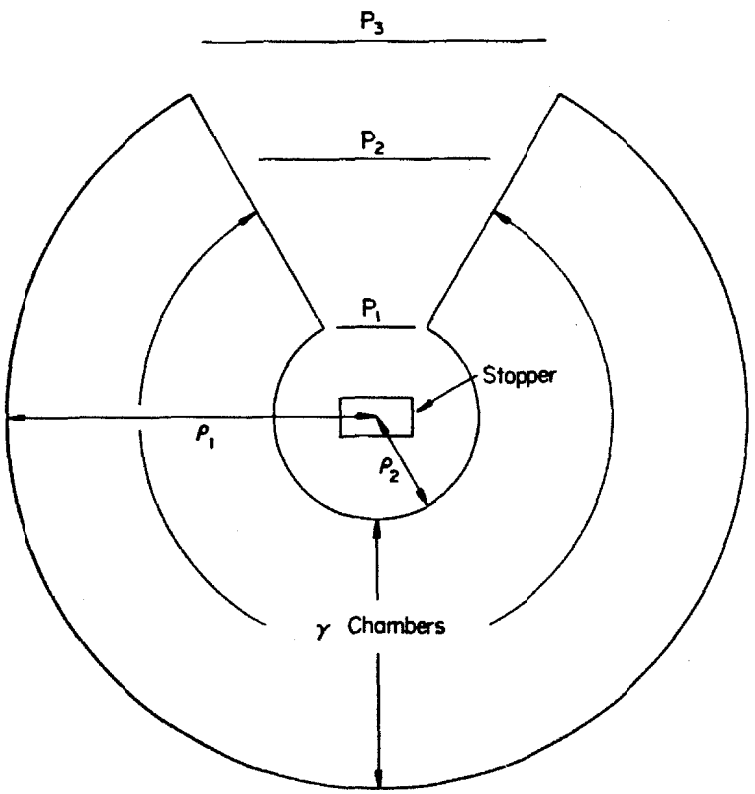

Front View

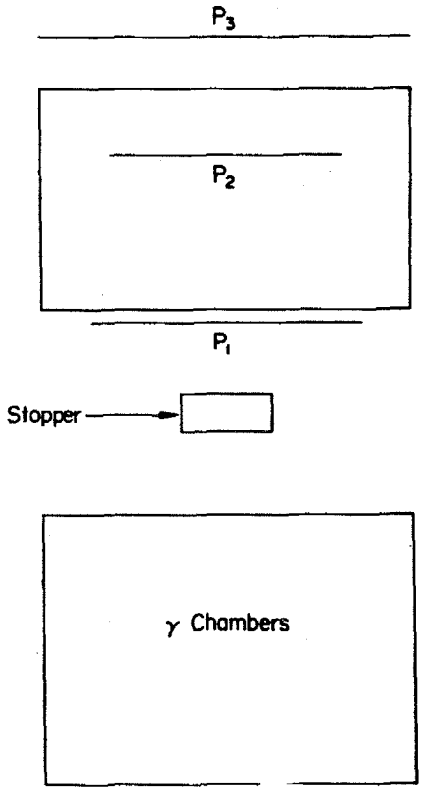

Side View

Simplified Model

Figure 40

on the π for passing through the sensitive region of the π chamber (P_1) and activating the π hodoscope channels 1, 5 and 6.

In the computation π^+ decay vertices were generated in the stopper with spatial distributions given by results of measurements on the calibration runs. The π^+ directions were generated isotropically and the requirements of triggering and of having a good π chamber track were simulated by requiring successful π's to go through the plane sections P_1, P_2 and P_3. After a successful trigger was encountered a π^o decay was generated which was isotropic in the π^o center of mass, then the amount of spark chamber material along each γ trajectory was computed. By using a known conversion length describing the conversion of γ's in the spark chamber material the probabilities for zero, one or two γ conversions were computed and the numbers added to the appropriate azimuthal angle bins. The probabilities for each γ converting in the various plates were computed and tallied in cells corresponding to the plates. The results are tabulated below. The azimuthal angle distributions are shown summed for each chamber and expressed as a percentage of all photons of that category converting in the designated chamber.

No. of Photons per event	Probability %	Corrected Prob. %
0	6	12
1	60	60
2	34	28

γ Azimuthal Angular Distributions

Chamber No.	One photon events (%)	Two photon events (%)	One or Two Photon events (%)
1	1.0	5.0	3.2
2	10.0	22.1	16.4
3	78.0	45.8	60.8
4	10.0	22.1	16.4
5	1.0	5.0	3.2

The point of conversion distributions gave an exponential distribution with a conversion length of 9.5 plates as compared to 10.3 plates for photons that are all normally incident to the plates.

Neglected in this calculation were corrections due to conversion of photons in the stopper, lucite walls and aluminum plates. These corrections can be approximated by using the chance for an average photon to convert in the stopper, etc. The corrected probabilities are listed above. Also neglected in these calculations were the effects due to the walls of the spark chamber which introduce regions of lucite instead of steel plate.

APPENDIX VII

CALCULATION OF π^+ INTERACTIONS

One source of short range π^+ from K^+ decays in this experiment is inelastically scattered π^+ where the π^+ comes from the $K_{\pi 2}$ mode. Because the ratio $K_{\pi_2\gamma}/K_{\pi 2}$ is of the order of 10^{-3}, a "small" percentage of scatters may prove to be a larger effect than $K_{\pi_2\gamma}$. A Monte Carlo calculation using experimental π^+ inelastic scattering cross sections was used to predict the number of inelastically scattered π^+ from $K_{\pi 2}$ as well as the π^+ range distribution in the hodoscope. The distribution of photons from the π^o decay is also available from the calculation. A modification of the program generated background events for kinematic fitting by adding enough "accidental photon conversions" to make three γ events out of the $K_{\pi 2}$ interactions events.

The model of the geometry and triggering requirements is essentially the same as the one used to compute behavior of $K_{\pi 2}$ events except that the top plane of the hodoscope, P_3 shown in Figure 40, was moved down to correspond to the position of channel 4 instead of channel 6 so as to be an average position between 2 and 5. The $K_{\pi 2}$ decays were generated in the same manner as described in Appendix VI. The main difference between the two calculations is that here one allows the π^+ to interact in the stopper. The point of interaction was generated to be uniform along the path of the π's original direction. The energy loss in the interaction

and the scattering's angles were generated as independent variables within each of the four energy loss regions considered, and will be discussed shortly. Within each energy region except one, the π^+ energy loss was taken as uniformly distributed; the π^+ azimuthal scattering angle was also uniformly distributed while the polar angle was distributed according to the data on π^+ inelastic scattering which will be discussed later. After the inelastic scattering variables were generated, those π's that had enough energy and the right direction to get into the telescope were tallied in the appropriate range and projected range bins. Each tally was weighted according to the probability for interaction as given by the total cross section for inelastic scattering in the energy range under consideration and by the amount of stopper material along the π's original trajectory.

The π^+ inelastic scattering data which were used are listed below:

1. Angular distribution of elastic scattering of 87 MeV π^+ on oxygen (24). This was included because of back scatter could just make it into channel 6. The data is plotted in Figure 41A.
2. Inelastic scattering angular distribution of 87 MeV π^+ on oxygen in the region of $E_{e\ell} - 12 < E_\pi < E_{e\ell}$, E_π is the energy of the π after interaction (24). The energy was taken to be uniformly distributed in this region. The data is plotted in Figure 41B.

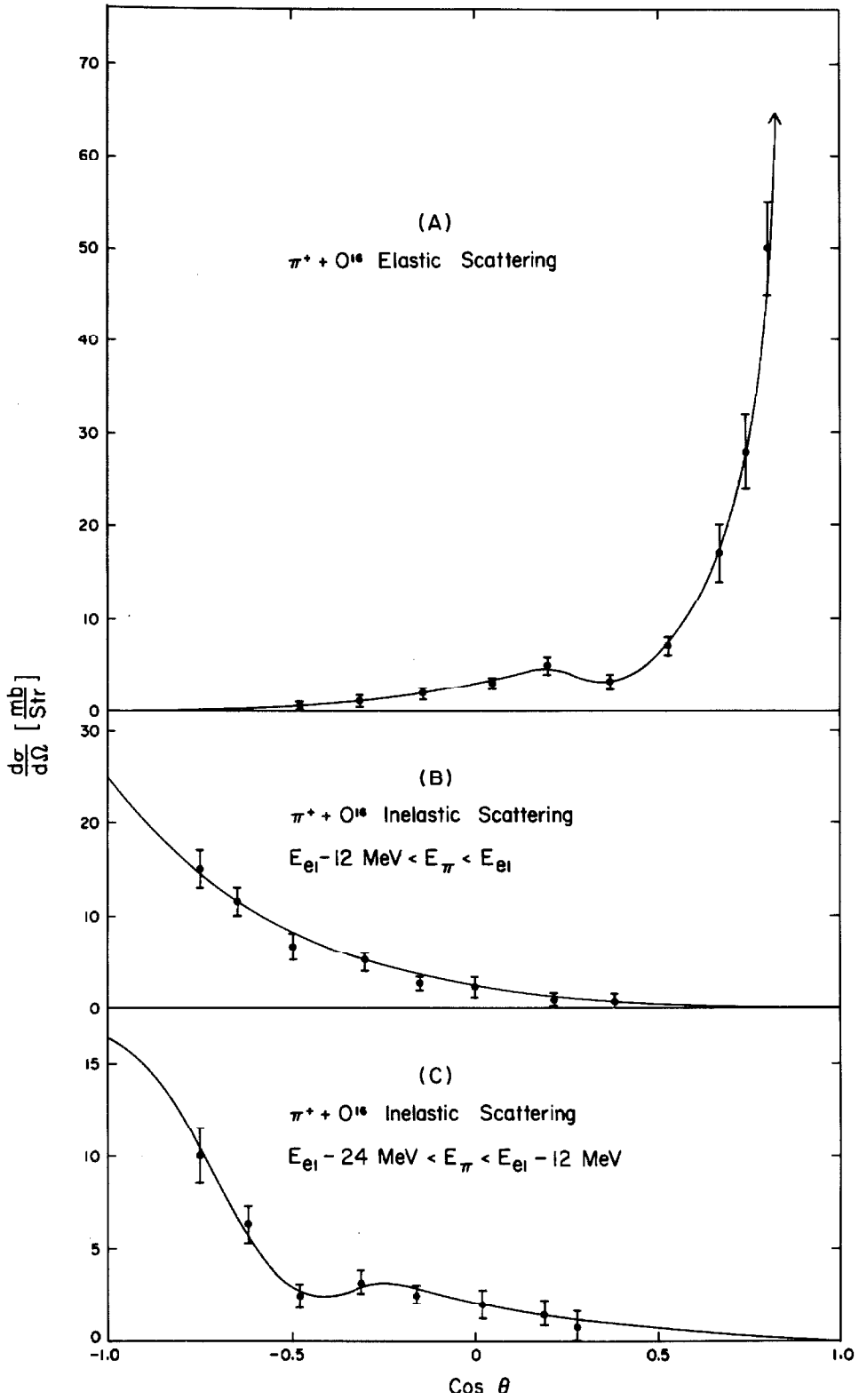
(A)
π⁺ + O¹⁶ Elastic Scattering
(B)
π⁺ + O¹⁶ Inelastic Scattering
E_el - 12 MeV < E_π < E_el
(C)
π⁺ + O¹⁶ Inelastic Scattering
E_el - 24 MeV < E_π < E_el - 12 MeV
dσ/dΩ [mb/Str]
Cos θ

Figure 41

3. Inelastic scattering angular distributions (24) of 87 MeV π^+ on oxygen in the region $E_{e\ell} - 24 < E_\pi < E_{e\ell} - 12$. The data is plotted in Figure 41C. In the calculation the angular distribution given here was used for the region $E_{e\ell} - 40 < E_\pi < E_{e\ell} - 12$ and the total cross section double that for the restricted energy region. The energy loss distribution was taken to be uniform.

4. Inelastic scattering of 125 MeV π^- on carbon (25) for the region $0 < E_\pi < E_{e\ell} - 40$. The angular distribution is shown in Figure 42A and the energy distribution of the scattered π is shown in Figure 42B.

The smooth curves are hand drawn fits to and extrapolation of the data. The total cross sections for each region were obtained by integrating under the smooth curves. The total cross sections are scaled to fluorine and carbon by the ratio of the appropriate atomic weights to the 2/3 power.

The results of the calculation are presented as the number of certain types of $K_{\pi 2}$ interaction events that the probabilities would predict should occur for the total number of $K_{\pi 2}$ decays in the experiment. One result is the number of π's stopping in each of the counters for the conditions upon which the 174 $K_{\pi_2\gamma}$ candidates were selected. These are shown in the table below along with the actual number in the 174 and the number expected when considering only the inner bremsstrahlung model for $K_{\pi_2\gamma}$.

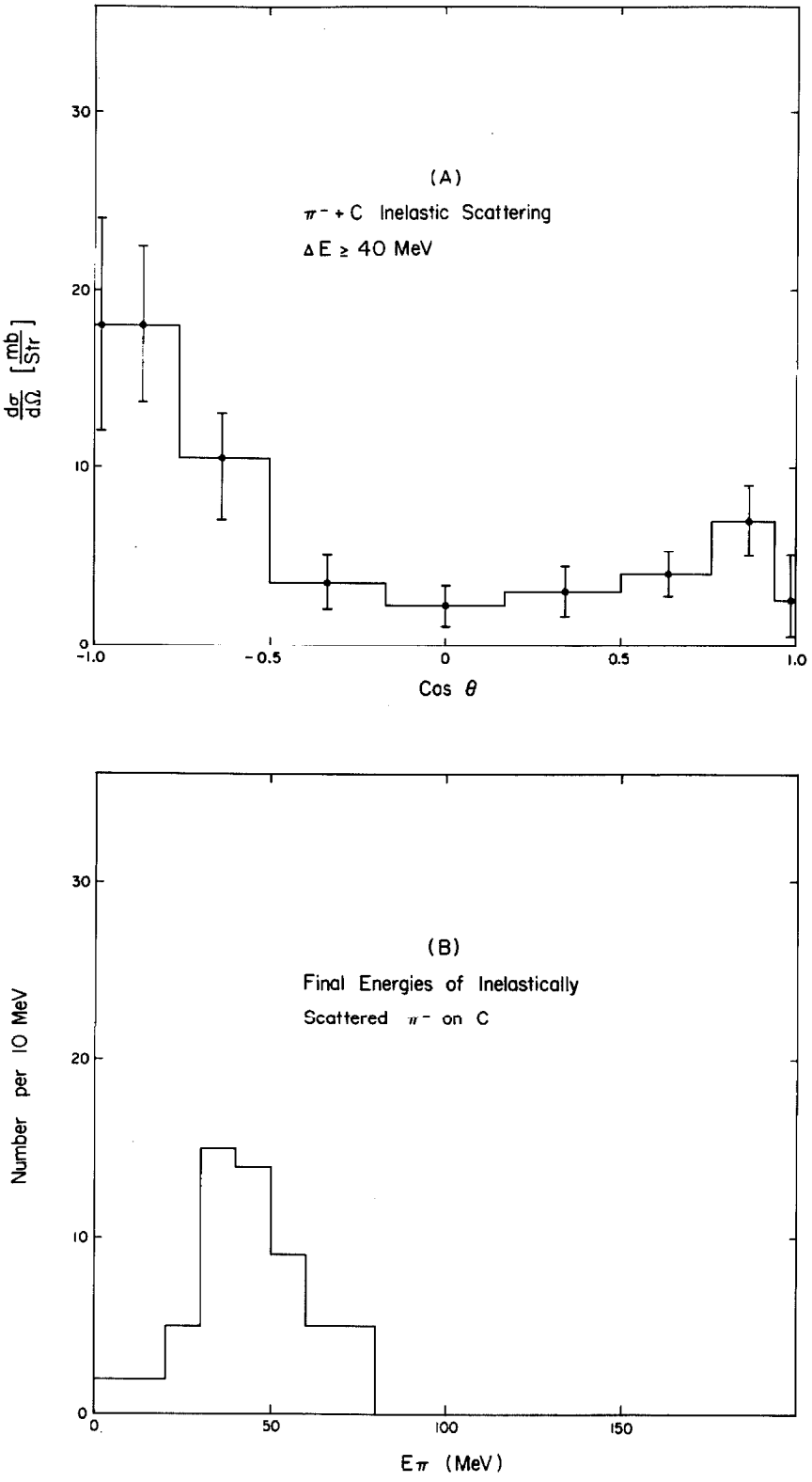
(A)
π⁻ + C Inelastic Scattering
Δ E ≥ 40 MeV
dσ/dΩ [mb/Str]
Cos θ
(B)
Final Energies of Inelastically
Scattered π⁻ on C
Number per 10 MeV
Eπ (MeV)

Figure 42

Counter	No. π's predicted	No. π's observed in 174	No. π's expected for inner bremsstrahlung
2A + 2B	21	68	~ 1.7
3A	15	19	~ 1.3
4A	23	29	~ 1.7
5A + 5B	55	58	~ 3.7
Total	114	174	~ 8.4

The γ distributions associated with the π^+ interaction events considered in the table above are shown below:

γ/Frame	(%) Frames
0	37
1	51
2	12

Chamber	(%) of γ's
1	27.5
2	17.5
3	10.
4	17.5
5	27.5

The results show that the events expected from $K_{\pi 2}$ interactions can account for most of the 174 candidates and completely overwhelms the number expected from inner bremsstrahlung.

The approximations made in this calculation such as using some π^- data instead of all π^+ data, extrapolating the data to unmeasured regions, and neglecting energy and angle correlations,

as well as the errors in the data itself, will not yield accurate results. The results may be as much as a factor of two off, but they are still useful for assessing whether the $K_{\pi 2}$ interactions are negligible, are comparable to, or completely swamp the 174 candidates.

APPENDIX VIII

KINEMATIC FITTING PROCEDURES

The procedures for kinematic fitting in both the $K_{\pi 2}$ and $K_{\pi_2\gamma}$ cases are very similar. The $K_{\pi_2\gamma}$ case will be discussed first, followed by a discussion of the simplifications and modifications for the $K_{\pi 2}$ mode. In each case there are three more items of data than are needed to determine the kinematical parameters of the decay, assuming one knows the identity of all particles and their masses. Kinematic fitting is a definite prescription for utilizing all data to obtain, in some sense, the "best" values for the parameters describing the event and a "figure of merit" describing the quality of the fit.

A. Fits to $K_{\pi_2\gamma}$

For the $K_{\pi_2\gamma}$ case the diagram in Figure 5 shows a set of parameters completely describing the decay. These are: $\vec{R}_o$, the decay vertex; $\vec{R}_1$, $\vec{R}_2$, $\vec{R}_3$, the points of conversion of the three photons, where $\vec{R}_1$ is the photon from the primary decay; $\vec{R}_4$, a point on the top of the stopper such that $\vec{R}_4 - \vec{R}_o$ is the direction of the π^+ as it emerged from the decay; and T_{π^+} the kinetic energy of the π^+. $\vec{R}_5$, a point on the π^+ trajectory in the middle of the π chamber such that $\vec{R}_5 - \vec{R}_4$ is in the direction of the π^+ after emerging from the stopper, is not needed to describe the original decay, but rather describes the π^+ after multiple scattering in the stopper. The data are $\vec{d}_1$, $\vec{d}_2$, $\vec{d}_3$ which are

the measured points of conversion; d_{ox} and d_{oy}, which are the measured x and y coordinates where the K^+ entered the stopper at $\vec{P}_K$; d_{4x}, d_{4z}, d_{5x}, d_{5z} which are the x and z coordinates of points at the top of the stopper and in the middle of the π chamber respectively and which are on a straight line that is given by a least squares fit to the sparks in the π chamber; and d_H which is the range of the π^+ in the π hodoscope.

The likelihood function, L, for an event is the same as the probability density for observing $\vec{d}_1$ through $\vec{d}_5$ and d_H given the values of the parameters $\vec{R}_o$ through $\vec{R}_4$ and T_{π^+}.

All measurements will be assumed to have gaussian error distributions. L is then equal to the product of the probability density for obtaining $\vec{d}_o$ through $\vec{d}_3$ and d_H from a measurement on an event given the decay parameters $\vec{R}_o$ through $\vec{R}_4$ and T_{π^+} and the probability density for obtaining $\vec{d}_4$ and $\vec{d}_5$ from a measurement given a π^+ of energy T_{π^+} emerging from $\vec{R}_o$ in direction $\vec{R}_4 - \vec{R}_o$. The first factor is a product of terms of the form

$$\frac{1}{\sqrt{2\pi}\,\sigma_i}\, e^{-\frac{(R_i - d_i)^2}{2\sigma_i^2}}$$

where i refers to a measured component of one of the points $\vec{d}_o$ through $\vec{d}_3$. The first term also has a factor

$$\frac{1}{\sqrt{2\pi}\,\sigma_H}\, e^{-\frac{(f_H(T_{\pi^+}, R_o, R_4) - d_H)^2}{2\sigma_H^2}}$$

where f_H is the computed range in the hodoscope for a π^+ with kinetic energy T_{π^+} emerging from $\vec{R}_o$ in direction $\vec{R}_4 - \vec{R}_o$. For the second factor in L, one must take account of multiple scattering in the stopper. Only angular changes due to multiple scattering will be considered because they have a greater effect than lateral displacements. The following sketch for the xy plane shows the geometry for a particular path:

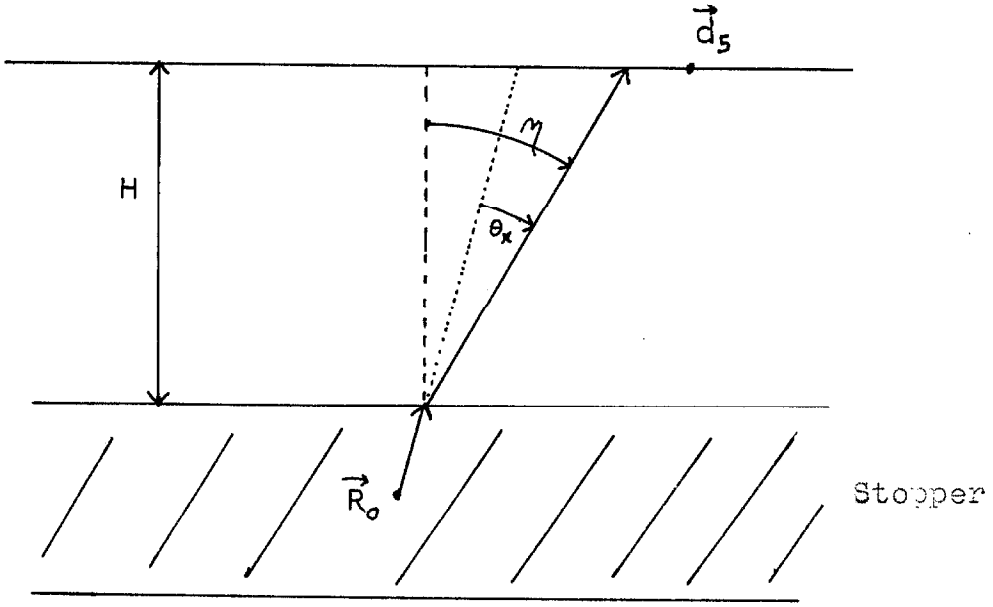

One way to analyze the problem is write the probability density with the multiple scattering angle, θ_x, also specified, then integrate over all possible θ_x. From the measurement error associated with the x components of $\vec{d}_4$ and $\vec{d}_5$ a factor (1) is obtained.

$$(1) \qquad \left(\frac{1}{\sqrt{2\pi}\,\sigma_{4x}} e^{-\frac{(R_{4x} - d_{4x})^2}{2\sigma_{4x}^2}}\right)\left(\frac{1}{\sqrt{2\pi}\,\sigma_{5x}} e^{-\frac{(R_{4x} + H\tan\eta - d_{5x})^2}{2\sigma_{5x}^2}}\right)$$

where $\eta = \theta_x + \arctan\left(\frac{R_{4x} - R_{ox}}{R_{4y} - R_{oy}}\right)$

Another factor comes from the probability for a scattering through θ_x and is expressed by

(2) $$\frac{1}{\sqrt{2\pi}\,\sigma_\theta} \; e^{-\frac{\theta_x^2}{2\sigma_\theta^2}}$$

The integral over θ_x for the product of expressions (1) and (2) is easily done when the approximation $\tan\theta \simeq \theta < 1$ is used. The result is

(3) $$\frac{1}{\sqrt{2\pi}\,\sigma_{4x}} \; e^{-\frac{(R_{4x} - d_{4x})^2}{2\sigma_{4x}^2}} \; \frac{1}{\sqrt{2\pi}\,\sigma_{5x}} \; e^{-\frac{(S_x - d_{5x})^2}{2\sigma_{5x}^2}}$$

where

$$S_x = R_{4x} + \frac{(R_{4x} - R_{ox})}{(R_{4y} - R_{oy})} \cdot H$$

and

$$\sigma_{Sx}^2 = \sigma_{5x}^2 + \sigma_\theta^2 H^2 \left[1 + \left(\frac{R_{4x} - R_{ox}}{R_{4y} - R_{oy}}\right)^2\right]^2$$

Similar results hold for the zy plane. Combining all factors, all of which are gaussian yields the result,

$$L = \left(\frac{1}{2\pi}\right)^{16/2} \left(\prod_{j=1}^{16} \frac{1}{\sigma_j}\right) \; e^{-\chi^2/2}$$

where

$$(4) \qquad \chi^2 = \sum_{i=1}^{16} \frac{(f_i - d_i)^2}{\sigma_i^2}$$

and the f_i are functions of the parameters. The fifteen parameters $\vec{R}_o$ through $\vec{R}_3$, R_{4x}, R_{4z} and T_{π^+} which describe the decay are not all independent; the energy and momentum conservation laws restrict the number of independent parameters to thirteen. For algebraic convenience the independent parameters are chosen to be the following set:

$$\vec{R}_o,\ \vec{B},\ \vec{C},\ D,\ A_x,\ A_z \text{ and } T_{\pi^+}$$

where

$$\vec{B} = \vec{R}_1 - \vec{R}_o$$

$$\vec{C} = \vec{R}_2 - \vec{R}_o$$

$$D = |\vec{R}_3 - \vec{R}_o|$$

$$A_x = R_{4x} - R_{ox}$$

$$A_z = R_{4z} - R_{oz}$$

Table IX shows the correspondence between of index, i, of expression (4) and the data as well as the functional dependence of the f_i and σ_i^2 on the independent parameters.

TABLE IX

$K_{\pi_2\gamma}$ KINEMATIC FITTING VARIABLES

i	Data	f_i	σ_i^2
1	d_{0x}	R_{ox}	$\sigma_{ox}^2 + C_1\Delta^2 + C_2\Delta^{1.82}$
2	d_{0y}	R_{oy}	$\sigma_{oy}^2 + C_1\Delta^2 + C_2\Delta^{1.82}$
3	d_{1x}	$R_{ox} + B_x$	σ_{1x}^2
4	d_{1y}	$R_{oy} + B_y$	σ_{1y}^2
5	d_{1z}	$R_{oz} + B_z$	σ_{1z}^2
6	d_{2x}	$R_{ox} + C_x$	σ_{2x}^2
7	d_{2y}	$R_{oy} + C_y$	σ_{2y}^2
8	d_{2z}	$R_{oz} + C_z$	σ_{2z}^2
9	d_{3x}	$R_{ox} + D\cdot\ell_x^*$	σ_{3x}^2
10	d_{3y}	$R_{oy} + D\cdot\ell_y^*$	σ_{3y}^2
11	d_{3z}	$R_{oz} + D\cdot\ell_z^*$	σ_{3z}^2
12	d_{4x}	$R_{ox} + A_x$	σ_{4x}^2
13	d_{4z}	$R_{oz} + A_z$	σ_{4z}^2
14	d_{5x}	$R_{ox} + A_x(1 + H/A_y)$	$\sigma_{5x}^2 + \sigma_\theta^2 H^2 T_x^2$
15	d_{5z}	$R_{oz} + A_z(1 + H/A_y)$	$\sigma_{5z}^2 + \sigma_\theta^2 H^2 T_z^2$
16	d_H	$R(T_\pi) - K\cdot A$	σ_H^2

TABLE IX (Continued)

$K_{\pi_2\gamma}$ KINEMATIC FITTING VARIABLES

$\Delta = R_{oz} - C_3$

C_3 = z coordinate of the front of the stopper facing into the K beam.

C_1 = Square of the angular uncertainty of the K beam.

$C_2\Delta^{1.82}$ = term gives uncertainty due to multiple scattering of K^+.

$\vec{\ell} = -\frac{1}{k_2}\left\{P_{\pi^+}\frac{\vec{A}}{A} + k\frac{\vec{B}}{B} + k_1\frac{\vec{C}}{C}\right\}$

A_y = $K_y - R_{oy}$, where K_y is height of top of the stopper.

$$k = \frac{M_K(M_K - 2E_{\pi^+}) + M_{\pi^+}^2 - M_{\pi^o}^2}{2\left(M_K - E_{\pi^+} + P_{\pi^+}\frac{\vec{A}\cdot\vec{B}}{AB}\right)}$$

$$k_1 = \frac{1}{2}M_{\pi^o}^2 \Big/ \left\{M_K - E_{\pi^+} + P_{\pi^+}\vec{A}\cdot\vec{C}/AC + k[\vec{B}\cdot\vec{C}/BC - 1]\right\}$$

$k_2 = M_K - E_{\pi^+} - k - k_1$

$R(T_{\pi^+})$ = Range of π^+ of energy T_{π^+} in scintillator plastic.

K = Constant converting distance in FC-75 to equivalent grams of scintillator.

$\sigma_\theta^2 = (15\,E_{\pi^+}/P_{\pi^+}^2)^2\,A/X_o$

X_o = Radiation length of FC-75

$T_x = 1 + A_x^2/A_y^2$

$T_z = 1 + A_z^2/A_y^2$

As was explained in the main text, the fitting procedure was to minimize - Log L with respect to the thirteen independent parameters in order to obtain the "best fit" values for the parameters. The minimumization of this nonquadratic function was accomplished by an iterative technique using a modified computer program described elsewhere (25). The value of χ^2 at the minimum for good fits should be nearly chi squared distributed with 16 - 13 = 3 degrees of freedom. It should be noted that although there are three degrees of freedom in the fitting, the kinematics are overdetermined by only 15 - 13 = 2 parameters. This arises because there are essentially two independent measurements, regardless of the conservation laws for one parameter, R_{ox}, which gets estimated directly by d_{ox} and also by extrapolation of the π^+ direction in the xy plane back to intercept the line $y = d_{oy}$. The χ^2 acceptance test is used to reject bad fits. The procedure is to pick a confidence limit, say 1% to which there corresponds a value of χ^2, χ_c^2, such that the probability for $\chi^2 > \chi_c^2$ is 1%, assuming a chi squared distributed variable. Given χ_c^2 one rejects all fits with an experimental χ^2 larger than χ_c^2 and accepts those less than χ_c^2.

B. Fits to $K_{\pi 2}$

Fitting to the $K_{\pi 2}$ hypothesis requires very little modification to the procedures described above for $K_{\pi_2\gamma}$. Four factors in L are absent, namely the three associated with measuring the point of conversion of the first photon, which was the photon of primary decay, not one of the π^o decay photons, and the factor associated

with measuring the range of the π^+ in the hodoscope. The independent parameters chosen to describe a $K_{\pi 2}$ event are:

$\vec{R}_o$ - the decay vertex,

$\vec{B} = \vec{R}_1 - \vec{R}_o$ where $\vec{R}_1$ is the point of conversion of the first photon, $C = |\vec{R}_2 - \vec{R}_o|$ where $\vec{R}_2$ is the point of conversion of the second photon,

$$\left.\begin{aligned} A_x &= R_{3x} - R_{ox} \\ A_z &= R_{3z} - R_{oz} \end{aligned}\right\}$$ where $\vec{R}_3$ is a point

on the top of the stopper where the π^+ emerges from the stopper. Table X shows the correspondence between the index, i, of expression (4) for L and the data as well as the dependence of the f_i's and σ_i^2's on the independent parameters. The procedures for the minimumization of - log L and the use of the chi squared acceptance test as described above for $K_{\pi 2\gamma}$ carry through intact for $K_{\pi 2}$ fits except that only nine parameters are involved.

TABLE X

$K_{\pi 2}$ KINEMATIC FITTING VARIABLES

i	Data	f_i	σ_i^2
1	d_{ox}	R_{ox}	$\sigma_{ox}^2 + C_1\Delta^2 + C_2\Delta^{1.82}$
2	d_{oy}	R_{oy}	$\sigma_{oy}^2 + C_1\Delta^2 + C_2\Delta^{1.82}$
3	d_{1x}	$R_{ox} + B_x$	σ_{1x}^2
4	d_{1y}	$R_{oy} + B_y$	σ_{1y}^2
5	d_{1z}	$R_{oz} + B_z$	σ_{1z}^2
6	d_{2x}	$R_{ox} + C \cdot \ell_x^*$	σ_{2x}^2
7	d_{2y}	$R_{oy} + C \cdot \ell_y^*$	σ_{2y}^2
8	d_{2z}	$R_{oz} + C \cdot \ell_z^*$	σ_{2z}^2
9	d_{3x}	$R_{ox} + A_x$	σ_{3x}^2
10	d_{3z}	$R_{oz} + A_z$	σ_{3z}^2
11	d_{4x}	$R_{ox} + A_x (1 + H/A_y)$	$\sigma_{4x}^2 + \sigma_\theta^2 H^2 T_x^2$
12	d_{4z}	$R_{oz} + A_z (1 + H/A_y)$	$\sigma_{4z}^2 + \sigma_\theta^2 H^2 T_y^2$

$*\vec{\ell} = -(\beta \vec{A}/A + \alpha \vec{B}/B)/(1 - \alpha)$

$\alpha = \frac{1}{2}(1 - \beta^2)/(1 + \beta \vec{B} \cdot \vec{A} / BA)$

β = velocity of $\pi^o = \left\{1 - \left[2 M_K M_{\pi o}/(M_K^2 - M_{\pi+}^2 + M_{\pi o}^2)\right]^2\right\}^{1/2}$

$\sigma_\theta^2 = \frac{225 (1 - \beta^2)}{\beta^4 M_{\pi+}^2} A/X_o$

A_y, C_1, C_2, C_3, Δ, X_o, T_x, T_z - Refer to Table IX

APPENDIX IX

CALCULATION OF BACKGROUNDS TO KINEMATIC FITS

Kinematic fitting is utilized in this experiment as the final test for a $K_{\pi_2\gamma}$ candidate. The fitting procedure is relied upon to separate real $K_{\pi_2\gamma}$ events from any other kind that have gotten through the pre-selection criteria. Obviously, for kinematic fitting to be useful it must reject, with high probability, non-$K_{\pi_2\gamma}$ events. The extent to which various non-$K_{\pi_2\gamma}$ events, which will survive the pre-selection criterion, can fit the $K_{\pi_2\gamma}$ kinematics is the object of this calculation. It is also of interest to compute the probabilities for various backgrounds to $K_{\pi 2}$ events to fit the $K_{\pi 2}$ kinematics.

For both cases a Monte Carlo calculation was performed. For each type of background considered a number of events were generated which were distributed as that type of background should be distributed. A generated event consisted of values for each of the measurements made on events in the experiment. The measuring errors present in this experiment were also put into the numbers generated to specify an event. The Monte Carlo events were then fit in the same manner as experimental events.

A. $K_{\pi 2}$ Backgrounds

Two types of $K_{\pi 2}$ backgrounds were considered:

(a) A $K_{\pi 2}$ decay where only one π^o photon converts in the spark chambers. The second photon converting in the spark chamber is an accidental photon.

(b) The π and K chamber tracks come from a common vertex, for example, from a K^+ decay or a π^+ interaction, but the two observed photons are accidental and uncorrelated with the π' and K' vertex.

It was assumed that the accidental photon in type (a) backgrounds was uncorrelated with the π^o decay photon and that the accidental γ was emitted isotropically from the stopper. For type (b) events it was assumed that both photons were isotropic and mutually uncorrelated. It must be remarked that if the two photons in (b) came from a π^o produced from a π^+ charge exchange scattering in the stopper then they would be isotropic but correlated.

Events of type (a) were generated by utilizing those calibration events described in Section III C 2 which gave good fits to the $K_{\pi 2}$ kinematics and replacing one of the real photons by a Monte Carlo generated accidental photon. The Monte Carlo program generated accidental photons which were isotropic in direction from the center of the stopper, which had exponential conversion point distributions with a conversion length of 10.3 plates, and which converted in the γ chambers. The conversion length of 10.3 plates is the real length not that projected to the xy plane. Type (b) events were constructed by utilizing those calibration events described in Section III C which gave good fits to the $K_{\pi 2}$ kinematics and replacing both real photons with two of the Monte Carlo generated accidental photons described above.

One hundred eighty events of each type, (a) and (b), were constructed and fitted to the $K_{\pi 2}$ kinematics with the same program and in the same manner as the calibration events. The results were than 13% of type (a) and 4.5% of type (b) fit using the same fitting criterion as used for the calibration events. A study of those giving good fits indicated, as might have been expected, that the background configuration most likely to fit was an event where one photon makes a small angle with the π^+ direction and the other goes backwards. For such a configuration small changes in the angle, which the forward photon makes with the π direction, make large changes in the π^o energy thereby making it easy to fit $K_{\pi 2}$ kinematics to the data. Two sets of plots summarize the results for the background fits; one set shown in Figure 43a and b, gives the distributions of χ^2 for the background fits to type (a) and (b) events respectively. The other set shown in Figure 44a and b, plots the opening angle distributions for those background events with χ^2 less than 12 for type (a) and (b) events respectively.

B. $K_{\pi_2\gamma}$ Backgrounds

For $K_{\pi_2\gamma}$ kinematic fitting there are a wider variety of backgrounds mainly because $K_{\pi_2\gamma}$ is so rare that rare types of backgrounds have a chance for competing with the $K_{\pi_2\gamma}$ rate. Some of the more important backgrounds are:

(1) A few π's from τ and τ' can reach channels 2 and even 3 in the π hodoscope and produce triggers. The τ events

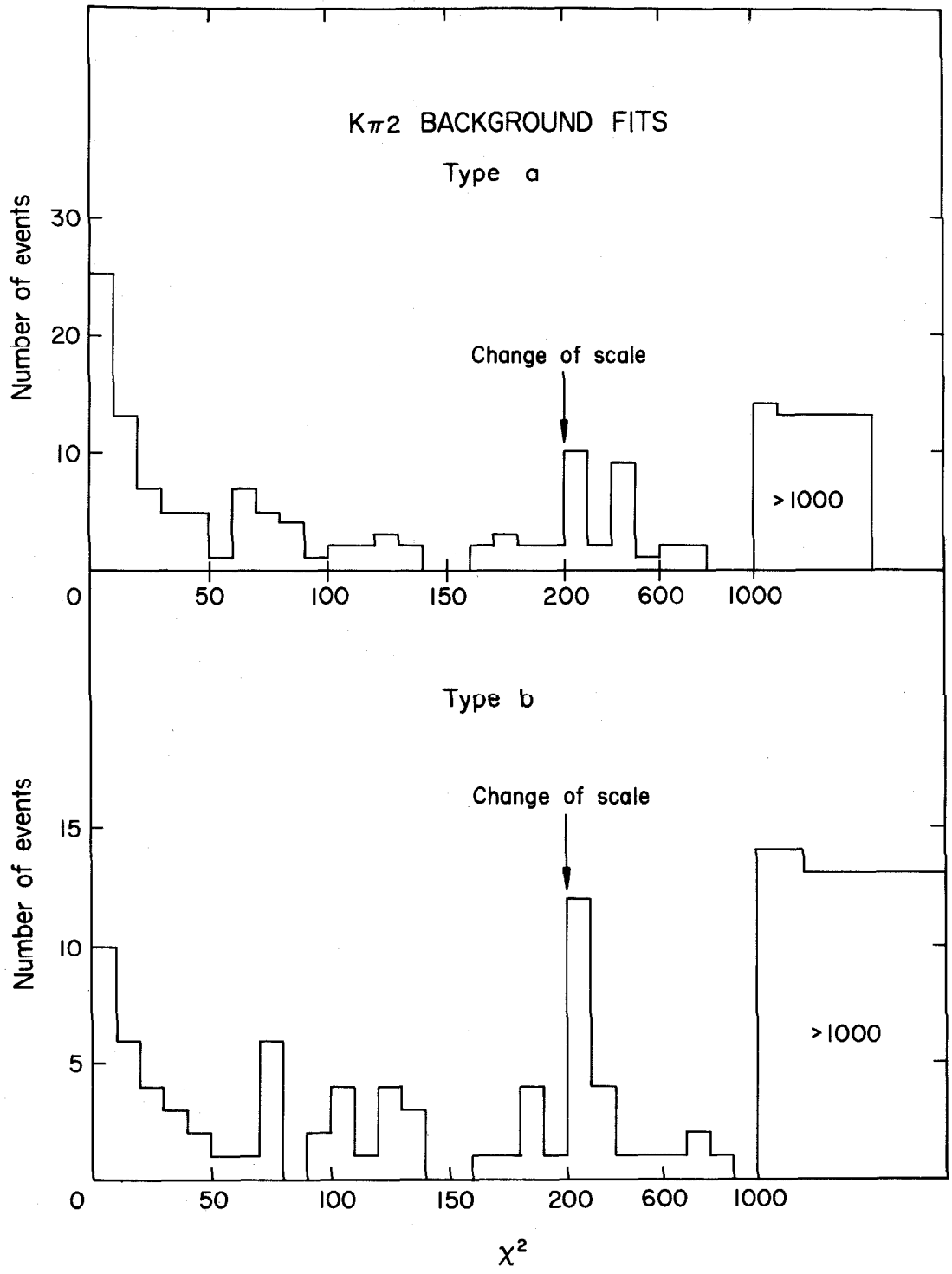
Kπ2 BACKGROUND FITS
Type a
Number of events
30
20
10
0
Change of scale
>1000
50
100
150
200
600
1000
Type b
Number of events
15
10
5
0
Change of scale
>1000
50
100
150
200
600
1000
χ²

Figure 43

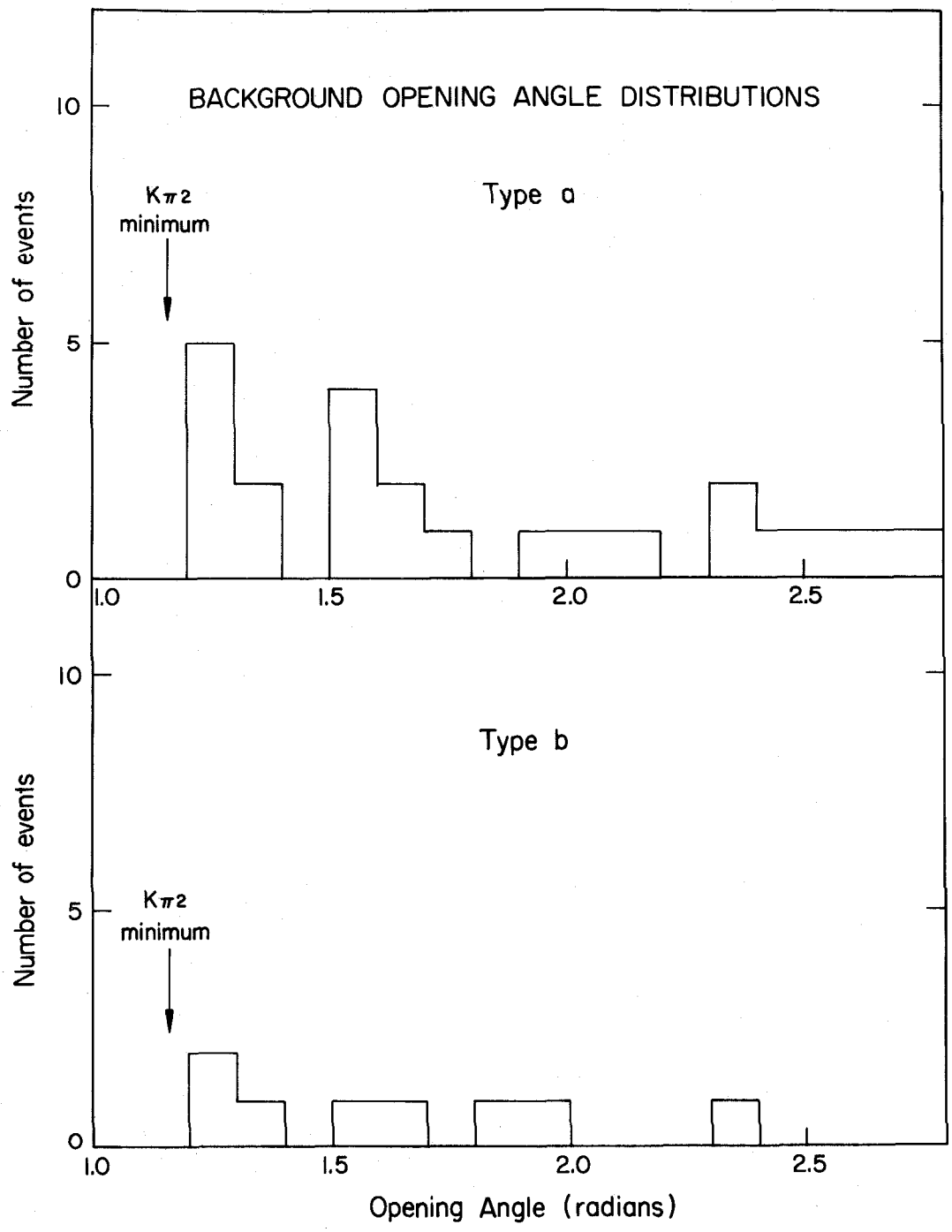
BACKGROUND OPENING ANGLE DISTRIBUTIONS
Type a
Kπ2 minimum
Number of events
10
5
0
1.0
1.5
2.0
2.5
Type b
Kπ2 minimum
Number of events
10
5
0
1.0
1.5
2.0
2.5
Opening Angle (radians)

Figure 44

can yield up to four photons; the τ events none. Accidental photons can, of course, be present for both types of events.

(2) The π^+ from $K_{\pi 2}$ can scatter inelastically in the stopper and thus appear as a short range π in the π hodoscope. When enough accidental photons are present to provide a total of three photons one has a possible $K_{\pi_2\gamma}$ background.

(3) When the π^+ from $K_{\pi 2}$ interacts after the π chamber it can appear to have a short range. Enough additional accidental photons to produce a total of three yields a possible $K_{\pi_2\gamma}$ background. These events will fit $K_{\pi 2}$ kinematics if two of the photons are from the π^o decay. This is not true of the type described in (2).

(4) The π^+ from a $K_{\pi 2}$ may scatter in the background direction off the material in the γ chamber 3 and go back through the stopper, through the π chamber and appear as a short range π^+ in the π hodoscope. Additional accidental photons to give a total of three observed γ's provide another $K_{\pi_2\gamma}$ background.

In an effort to estimate the chance for the above types of backgrounds to fit several types of Monte Carlo generated events were fit to the $K_{\pi_2\gamma}$ hypothesis using the same criteria as used with the real data. One category of events utilized the 36

calibration events that were found to fit the $K_{\pi 2}$ hypothesis. To these events were added accidental photons with the same characteristics as those used in the $K_{\pi 2}$ background calculation which is described in Section A of this appendix. Only the π^+ direction was used; its range in the hodoscope was required to be distributed according to the experimental distribution seen for the 174 $K_{\pi_2\gamma}$ candidates. Three sets of events were generated by using the $K_{\pi 2}$ data described above and constructing the following three sets of photons:

(a) Both π^o photons and one accidental.

(b) Only one π^o photon and two accidentals.

(c) Three accidental photons only.

Two more types of events were constructed using the $K_{\pi 2}$ interaction events constructed by the Monte Carlo program described in Appendix VI and adding enough accidental photons to total three. The types are:

(d) The $K_{\pi 2}$ interaction events with both π^o photons and one accidental photon.

(e) The $K_{\pi 2}$ interaction events with only one π^o photon and two photons.

The five types of events (a) through (e) were fit to the $K_{\pi_2\gamma}$ kinematics in the same manner as for "real data". Each event was fit three times, each time using a different photon as the photon from the primary $K_{\pi_2\gamma}$ decay. The combination with the smallest χ^2 determines the quality of the fit. The distributions of the

smallest χ^2 of each triplet for all five types are plotted in Figure 45. The table below summarizes the results.

Type	Number of events used	Number that fit	Percent fitting
(a)	60	28	47 ± 9
(b)	60	11	18 ± 6
(c)	60	9	15 ± 5
(d)	51	0	0 + 1.3
(e)	51	7	12 ± 5

Type (a), (b), and (c) events describe the background listed in (3), while type (d) and (e) describe the backgrounds listed in (2). Tye type (c) events stopping in channels 2 and 3 provide an estimate for the backgrounds listed in (1) to the extent that the τ' events can be approximated as having three isotropic uncorrelated photons. The τ' events that produce $K_{\pi 2\gamma}$ triggers in channels 2 and 3 are those for which the π^+ has close to the maximum allowed energy. For these events the two π^o tend to come off together with low energy (~ 20 MeV); thus the γ's from the π^o will have wide opening angle and be nearly isotropic. The backgrounds listed in (4) can be estimated by the (c) and (d) type events. The events in (4) will have π^o's moving in the direction of the hodoscope as also do the $K_{\pi 2}$ interactions in the stopper because the π^+ interaction cross

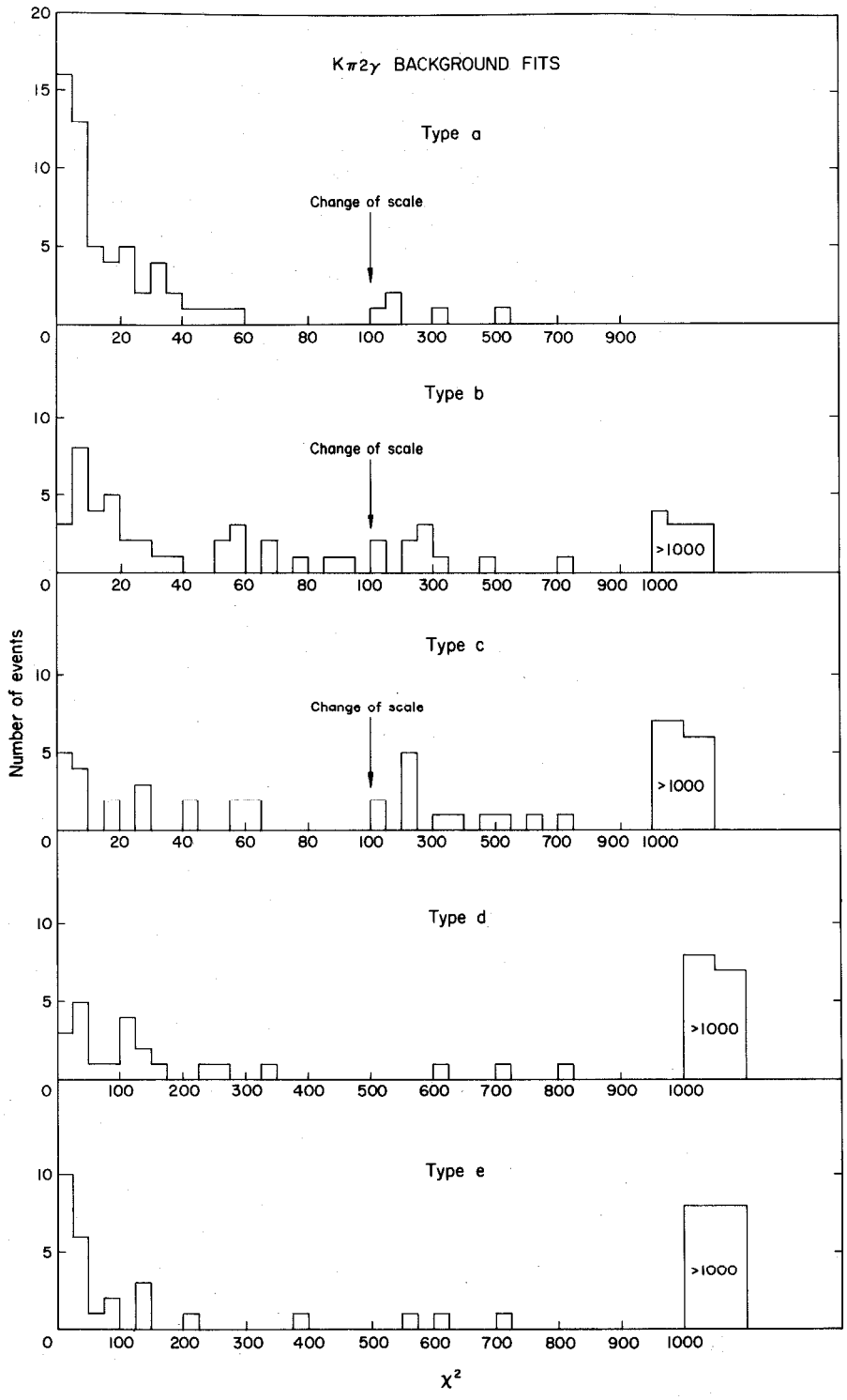
Kπ2γ BACKGROUND FITS
Type a
Change of scale
Type b
Change of scale
>1000
Type c
Change of scale
>1000
Type d
>1000
Type e
>1000
Number of events
χ²

Figure 45

section is peaked for background angles. Thus the background of category (4) will have mostly events with two accidental photons and will have more trouble fitting $K_{\pi_2\gamma}$ kinematics than type (d) events because of the larger discrepancy between π^+ direction and K^+ location.

APPENDIX X

SPARK CHAMBER MEASURING PROCEDURES AND MEASUREMENT ERRORS

A. Spark Chamber Measuring Procedures

The procedures for measurement and event reconstruction will be discussed as a prelude to a discussion of measurement errors. All spark chamber measurements used in the final analysis were made with a digitized measuring table on which the projected image of the film fell. The measuring table was of the variety that used crossed mylar belts geared to 10,000 count encoders through a chain drive from the cylindrical drums over which the mylar belts passed. Each belt had a fine line drawn on it perpendicular to its motion; the encorders were connected to a Datex storage and translating unit. Each time the data record footswitch closed both encoders were read out and four decimal digits per axis were punched onto cards by the IBM 526 Summary punch attached to the system. Parameters from a 20-digit parameter board were also available for punching onto the data cards as desired.

For each frame measured, the first measurements were of fixed fiducial marks in order to determine the transformation to laboratory space. The fiducial plate used in this experiment provided a grid with a 5 cm separation in laboratory space. Three grid crossings were measured in the vicinity of each measured track in order to overdetermine a local transformation which

corrected for the various nonlinearities in the optical system. Some of the nonlinearities such as the barrel distortion of the field lens and the distortion of the projector system are constant from frame to frame but the nonlinearities due to the curvature and buckling of the film in the camera vary from frame to frame. The first, fixed type of distortion could be measured once and corrected for but the latter variable type required frame by frame correction.

For the π track, all sparks and reflections in the π chamber were measured. The depth coordinate of each spark was computed from the distance between spark and reflections. Then a straight line was fitted to the points represented in the measurements of the sparks by making a least squares fit to the projection in the xy plane and to the projection in the yz plane. From the fit, the coordinates and errors of this fitted line's intersection with the top of the stopper ($\vec{d}_4$) and the center line of the π chamber ($\vec{d}_5$) were computed. The value of χ^2 was computed and used as a goodness of fit criterion.

The reflections of the spark in the K chamber gap next to the S_K counter were measured and the point of entry, $\vec{P}_K$, of the K^+ into the stopper was computed from these measurements. Next, by assuming a $\theta = 0^\circ$ K^+ trajectory the position of closest approach of the π and K trajectories was computed. The distance of closest approach and its projections onto the coordinate axes were computed for monitoring purposes.

For each γ track, several sparks and reflections at the beginning of the track starting with the gap nearest the point of conversion were measured and then fitted to the best value of the point of conversion and the γ direction by a maximum likelihood fitting procedure which included measuring error and multiple scattering of the electrons in the shower. The procedure also yields estimates of the error on the fitting parameters and a χ^2 for the fit.

For the $K_{\pi_2\gamma}$ events, the range of the π^+ in the hodoscope was computed from the π^+ trajectory parameters and the pulse height in the stopping counter. Numerous checks for gross error and bad measurements were made, such as χ^2 for all track and shower fits, the miss between the π and K trajectories, local transformation parameters, and consistency of the depth calibration for sparks having two reflections where an independent computation of the depth was available.

B. Measuring Errors

There are several categories of measurement errors in this experiment and they are listed below.

(1) The error in estimating the center of a spark or reflection.

(2) The faithfulness of the center of the spark to a point on the particle trajectory.

(3) The faithfulness of the reflections to the main spark.

(4) The uncertainty in the geometrical parameters of the spark chamber assembly.

How these errors affect the respective items of data will be discussed shortly.

The error mentioned in (1) can be determined from the reproducibility of the measurement of a spark or reflection. When this was done the result was 0.14 mm in the laboratory space and is roughly 10% of the width of a spark.

Straight line fits in the xy plane to data from fast, heavy particles tracks can be used to estimate the error from item (2). One assumes a reasonable value for σ_{total} and uses this assumed value to fit many tracks. Because χ^2 scales by σ^2_{total} and because the expected value of χ^2 is known the average value of the observed χ^2 can be used to solve for the actual value of σ^2_{total} from the relation

$$\langle \chi^2 \text{ observed} \rangle \frac{\sigma^2_{used}}{\sigma^2_{total}} = N$$

where N is the number of degrees of freedom for the fits. The width of the observed χ^2 distribution can be compared with the expected width as a check on the procedure. The σ_{total} so determined is compounded from sources (1) and (2) above; with the error from (1) known the error from (2) can then be obtained. For π's from $K_{\pi 2}$ and for cosmic rays in the thin plate π chamber, the σ for source (2) is about 0.33 mm and for a cosmic rays in the γ chamber it is about 0.44 mm.

The depth coordinate is essentially given by a factor of approximately 5 times the distance between reflections when both reflections are present or by about 10 times the distance between spark and reflection when only one reflection is present. The distance to be used is the distance between corresponding points on the spark and the reflection, projected onto the spark chamber plates. For a variety of reasons the center of a reflection does not correspond to the center of a spark. Small irregularities in the mirrors distort the reflection; the two mirrors in a given gap look at different parts of the spark; small twists in the mirrors cause even two mirrors in the same relative position in different gaps to look at different portions of the spark; an irregular shape to a spark upsets the correspondence of center of spark and reflection. Because of the nature of the above irregularities, the errors introduced by them vary from track to track and gap to gap so that over the chamber they can be treated as random errors for the purpose of fitting tracks. From χ^2 fits to fast heavy particle tracks in the yz plane one obtains a σ_{total} which is compounded of errors from source (2) and 5 or 10 times the magnitude of errors from sources (1) and (3). The σ_{total} so obtained is 1.8 mm for the case with both reflections and 3.2 mm with one reflection. It is apparent that source (3) dominates these σ's. Unfolding the $\sigma_{(3)}$ gives 1.65 mm for the case with both reflections and 2.9 mm with one reflection. As might be expected these last σ's depend upon the angle the track makes with the plates. The numbers presented are an average over angles.

The uncertainties of type (4) are the most difficult to estimate and are also fairly serious. The most important errors of this category are errors in the depth calibration. They are discussed in Appendix III C and produce about a 1% uncertainty for the case of both reflections and about 1.5% for the case of one reflection. These correspond to uncertainties of 3.0 and 4.5 mm respectively in depth for a nominal depth of 30 cm. The errors associated with the local transformation are small and contribute 0.2 to 0.3 mm in x and y and 0.5 mm in z. Uncertainties in the location of the planes of the mirror plate are about 2 mm in depth.

For the π^+ tracks systematic errors in the π chamber depth calibration appreciably affect the π angle and location of the point where π extrapolates back to the stopper. The uncertainty of about 1° in the tilt of the π chamber (depth view) and an uncertainty of 0.01° in the mirror angle contribute an error of about 5 mm to the z coordinate of the decay vertex.

Systematic errors also effect the measurements of the x and y coordinates of the decay vertex. Uncertainties in the parameters describing the orientation of the K chamber mirrors contribute systematic errors of about 3 to 5 mm. Other errors which are not systematic include multiple scattering of the K^+ in the stopper and the angular spread of the beam. The contributions due to these depend upon the distance, D, of the K meson's penetration into the stopper; which, for the average value of D, were 2 mm from the multiple scattering and 5 mm from the angular spread. The

formulas in the list below for the total error on R_{ox} or R_{oy} show the explicit dependence on D; the D^2 term arises from the angular spread of the beam and the $D^{1.82}$ term from multiple scattering while the constant term summarizes the systematic errors.

The list below shows the total errors on all quantities that were used in the kinematic fits. They were compounded from the various errors discussed above. In some cases, notably on the depth measurements, certain errors have contributions that depend upon the depth, however, the total variation with depth is not great enough to warrant the additional computational effort, so, for these cases the average value of the error was used. The uncertainty in the π^+ range after the top of the stopper comes mainly from range straggling and the uncertainty in the range measurement in the stopping counter. Range straggling is about 3% and the uncertainty of the range in the stopping counter averaged over a uniform stopping distribution is 0.4 gr. Other errors are a 0.3 gr uncertainty in the location of the top of the stopper, and a 0.3 gr. error in the range in lucite wedge due to uncertainty in the location of the wedge. The π^+ direction uncertainties make a negligible contribution to the range error.

Measurement Errors Used in Kinematic Fits

R_o

$$\sigma_x^2 = 9 + 1.2 \times 10^{-2} D^2 + 7 \times 10^{-3} \times D^{1.82} \quad (\text{mm.}^2)$$

$$\sigma_y^2 = 25 + 1.2 \times 10^{-2} D^2 + 7 \times 10^{-3} \times D^{1.82} \quad (\text{mm.}^2)$$

R_y

$\sigma_x = 0.6$ mm

$\sigma_y = 0.6$ mm

$\sigma_{zI} = 5$ mm

$\sigma_{zII} = 6$ mm

R_4

$\sigma_x = 2$mm

$\sigma_{zI} = 18$mm

$\sigma_{zII} = 11$mm

R_5

$\sigma_x = 0.4$ mm

$\sigma_{zI} = 5$ mm

$\sigma_{zII} = 4$ mm

Range in hodoscope

$\sigma_H = 0.8$ gr.

I and II above refer to the case of one or two reflections respectively.

APPENDIX XI

EFFICIENCIES

A. Channel 1 Predictions

In Section III D 3 reference was made to predictions for the number of channel 1 triggers expected as well as the distributions of γ rays that should be seen. The details of the calculation will be described here. The number of τ or τ' triggers expected is given by the following formula

$$N = N_K \cdot \epsilon_{DT} \cdot R \cdot \epsilon_{\pi-\mu} \cdot \Omega_1 \cdot M \int_{\text{counter 1}} P(x)\, dx$$

where N_K is total number of stopping K's detected, ϵ_{DT} is the dead time correction factor, R the branching ratio for the decay mode in question, $\epsilon_{\pi-\mu}$ the detection efficiency for the detecting π-μ decays in channel 1, Ω_1 the solid angle subtended by channel 1, M = 1 or 2 is the π^+ multiplicity for τ or τ' modes respectively and P(x) is the projected range distribution in channel 1 for the π^+ from the mode in question. P(x) is obtained by suitably convoluting the range spectrum f(R) for mode in question with distribution $P_1(y)$ of the height of the K^+ in the stopper as expressed below.

$$P(x) = \int P_1(y)\, f(x + c - y)\, dy$$

where c is the total height of the stopper in the y direction. The range spectra are obtained by transforming the published π^+ energy spectra (26, 27), N(E), for τ and τ', using a well known formula

involving dE/dx and the range energy $E(x)$ relations for the material involved as follows:

$$f(x) = N(E(x)) \frac{dE}{dx} (x)$$

In this way both N_τ and $N_{\tau'}$, the number of τ and τ' events to be expected, are computed. The dead time factor is computed from the average number of pictures per pulse, the π-μ detection efficiency of 0.5 from the cutoffs on the μ delay curve and the channel 1 solid angle from geometry. For $N_K = 4.3 \times 10^6$, the results are

$$N_\tau = 277 \text{ or } 84\%$$

$$N_{\tau'} = 53 \text{ or } 16\%$$

Photon distributions are arrived at by assuming that the γ's from τ' are isotropically distributed with a 50% probability for converting in the γ chambers. The 50% probability is the effective solid angle of the γ chambers. The assumption of γ isotropy is reasonable because the π^o's are of low energy for those τ' that can trigger channel 1. Final γ distributions include modifications for γ accidentals. A table in Section III D 3 shows the distribution of number of γ's per frame both with and without accidentals. The angular distribution of γ's would be uniform both with and without accidentals.

B. Scanning Efficiency

The most critical scanning efficiency is associated with detecting π-μ decays. For a variety of reasons discussed in the main text, the μ pulses are difficult to observe on the fast display photographs. By comparing the results of several scans of the same runs by different scanners a measure of this efficiency is obtained. From the comparison of two scanners one obtains the number of decays missed by the one scanner and seen by the other; for example, say scanner No. 1 saw N_1 events not seen by No. 2 and No. 2 saw N_2 not seen by No. 1. If both saw a total N decays then the expected value of the efficiencies, ϵ_1 and ϵ_2 for scanners No. 1 and No. 2 respectively, are

$$\epsilon_1 = \frac{N}{N + N_2}$$

$$\epsilon_2 = \frac{N}{N + N_1}$$

In this manner the three regular scanners and a physicist (the author) were compared with the result that scanning efficiencies for good π-μ decays varied from 85 ± 2.2% to 94 ± 1.8% with an average of 90 ± 1.2% while the scanning efficiency for π-μ candidates varied from 86 ± 1.8% to 91 ± 1.6% with an average of 88 ± 0.9%

C. Composition of $K_{\pi 2}$ Calibration Runs

The 232 Type S events of the calibration runs described in Section III E 2 from which $K_{\pi 2}$ events were isolated by kinematic fits are not pure $K_{\pi 2}$. Muons from $K_{\mu 2}$ and $K_{\mu 3}$ which go through

channels 1, 5 and 6 but miss channels 7 and 8 would be placed in the Type S category. The number of $K_{\pi 2}$ detected in the calibration runs is given by

(1) $$N_K \cdot R_{\pi 2} \cdot S_{1\cdot 5\cdot 6}$$

where N_K is the number of K decays observed, $R_{\pi 2}$ is the $K_{\pi 2}$ branching ratio, and $S_{1\cdot 5\cdot 6}$ is the solid angle for channels 1, 5 and 6 in coincidence. The number of $K_{\mu 2}$ which go through channels 1, 5 and 6 but miss 7 and 8 is given by

(2) $$N_K \cdot R_{\mu 2} \cdot (S_{1\cdot 5\cdot 6} - S_7)$$

where $R_{\mu 2}$ is the $K_{\mu 2}$ branching ratio and S_7 is the solid angle for channel 7.

The fraction of $K_{\pi 2}$ in Type S is then given by the ratio of (1) to the sum of (1) and (2) which reduces to

$$\frac{R_{\pi 2}}{R_{\pi 2} + R_{\mu 2} \cdot \left(1 - \frac{S_7}{S_{1\cdot 5\cdot 6}}\right)} = 0.58$$

Combining this fraction with the result of Appendix VI for the fraction of $K_{\pi 2}$ triggers where both π^o photons convert means that 16% or 38 events of the Type S events will be $K_{\pi 2}$ with both photons visible in the γ chambers.

APPENDIX XII

CHARGED PARTICLE ACCIDENTAL DATA

As was discussed in Section III D 3, charged particle rates and distributions are of interest because they can serve as a monitor of γ accidentals. For each of the three sets of γ data to be considered, the channel 1 events, the channel 6 events, and 174 $K_{\pi_2\gamma}$ candidates, the charged particles distributions observed will be compared with the results obtained from the $K_{\mu 2}$ background runs. The background run data have been normalized to the observed number of frames for each of the three sets of γ data. Two distributions, the distribution of number of charged particles tracks per frame and the azimuthal angular distribution, will be considered below.

A. Channel 1 Events

Distribution of number of charged particles Tracks per frame (Channel 1)

Charged/ Frame	Number of Frames		Poisson Using
	Observed	Background Run	Observed Average
0	185	190	192
1	101	80	96
2	20	39	24
3	5	4	4
4	0	3	0
Total	316	316	316

Charged Particle Azimuthal Angular Distribution
(Channel 1)

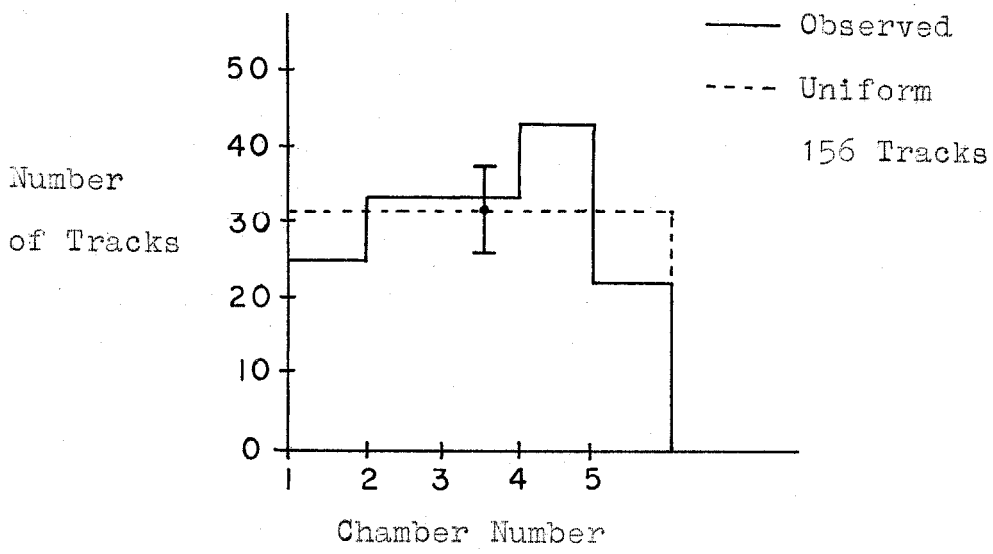

On the basis of the background runs 182 ± 10 tracks are expected for the 316 Channel 1 frames while 156 ± 13 are observed.

B. Channel 6 Events

Distribution of the number of charged particles Tracks per frame (Channel 6)

Charged/ Frame	Number of Frames Observed	Number of Frames Background Run	Poisson Using Observed Average
0	42	45	44
1	31	24	28
2	8	11	9
3	2	2	2
4	0	1	0
Total	83	83	83

Charged Particle Azimuthal Angular Distribution (Channel 6)

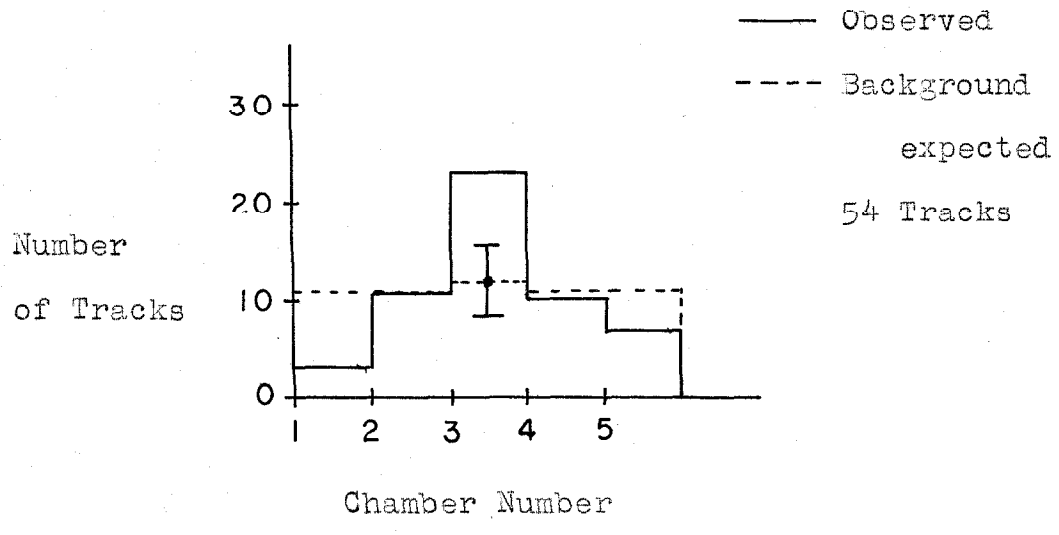

On the basis of the background run 56 ± 7 charged particle tracks are expected for the 83 channel 6 frames while 54 tracks are observed.

C. The 174 $K_{\pi_2\gamma}$ Candidates

Distribution of number of charged Particle Tracks per Frame

Charged/ Frame	Number of Frames Observed	Number of Frames Background Run	Poisson Using Observed Average
0	106	108	107
1	54	42	52
2	12	21	13
3	2	3	2
Total	174	174	174

Charged Particle Azimuthal Angular Distribution

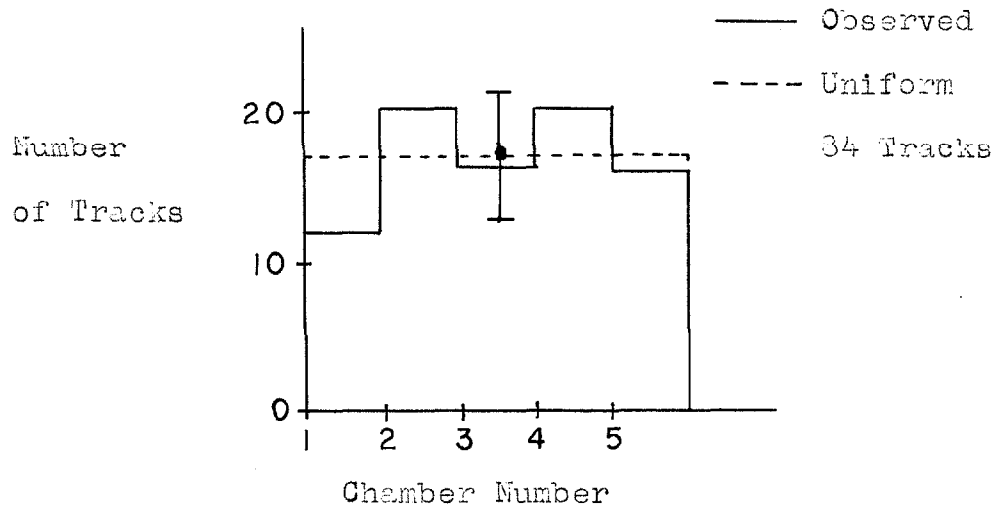

On the basis of the background runs, 93 ± 10 tracks are predicted and 84 ± 9 are observed.

D. Summary

The three groups of data presented above show that the charged particle rates and distributions are in general agreement with the

background runs. This insures that the γ accidental rates and distributions for each of the three goups are unchanged from the background run. Whenever corrections for γ accidentals were made they were made using the rates and distributions derived from the $K_{\mu 2}$ background runs.

In each of the three cases considered above the number of charged particle tracks expected on the basis of the background runs have been corrected for γ's that convert in the stopper and lucite wall of the spark chambers. In all three cases the number of charged particle tracks observed are slightly fewer than expected on the basis of the background run although roughly within the statistics. The angular distributions are nearly uniform except possibly for channel 6 where a peaking in chamber 3 is observed, although the small number of events limits the statistics. The distributions of tracks per frame are in general agreement with the background runs and even better agreement with the Poisson distributions using the observed averages. The background runs show a slightly higher fraction of multiple track frames at the expense of single track frames.

Footnotes and References

1. R. H. Dalitz, Int. Conf. on Fundamental Aspects of Weak Interactions, 1963, BNL-837, Abstract NSA 18:4429
2. M. Roos, Rev. Mod. Phys. 35, 315 (1963)
3. Cork, Kerth, Wenzel, Cronin, Cool Phys. Rev. 120, 1000 (1960)
4. N. Cabibbo, Phys. Rev. Letters 12, 62 (1964)
5. Kiyomi Itabashi, Phys. Rev. 136, 221 (1964)
6. J. D. Good, Phys. Rev. 113, 352 (1959)
7. N. Cabibbo and R. Gatto, Phys. Rev. Lets. 5, 382 (1960)
8. S. Pepper and Y. Ueda, U. of Rochester Report UR-875-30
9. S. Oneda and Y. Kim, Phys. Letters 8, 83 (1964)
10. H. Chew, Nuovo Cimento 26, 1109 (1962)
11. I. G. Ivanter, JETP 14, 557 (1962)
12. H. Chew, Phys. Rev. 123, 377 (1961)
13. K. Hiida, Nuovo Cimento, 8, (1117) (1959)
14. B. P. Roe, et. al., Phys. Rev. Letts. 1, 346 (1961)
15. R. W. Birge, et. al., Phys. Rev. Letts. 11, 35 (1963)
16. G. Harris, et. al., Phys. Rev. 108, 1561 (1957)
17. D. S. Prowse and B. Evans, Nuovo Cimento, 8, (1958)
18. D. Monti, et. al., Nuovo Cimento, 21, 550 (1961)
19. See table, Page 553 of Reference 18.
20. D. Cline and W. F. Fry, Phys. Rev. Letts. 13, 101 (1964)
21. W. C. Davidon, Argonne National Laboratory Report, ANL-5990 Rev. (1959)
22. A. V. Tollestrup, CTSL Internal Report No. 6, (1963)

23. Compilation prepared by D. Groom, Synchrotron Laboratory, California Institute of Technology, Pasadena, California

24. F. P. G. Valckx, Nuovo Cimento 23, 1005 (1962)

25. J. O. Kessler and L. Lederman, Phys. Rev. 94, 689 (1954)

26. S. McKenna, et. al., Nuovo Cimento, 10, 763 (1958)

27. G. Giacomelli, et. al., Physics Letters 3, 346 (1963)

28. D. E. Greiner, et. al., Phys. Rev. Letts. 13, 284 (1964)

29. Photon absorption in Fe extrapolated from the Cu data at 55 MeV of

Rosenblum et. al., Phys. Rev. 88, 612 (1952)
Adams, Phys. Rev. 74, 1707 (1948)
Lawson, Phys. Rev. 75, 433 (1949)
DeWire et. al., Phys. Rev. 82, 447 (1951)

by assuming the cross-sections to be proportional to $Z^2 \log (183\ Z^{-1/3}) - 1/42$ at a given energy.